

Copyright
by
Timothy Bryan Michaelson
2005

**The Dissertation Committee for Timothy Bryan Michaelson Certifies that this is the
approved version of the following dissertation:**

**Free Radical Graft Polymerization Lithography and Modeling Base
Quenchers in Photoresists**

Committee:

C. Grant Willson, Supervisor

Roger T. Bonnecaze

John G. Ekerdt

Benny D. Freeman

Chris A. Mack

**Free Radical Graft Polymerization Lithography and Modeling Base
Quenchers in Photoresists**

by

Timothy Bryan Michaelson, B.S.; M.S.

Dissertation

Presented to the Faculty of the Graduate School of

The University of Texas at Austin

in Partial Fulfillment

of the Requirements

for the Degree of

Doctor of Philosophy

The University of Texas at Austin

August, 2005

Dedication

To my family.

Acknowledgements

Without the help and support of many individuals, this work would not have been possible. I would like to start by thanking Dr. Willson for patiently providing me with help and support throughout my undergraduate and graduate career at The University of Texas at Austin. I would also like to thank the members of my dissertation committee for their helpful advice and discussion. Several undergraduate students were involved in this project as well, and foremost among them, I would like to sincerely thank Jose Rangel for help with many aspects of this work over several years. I would also like to thank undergraduate students Brooke Anderson, Khiet Nguyen, Simon Sierra, and Ian Blair as well as high school student Emily Seen for contributions to this work as well.

I have been privileged to work in a research group full of wonderful, talented people that have gone above and beyond any of my expectations in helping me with various aspects of this work. For this privilege, I would like to thank all the members of the Willson group, both past and present. Specifically, I would like to acknowledge the contributions of Andrew Jamieson, Jason Meiring, and Michael Stewart for helpful discussions and collaboration on several projects. I would also like to thank Matthew Colburn for working with me when I was an undergraduate in this research group and for helpful discussions early in my graduate career. I would like to thank Kyle Patterson, Thomas Mrozek, Matthew Pinnow, Brian Osborn, Charles Chambers, and Yukio

Nishimura for help with chemical synthesis. I would also like to acknowledge Pavlos Tsiartas, Sean Burns, and Colin Brodsky for help with various aspects of this work as well.

I have been extremely fortunate to have had the opportunity to work closely with industry on various aspects of this work. I would like to gratefully acknowledge the contribution of AMD to this work. AMD has provided access to tools and facilities as well as the time of its employees throughout the course of this work. I would like to thank Adam Pawloski, Alden Acheta, and Harry Levinson with AMD for their contributions. I would also like to thank International SEMATECH for access to their tools and facilities as well. I would like to thank Daniel Miller, Jordan Owens, Larry Looger, Arnie Ford, Will Conley, Tawfeeq Alzaben, Rene Diaz, and Karen Turnquest for their contributions. Finally thanks to Jeff Byers and Mark Smith with KLA Tencor for help with this work as well.

Without funding, none of this work could have happened. I would like to thank SRC, DARPA, The National Science Foundation, and International SEMATECH for funding various aspects of this project. I would also like to thank KLA Tencor, AZ Clariant, Dupont Electronic Polymers, EUV Technology, Texas Instruments, and Ciba Specialty Chemicals for donation of chemicals, equipment, and software.

Free Radical Graft Polymerization Lithography and Modeling Base Quenchers in Photoresists

Publication No. _____

Timothy Bryan Michaelson, Ph. D
The University of Texas at Austin, 2005

Supervisor: C. Grant Willson

The process of cationic graft polymerization lithography was developed at The University of Texas at Austin. This process is a top surface imaging scheme that involves using photogenerated acid to initiate the graft polymerization of a gas phase monomer onto a surface. This technique relies on the cationic initiation of polymerization and, hence, is limited to a certain set of monomers and initiators. There are very few photoacid generators strong enough to initiate cationic polymerization. Also, the amount of photoacid generator that can be added to a polymer film is limited by its solubility in the film. Furthermore, only vinyl ethers and epoxides have been found to be active towards this type of polymerization.

Because of these limitations, an alternate, free radical based scheme for graft polymerization lithography was desired. Free radical graft polymerization lithography would allow a multitude of initiators to be used, including polymer bound initiators. It would also allow access to a new set of monomers. This document describes the

development of a free radical graft polymerization lithography scheme. Custom synthesis of both the initiator and monomer, design and automation of the grafting chamber, studies of grafting kinetics, and imaging experiments are described.

This dissertation also describes fundamental research into the function of base in photoresists. As critical dimensions in microlithography become ever smaller and the importance of line-edge roughness becomes more pronounced, it is becoming increasingly important to gain a fundamental understanding of how the chemical composition of modern photoresists influences resist performance. Modern resists contain four basic components: polymer, photoacid generator, dissolution inhibitor, and base quencher. Of these four components, the one that is least understood is the base quencher. This dissertation examines the influence of base additives on line-edge roughness, contrast, photospeed, and isofocal critical dimension (CD). Furthermore, the function of acid/base neutralization products in photoresist films is examined.

Table of Contents

List of Tables	xiii
List of Figures	xiv
Chapter 1: Traditional Photolithography	1
1.1 Introduction and Moore's Law	1
1.2 Device Fabrication and Lithography	2
1.3 Exposure	4
1.4 The Photoresist.....	7
1.4.1 Non Chemically Amplified Resists	7
1.4.2 Chemically Amplified Resists	9
Chapter 2: Top Surface Imaging.....	14
2.1 Introduction.....	14
2.2 Top Surface Imaging.....	15
2.3 Multilayer Resists	16
2.4 CARL Process.....	19
2.5 Digital Silylation.....	20
2.6 Graft Polymerization Lithography	21
Chapter 3: A Free Radical Scheme for Top Surface Imaging	24
3.1 Introduction to Free Radical Grafting.....	24
3.2 A Living Free Radical Process	25
3.2.1 Introduction to Living Free Radical Polymerization	25
3.2.2 Development of a Living Free Radical Initiator for TSI	28
3.3 A Non-Living Free Radical Process	34
3.3.1 Initiator Synthesis	34
3.3.2 Initiator Testing and Early Grafting Results	41
3.3.3 Developing an Imaging Process	44
3.4 Synthesis of Gas Phase Silicon Containing Monomers	46
3.5 Conclusions.....	48

3.6 Experimental	48
3.6.1 Living Free Radical Generator Synthesis	48
3.6.2 Non-Living Free Radical Generator Synthesis	52
3.6.3 Synthesis of Silicon Containing Monomers	56
Chapter 4: Grafting Results and Conclusions	58
4.1 Introduction.....	58
4.2 Early Investigation of the Grafting Process	59
4.3 Kinetic Studies	66
4.4 Imaging Experiments	74
4.5 Design and Imaging Results from The Larger Wafer Chamber	79
4.6 Conclusions and Recommendations	82
Chapter 5: Neutralization Byproducts in Photoresists	84
5.1 Introduction.....	84
5.2 Salt Studies.....	85
5.3 Conclusions and Recommendations	94
5.4 Experimental	96
5.4.1 General Procedure for the Synthesis of Triflate Salts.....	96
5.4.2 Purity Analysis.....	96
5.4.3 Infrared Spectroscopy (IR)	97
5.4.4 Specific Salt Synthesis Information.....	98
Chapter 6: The Influence of Base on Bias	101
6.1 Introduction.....	101
6.2 Experimental	103
6.2.1 Materials	103
6.2.2 Formulation Strategy	103
6.2.3 Contrast Studies	104
6.2.4 Imaging Experiments	105
6.2.5 Data Analysis	106
6.2.6 Error Analysis	107
6.3 Results.....	107

6.3.1 Simulation Results	108
6.3.2 Experimental Results	109
6.3.3 193nm Photoresist Results	112
6.4 Discussion	113
6.4.1 Simulation Results	113
6.4.2 Experimental Results	114
6.5 Conclusions and Recommendations	118
Chapter 7: The Influence of Base on Line-Edge Roughness	121
7.1 Introduction.....	121
7.1.1 Contrast	121
7.1.2 Line-edge roughness	122
7.2 Results.....	123
7.2.1 Contrast Studies	124
7.2.2 Line-Edge Roughness Studies	125
7.3 Discussion	126
7.3.1 Contrast Studies	126
7.3.2 Line-Edge Roughness	129
7.4 A Second Round of Experiments.....	130
7.5 Experimental	131
7.5.1 Materials	131
7.5.2 Measuring Deprotection Kinetics	131
7.5.3 Imaging Experiments.....	132
7.5.4 Data Collection and Analysis.....	133
7.6 Results.....	133
7.6.1 Deprotection Kinetics	133
7.6.2 Line-Edge Roughness	134
7.7 Discussion	137
7.7.1 Aerial Image Analysis.....	137
7.7.2 Modeling.....	139
7.8 Conclusions and Recommendations	143

Chapter 8: Conclusions and Recommendations	146
8.1 Graft Polymerization Lithography	146
8.2 Modeling Base Quenchers	148
References	153
Vita	161

List of Tables

Table 5.1	Acid and base components of various salts tested for activity in TBOC films	93
Table 6.1	Experimental Results for isofocal CD studies (nominal mask CD = 160 nm).....	110
Table 6.2	Experimental results for the second round of isofocal CD studies (nominal mask CD = 180nm)	111
Table 7.1	LER as a function of base type and loading	125
Table 7.2	LER as a function of PEB temperature for a resist without base and for a resist containing 10% TOA	126

List of Figures

Figure 1.1	Moore's law ⁴	2
Figure 1.2	Multiple levels of patterned copper wires on a semiconductor device ⁵	3
Figure 1.3	The lithography process	4
Figure 1.4	Diffraction induced blurring of an aerial image from an ideal square wave to what is actually seen	5
Figure 1.5	Solubility switch in the DNQ/novolac photoresist system	8
Figure 1.6	Solubility change upon exposure of a DNQ/novolac resist as a function of DNQ loading ⁸	9
Figure 1.7	The chemistry of TBOC based chemically amplified resists ¹	11
Figure 1.8	193nm photoresists	12
Figure 2.1	Generalized TSI scheme	16
Figure 2.2	Trilayer TSI scheme	17
Figure 2.3	Bilayer TSI Scheme	18
Figure 2.4	CARL TSI process	19
Figure 2.5	Digital silylation TSI scheme	20
Figure 2.6	Graft Polymerization Lithography	22
Figure 3.1	SEM images of lines grafted by Moore's graft polymerization scheme ³¹	25
Figure 3.2	Mechanism for a generalized ATRP polymerization scheme ⁵⁶	27
Figure 3.3	Example of an ATRP initiator ⁵¹	27
Figure 3.4	Nitroxide based free radical polymerization	28

Figure 3.5	Proposed radical graft polymerization scheme	29
Figure 3.6	Proposed synthesis of living free radical initiator.....	30
Figure 3.7	Alternate synthesis of living free radical initiator.....	31
Figure 3.8	Proposed synthesis of an alternate living free radical initiator	32
Figure 3.9	Synthesis of a polymer bound living free radical initiator and the use of that initiator to graft styrene onto the backbone.....	33
Figure 3.10	Irgacure 2959 (left) and Irgacure 184 (right).....	35
Figure 3.11	Proposed synthesis of a polymerizable photo-radical generator.....	35
Figure 3.12	Alternate synthesis of a polymerizable photo-radical generator.....	36
Figure 3.13	Proposed synthesis for a second polymerizable photo-radical generator	36
Figure 3.14	Synthesis of the norbornene-bound photo-radical generator	38
Figure 3.15	Attempted synthesis of a norbornene based, polymer bound PRG	39
Figure 3.16	Synthesis of the dinorbornene-bound PRG.....	39
Figure 3.17	Attempted synthesis of a dinorbornene based, polymer-bound PRG	40
Figure 3.18	Second Attempted synthesis of a dinorbornene based, polymer- bound PRG.....	40
Figure 3.19	Successful synthesis of a dinorbornene based, polymer-bound PRG.....	41
Figure 3.20	Simple exposure chamber schematic	42
Figure 3.21	A photograph of the first “successful” radical graft of this project	43
Figure 3.22	Three schemes for imaging using the radical grafting technique	45
Figure 3.23	Target silicon containing monomers.....	46
Figure 3.24	Synthesis of a difunctional, silicon containing monomer	46

Figure 3.25	Attempted synthesis of a monofunctional, silicon containing monomer	47
Figure 3.26	Second attempted synthesis of a monofunctional, silicon containing monomer	47
Figure 4.1	Schematic of the improved grafting chamber	58
Figure 4.2	Small molecule PRG (left) and Polymer-bound PRG (right)	59
Figure 4.3	Free radical surface grafting of methyl acrylate onto a substrate of polymer bound photo-radical generator coated on silicon. The grafting was done at a temperature of 60°C and a monomer pressure of 42.5 torr. From left to right can be seen: 1) Swelling caused by sorption into the film as the monomer is introduced, 2) Growth as the wafer is exposed to UV light, 3) Cessation of growth as the lamp is turned off, 4) Resumption of growth when the light is turned back on 5) Cessation of growth as the lamp is once again turned off, and 6) Film shrinkage as the monomer is desorbed when the chamber is evacuated.	61
Figure 4.4	Photograph of polymer grafted onto a film of styrene containing Irgacure 2959, a non-bound PRG. As can be seen the surface is quite rough and is unsuitable for lithography.	62
Figure 4.5	Photograph of a polymer grafted onto a film of PRG1, a polymer-bound PRG. This film is quite smooth. The reflection of books can be seen on the wafer.	63
Figure 4.6	Control experiment showing only the absorption and desorption of monomer when no PRG is present. No thickness change was observed when the film was irradiated with UV light.	64
Figure 4.7	Grafting results with the difunctional silicon containing monomer	65
Figure 4.8	Contrast between quenched and unquenched growth	66
Figure 4.9	Pressure dependence of the grafting process	67
Figure 4.10	Source intensity dependence of the grafting process	67
Figure 4.11	Ideal quenching efficiency as a function of quenching dose	69

Figure 4.12	PROLITH Simulation of the aerial image of 160nm nested lines	69
Figure 4.13	Simulated grafted profile given the above aerial image simulation and ideal quenching efficiency	70
Figure 4.14	Linear quenching efficiency as a function of quenching dose.....	70
Figure 4.15	Simulated grafted profile given the above aerial image simulation and linear quenching efficiency	71
Figure 4.16	Actual quenching efficiency data fit with an arbitrary function to match the shape of the data.....	72
Figure 4.17	Simulated grafted profile based on the measured quenching efficiency.....	73
Figure 4.18	SEMs of features printed by contact printing	75
Figure 4.19	Optical micrograph of higher resolution grafted images	76
Figure 4.20	SEM image of 500nm nested lines grafted with MMA.....	76
Figure 4.21	Top down SEM images of the etched wafer fragment	77
Figure 4.22	Higher magnification SEMs of etched, silicon-grafted wafers.....	77
Figure 4.23	Cross section SEMs of etched, silicon-grafted wafers.....	78
Figure 4.24	Schematic of the large wafer chamber.....	80
Figure 4.25	Photograph of the large wafer chamber	81
Figure 4.26	First grafted image using the new tool.....	81
Figure 5.1	Acid base equilibrium	85
Figure 5.2	Initial results for the deprotection of TBOC at 110°C	87
Figure 5.3	Comparison of two batches of the imidazolium triflate salt that had been synthesized and stored under dry conditions.....	88
Figure 5.4	Deprotection of TBOC with triflic acid at low temperatures	89

Figure 5.5	Deprotection of TBOC with an equimolar ratio of triflic acid and imidazole.....	90
Figure 5.6	Deprotection of TBOC with the salt imidazolium triflate	91
Figure 5.7	Comparison of the deprotection of TBOC with triflic acid alone versus a mixture of triflic acid and imidazolium triflate.....	92
Figure 5.8	The difference between the reaction of an amine and an ionic base with an acid. Shown is the reaction of ammonia and TBAH with triflic acid.	94
Figure 6.1	Aerial image isofocal point for 160nm nested lines at 320nm pitch. Shown is aerial image intensity versus horizontal position for four arbitrary focus values. The point where all four lines cross is the isofocal point. Notice the isofocal point is at half the pitch.....	102
Figure 6.2	Summary of the results of PROLITH simulations. In general, acid diffusion lengths greater than base diffusion lengths result in a downward shift in the isofocal CD. The opposite is true for acid diffusion lengths smaller than base diffusion lengths. Also, shifts in the isofocal CD tend to become more pronounced at higher base loadings.	109
Figure 6.3	Observed iso-fading CD through base loading	112
Figure 6.4	Illustration showing how the addition of various levels of base quencher can lead to different types of acid and base profiles in a photoresist film. The solid lines represent acid, and the dotted lines represent base	114
Figure 6.5	Correlation between estimated acid diffusion lengths in arbitrary units with isofocal CD measured by experiment. Diamonds with a solid line are 160nm nominal mask features in a resist containing 10% TOA. Squares with a dotted line are 180nm nominal mask features in a resist containing 40% TDDA, and triangles with a dashed line are 180nm nominal mask features in a resist containing 40% THA. The trend shown matches the trend seen in simulation.....	116
Figure 7.1	(a) Lines printed in a photoresist that does not contain base, (b) Lines printed in a photoresist that does contain base. The edges of the lines in (b) show less roughness than the edges in (a).	123

Figure 7.2	Percentage of blocked polymer sites that remain blocked after exposure and PEB for ten different photoresist formulations. The shape of the dots represents the type of base used. Diamonds represent the no base resist, triangles represent TEA, squares represent TOA and circles represent TBAH. The color of the points represents the base loading. Solid black points represent a molar loading of 5% relative to PAG, while hollow points represent a loading of 10%, and solid grey points represent a loading of 20%.....	124
Figure 7.3	This figure shows a comparison of the model fit to experimental data for the contrast model presented. The shape of the dots represents the type of base used. Diamonds represent the no base resist, triangles represent TEA, squares represent TOA and circles represent TBAH. The color of the points represents the base loading. Solid black points represent a molar loading of 5% relative to PAG, while hollow points represent a loading of 10%, and solid grey points represent a loading of 20%. The model fits for the 0%, 5%, 10%, and 20% base loadings are shown by the dotted grey line, the solid black line, the dotted black line, and the solid grey line respectively.	127
Figure 7.4	Simulation results showing the tradeoff between contrast enhancements and photospeed achieved by adding base.....	128
Figure 7.5	Observed trends of LER with base loading and PEB temperature	129
Figure 7.6	Fraction of blocked polymer remaining after PEB	134
Figure 7.7	CD data through AMag and dose for the 20% base resist	135
Figure 7.8	3 σ LER data through AMag and dose for the 20% base resist.....	135
Figure 7.9	CD SEM images of lines in resist showing the effect of asymmetric magnification and base loading on line-edge roughness.....	136
Figure 7.10	The ILS dependence of LER through base loading	137
Figure 7.11	Resist 3 σ LER through base loading at a fixed ILS of 20 μm^{-1}	138
Figure 7.12	Model fit for reaction kinetics. The points represent data while the solid lines represent the model fit.	140

Figure 7.13	Simulated chemical contrast as a function of base loading	141
Figure 7.14	Example data for the conversion of an aerial image into a polymer latent image through the use of the kinetic model	142
Figure 7.15	LER plotted as a function of PPG.....	143

Chapter 1: Traditional Photolithography

1.1 INTRODUCTION AND MOORE'S LAW

Over the years the semiconductor industry has undergone a great deal of change, but one factor has remained the same. This factor has been the ever present drive to print smaller and smaller features onto silicon wafers. Shrinking the printed features on microchips presents two major advantages. First, smaller transistors offer improved device performance,^{1,2} but perhaps the more important advantage is economics. The cost to process a silicon wafer from start to finish is roughly constant regardless of whether the wafer has one chip on it or whether it has one thousand.¹ By printing smaller features, more transistors can be fit onto a single chip and more chips can be fit onto a single wafer. The more chips that can be produced on a single wafer, the more profitable is that wafer.

Gordon Moore, former CEO of Intel, noticed a trend in this miniaturization. He noticed that the number of transistors per square inch of silicon wafer tended to double every 12-24 months.³ This observation, often called Moore's law, has held roughly true for over four decades of device manufacturing and has become a very important idea in the semiconductor industry. This concept has, in a sense, become the driving force for research and development in the industry, and considering the many different things that must come together to create a functional device, the fact that this trend has held true for decades is quite remarkable. Figure 1.1 shows an illustration of Moore's law over the past few decades.⁴ Research described in this dissertation was performed with the goal in mind of adding to the body of knowledge of the semiconductor industry to further advance development along this trend.

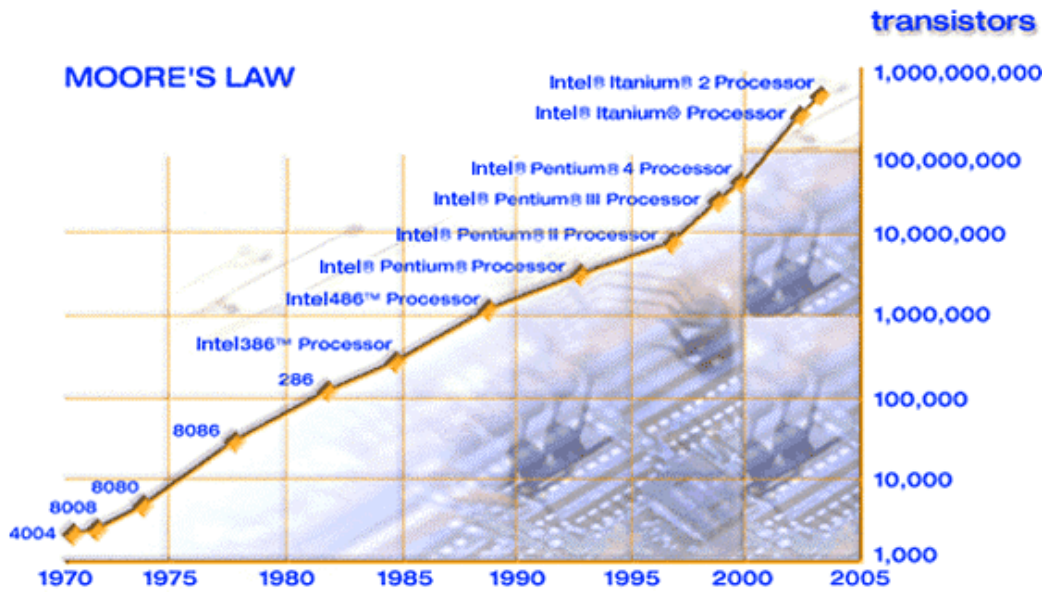


Figure 1.1 Moore's law⁴

1.2 DEVICE FABRICATION AND LITHOGRAPHY

Almost every step in the fabrication of a modern device requires patterning of some kind. Current state of the art microchips contain multiple levels of wiring used to interconnect various transistors and other devices printed directly onto the silicon wafer. Figure 1.2 shows multiple levels of patterned copper wiring on a microchip. The process of lithography is used to perform these patterning steps. In this process, a layer of polymer called a photoresist is coated on top of the substrate to be patterned. A photoresist is a specially designed material that performs two functions. First, a photoresist must undergo a solubility change on exposure to ultraviolet (UV) light. In the case of positive tone resists, irradiating the polymer film with UV light changes the film from insoluble to soluble in aqueous base developer. Negative tone resists do the opposite. The second function of a photoresist is to resist subsequent processing, which

is generally either an etch process or an ion implant process. The photoresist is exposed to UV light through a photomask, resulting in the pattern contained on the mask being projected onto the resist. This irradiation causes a change in the solubility of the exposed areas of the resist. The wafer is then immersed in an aqueous base developer, which washes away the soluble areas of the photoresist. The now exposed substrate can then be etched or implanted as required.¹ The process of lithography is shown in Figure 1.3 below.

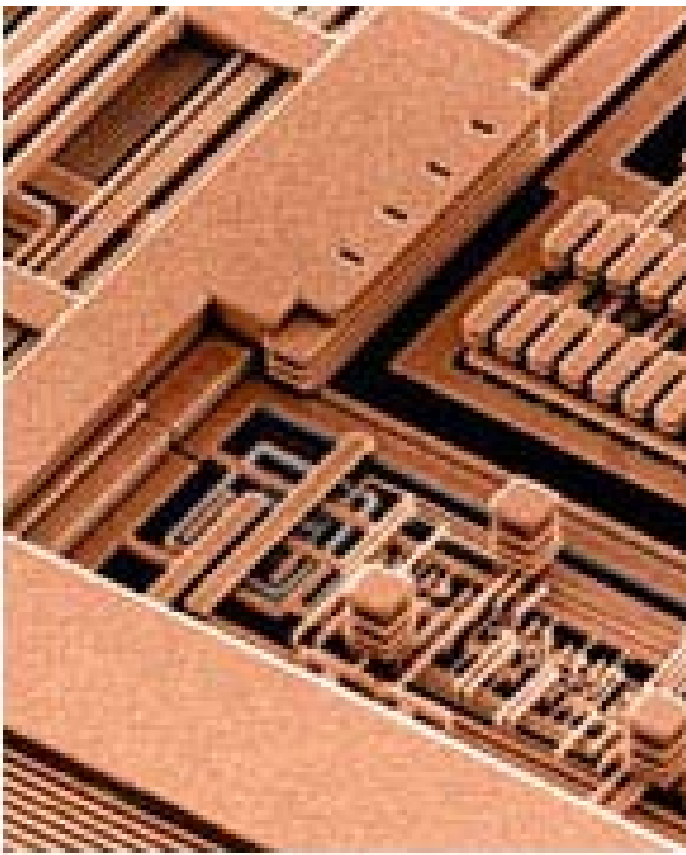


Figure 1.2 Multiple levels of patterned copper wires on a semiconductor device⁵

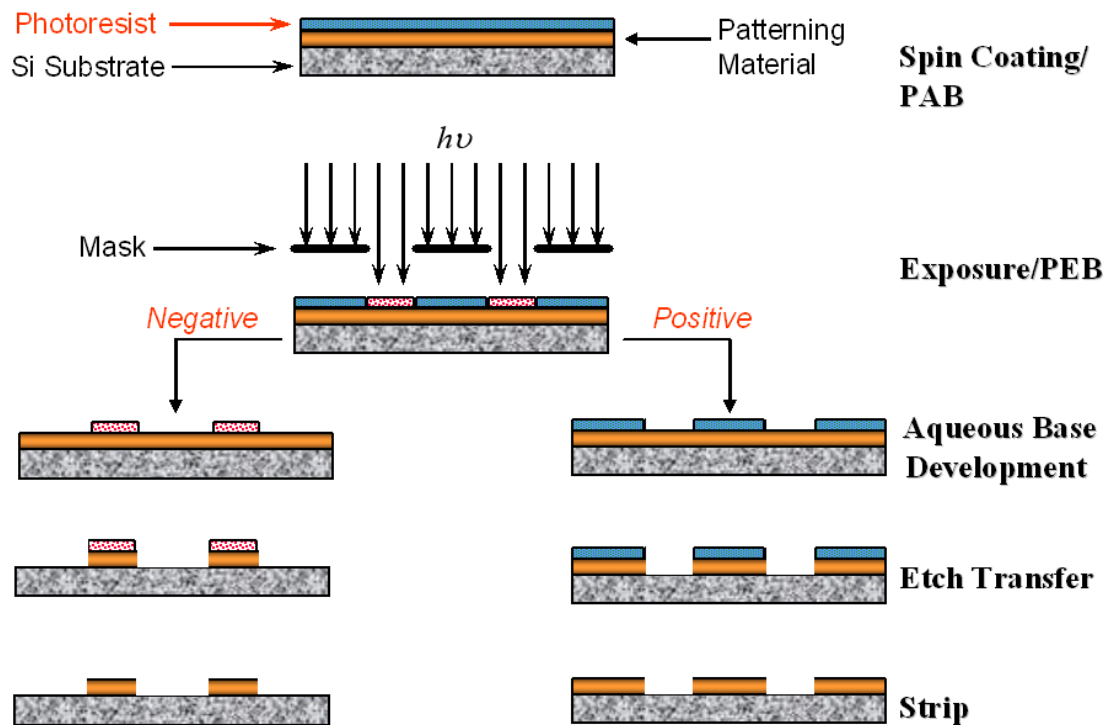


Figure 1.3 The lithography process

1.3 EXPOSURE

During the exposure process, the pattern from the mask is not directly reproduced on the wafer. Diffraction effects serve to blur the aerial image and degrade it from an ideal perfect square wave form.⁶ Figure 1.4 shows this blurring process. Diffraction effects increase as the mask feature size becomes smaller; hence, as features on the mask become smaller, diffraction effects make it harder to resolve that feature until eventually, no feature can be printed at all. According to Moore's law, however, semiconductor manufacturers must continue to shrink the size of transistors to keep pace with the industry. As a result, researchers must cleverly search for new and improved methods for printing smaller and smaller features.

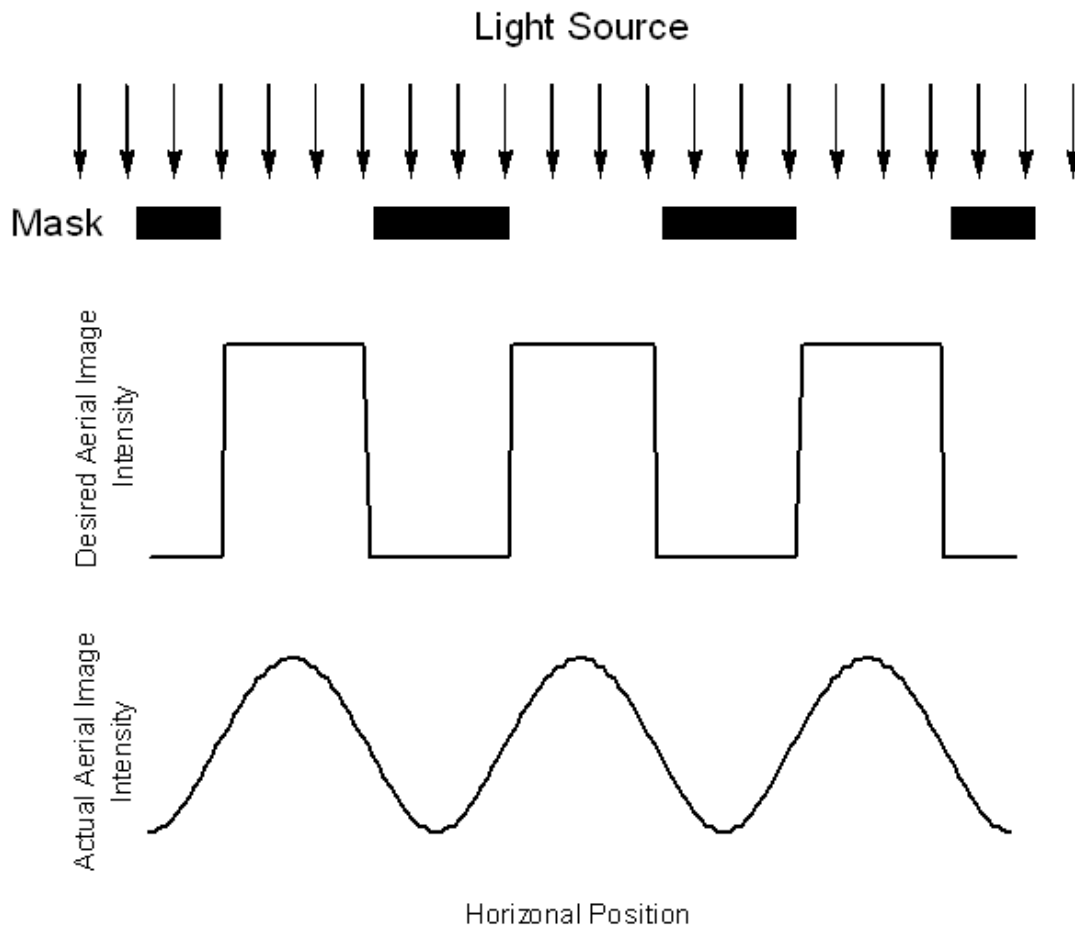


Figure 1.4 Diffraction induced blurring of an aerial image from an ideal square wave to what is actually seen

This smallest feature that can be printed on a wafer using conventional lithographic processes is limited by how well light can be focused onto the resist. Additionally, the light must remain focused throughout the entire thickness of the resist. The following lens laws describe the theoretical resolution limit of the exposure process. These equations are often referred to as the Rayleigh lens laws or the Rayleigh criteria.^{1,2,6}

$$R \propto \frac{\lambda}{NA} \quad (1.1)$$

$$DOF \propto \frac{\lambda}{NA^2} \quad (1.2)$$

In these equations, R is the resolution limit of the system, λ is the wavelength of the light used to print the image, NA is the numerical aperture of the lens, and DOF is the depth of focus of a feature at the resolution limit of the system. As can be seen, the minimum feature size can be decreased by increasing the numerical aperture of the lens or by decreasing the wavelength of the incident light. Increasing the numerical aperture of the lens is very expensive and carries with it a large penalty in terms of depth of focus. The other alternative is to print features using light of shorter wavelength. This solution too, however, presents challenges to overcome. Chief among these challenges is the development of new resist materials that are transparent at shorter wavelengths. This task seems particularly challenging considering the fact that the resist must also contain a chemically triggered solubility switch. In addition to materials concerns, one must also consider the loss of depth of focus associated with decreasing wavelengths of light. Despite these challenges, researchers have been decreasing the exposure wavelength used in lithography for decades. Significant advances in photoresist technology have been necessary to keep pace with this reduction of wavelength. The following section describes the general principles behind which photoresists operate, the chemical processes involved in the solubility switch of several common photoresists, and the evolution of the modern photoresist.

1.4 THE PHOTORESIST

1.4.1 Non Chemically Amplified Resists

Photoresists have been around for a long time, and a number of different types have been used over the years. The earliest photoresists were developed for photography applications in the early 19th century.⁷ These early resists have evolved a great deal over the years from early photographic materials to dichromated gelatins, which were used to manufacture the first semiconductor devices, to bis(arylazide)-rubber resists, which were used in integrated circuit manufacturing from the 1950s to the 1970s, to diazonaphthoquinone (DNQ) novolac resists, which are still in use today.^{1,7} Although these resists are all very different, they all work by the same principle. Each photoresist can be imaged because it has a light induced solubility switch. In the case of the DNQ/novolac system, a polymer film of novolac is coated onto a silicon wafer. Dispersed in this film is a small amount of DNQ. This film, as coated, is insoluble in aqueous base developer. As the film is irradiated with 365nm ultraviolet (UV) light, the DNQ undergoes a chemical reaction, and although the novolac resin is unchanged, the conversion of the DNQ to a more soluble species is enough to render the film soluble in aqueous base developer. Figure 1.5 shows this switch in the DNQ/novolac system.

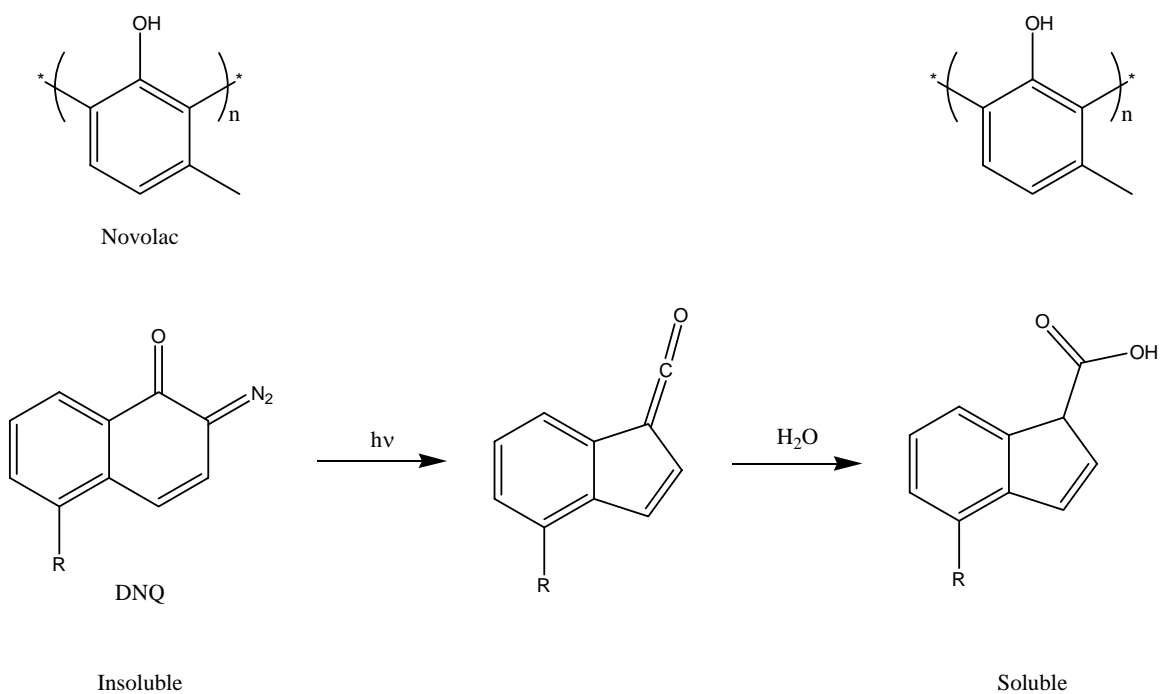


Figure 1.5 Solubility switch in the DNQ/novolac photoresist system

This solubility change is illustrated graphically in Figure 1.6 below.⁸ This plot shows the effect of photoactive compound (PAC) concentration, in this case the PAC is DNQ, on the solubility of both exposed and unexposed films of this resist. As can be seen, the addition of DNQ actually slows the dissolution rate of novolac in aqueous base developer. Upon irradiation with UV light, however, the DNQ undergoes the chemical reaction described above and the dissolution rate of the film becomes much higher.

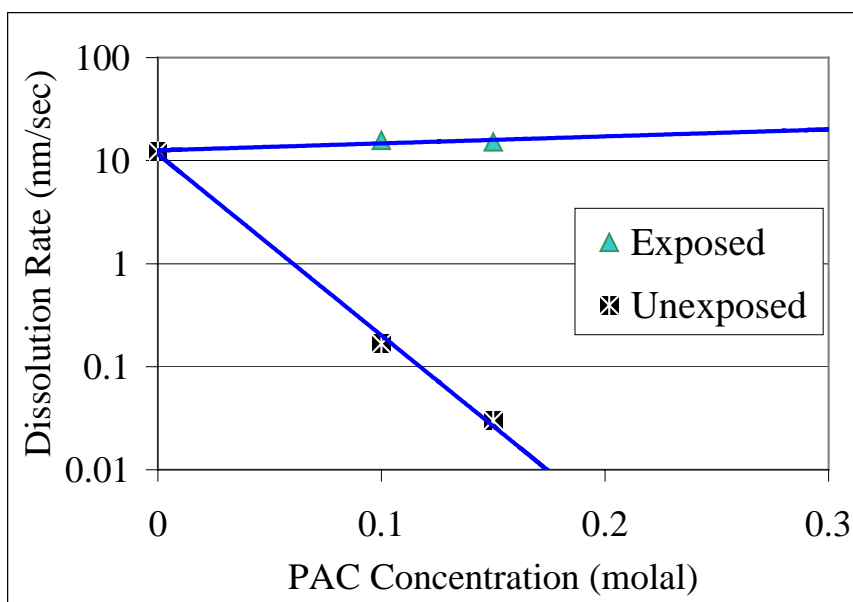


Figure 1.6 Solubility change upon exposure of a DNQ/novolac resist as a function of DNQ loading⁸

A number of modifications and improvements to this basic resist design have been made over the years, but extension of this platform to wavelengths of light below approximately 300nm has been impossible because of the absorbance of the novolac resin.^{1,9} The use of lower wavelengths is desirable, as described previously, because patterning performed with lower wavelengths of light allow smaller features to be printed. To extend photoresist technology to the next generation, researchers had to develop a new type of photoresist, the chemically amplified resist (CAR).

1.4.2 Chemically Amplified Resists

To reduce exposure wavelengths to 248nm, the next target illumination wavelength for the semiconductor industry, two problems had to be solved. First, a polymer that is transparent at that wavelength had to be found. Second, a way to

overcome the reduced light intensity of the mercury arc lamp at 248nm had to be found.² The first problem was solved by switching to a poly(4-hydroxystyrene) (PHOST) based system. The second problem was solved in two ways. First, the exposure source was changed from a mercury arc lamp to a KrF excimer laser. This tool offered an improved output intensity at 248nm as compared to a mercury arc lamp. Second, a system of amplification was developed to improve the sensitivity of the resist to light. This system was based on the idea that each photon incident on the photoresist could initiate a multitude of chemical reactions as opposed to previous systems, which allowed each photon to induce at most one reaction. This increased sensitivity to light became known as chemical amplification, and resists that used this system became known as chemically amplified resists (CARs).¹

Chemically amplified resists are based on the idea of catalysis. In general, CARs consist of a polymer with a small amount of photoacid generator (PAG) blended in. This PAG generates a strong acid on exposure to UV light. This acid then catalyzes a chemical reaction that causes a solubility switch in the polymer. One of the earliest and most well known CAR is based on tert-butyloxycarbonate protected PHOST. This protected polymer is often simply called TBOC for short. The protected polymer, TBOC, is insoluble in aqueous base developer, but the deprotected version, PHOST, is very soluble. The protecting group can be removed at elevated temperatures through a process that is catalyzed by acid. Figure 1.7 shows this entire process. Pictured is the common PAG triphenylsulfonium hexafluoroantimonate being converted to hexafluoroantimonic acid upon irradiation with 248nm light. Also shown is the conversion of TBOC to PHOST, resulting in the generation of volatile byproducts carbon dioxide and isobutylene. The plot in the upper right-hand corner of this figure shows how the deprotection reaction is catalyzed in the presence of acid. These curves show the

normalized mass of a sample of TBOC both with and without the presence of acid. As can be seen, the polymer sample containing acid undergoes decomposition at a temperature of around 100°C while the acid free sample remains stable until around 200°C. By performing a post exposure bake (PEB) of the resist between these two temperatures, the deprotection reaction resulting in a solubility switch will occur only in areas that have been exposed to light and hence contain acid.

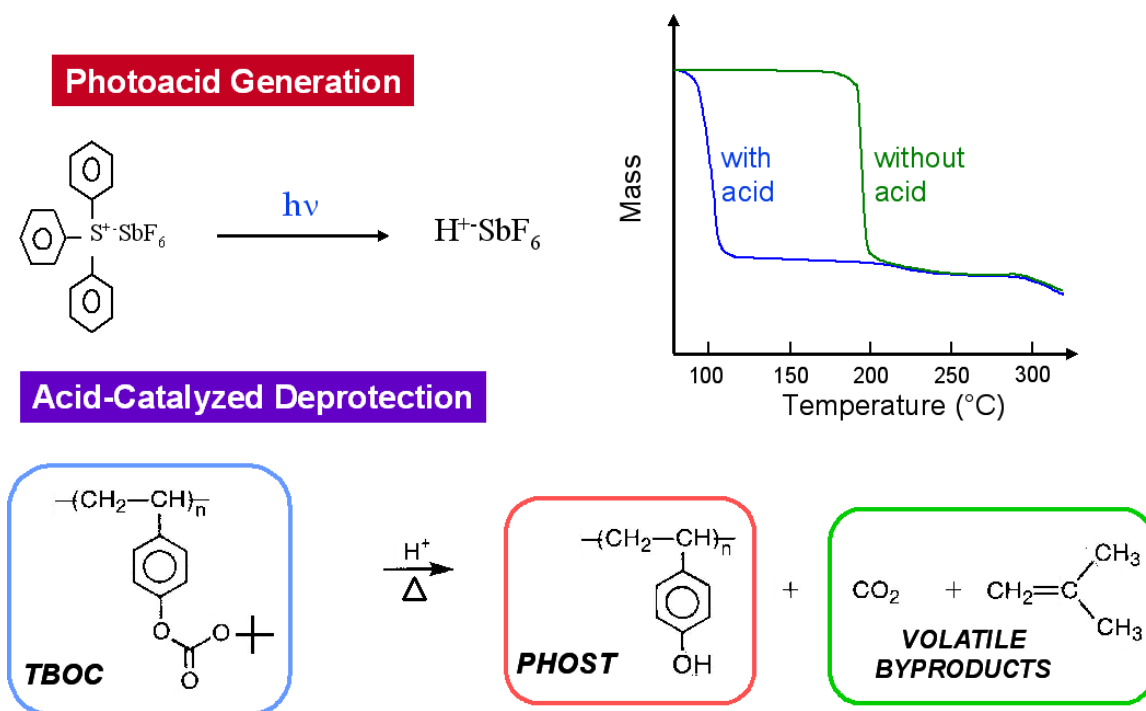


Figure 1.7 The chemistry of TBOC based chemically amplified resists¹

A vast number of variations on this theme of using CARs for 248nm lithography have been developed. Some are based on acid catalyzed crosslinking schemes so as to make a negative tone photoresist. Others have used acrylate or acetal protecting groups instead of the carbonate group that has been shown.^{1,10-12} These variations combined with

advances in mask and stepper technology such as the development of phase shift masks and alternate illumination schemes^{1,2,6} have extended the capabilities of 248nm lithography, but the need for smaller features persists. As a result, researchers continue to work to develop resists for lower wavelengths. The next wavelength of interest for lithography is 193nm, the wavelength emitted by an ArF excimer laser. To achieve transparency at this wavelength, no aromatic species could be included. As with 248nm resists, researchers have developed a number of different variations. Figure 1.8 below shows a few examples of 193nm resists.¹³

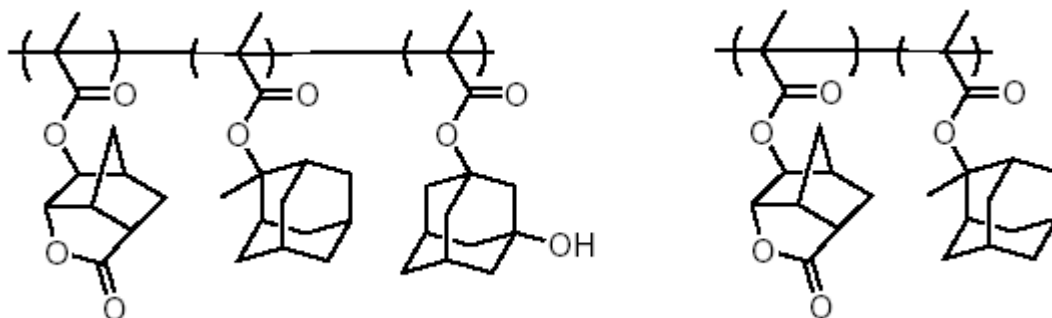


Figure 1.8 193nm photoresists

Integrated circuit manufacturers are already using 193nm lithography for commercial manufacturing and have been for several years¹⁴. As for the next generation beyond 193nm, the future is unclear. Today, much work is being done to develop an immersion stepper for 193nm lithography to extend that technology as far as possible.¹⁵⁻¹⁸ Beyond this step, there is much debate as to what the future will hold. Much work has been done to incorporate fluorine into a photoresist to make it transparent to 157nm light.^{19,20} Other researchers have worked on non-conventional lithography techniques

such as imprint lithography.²¹ Whatever the future may hold, it is clear that there will be many interesting challenges to overcome.

Chapter 2: Top Surface Imaging

2.1 INTRODUCTION

As described in previous sections, the semiconductor industry is constantly driven to produce components that are faster and cheaper than ever before. One way to lower the cost and boost the performance of microelectronic circuits is to print smaller features on the chip. Printing smaller features allow the manufacturer to pack more chips onto one wafer and to pack more transistors onto a chip. The downside is that printing smaller and smaller features has proven to be an increasingly difficult challenge. The Rayleigh lens laws, as described in Equations 1.1 and 1.2 describe the resolution and depth of focus limits of the lithography process. Also described previously are the many challenges associated with lithography.

In light of these challenges, alternative approaches to conventional lithography have been considered. One such approach is top surface imaging (TSI), an approach to lithography that requires only that the very top layer of the resist be exposed to light. This process eliminates the transparency requirement of the resist and significantly reduces the depth of focus requirement. Furthermore, top surface imaging does not require a chemically active transfer layer as does conventional photolithography. Finally, TSI eliminates added complexity to the imaging process caused by reflections from the substrate, such as standing waves, because the light does not penetrate beyond the top layer of the resist. Subsequent sections outline various TSI schemes that have been developed.

2.2 TOP SURFACE IMAGING

A number of different schemes for top surface imaging have been developed, although perhaps top layer imaging is a more appropriate name for these techniques. In general, these techniques all rely on a similar basic mechanism. First, the top portion of the film is patterned in some way with a material that possesses etch resistance. This patterned, etch resistant material is then used as a mask during an etch process that transfers the pattern to the underlying substrate. This etch process is usually done in two steps. First a dry develop step is used to clear away the unexposed TSI material. Then the pattern is transferred to the underlying substrate. The reason dry etch is so often used in TSI schemes is that it is one of the few techniques available that provides an anisotropic method for pattern transfer, and only a relatively thin patterned layer at the top surface of the wafer is required as a mask to generate high aspect ratio pattern transferred images. Figure 2.1 below shows a generalized scheme for TSI and several different TSI schemes are described in subsequent sections.

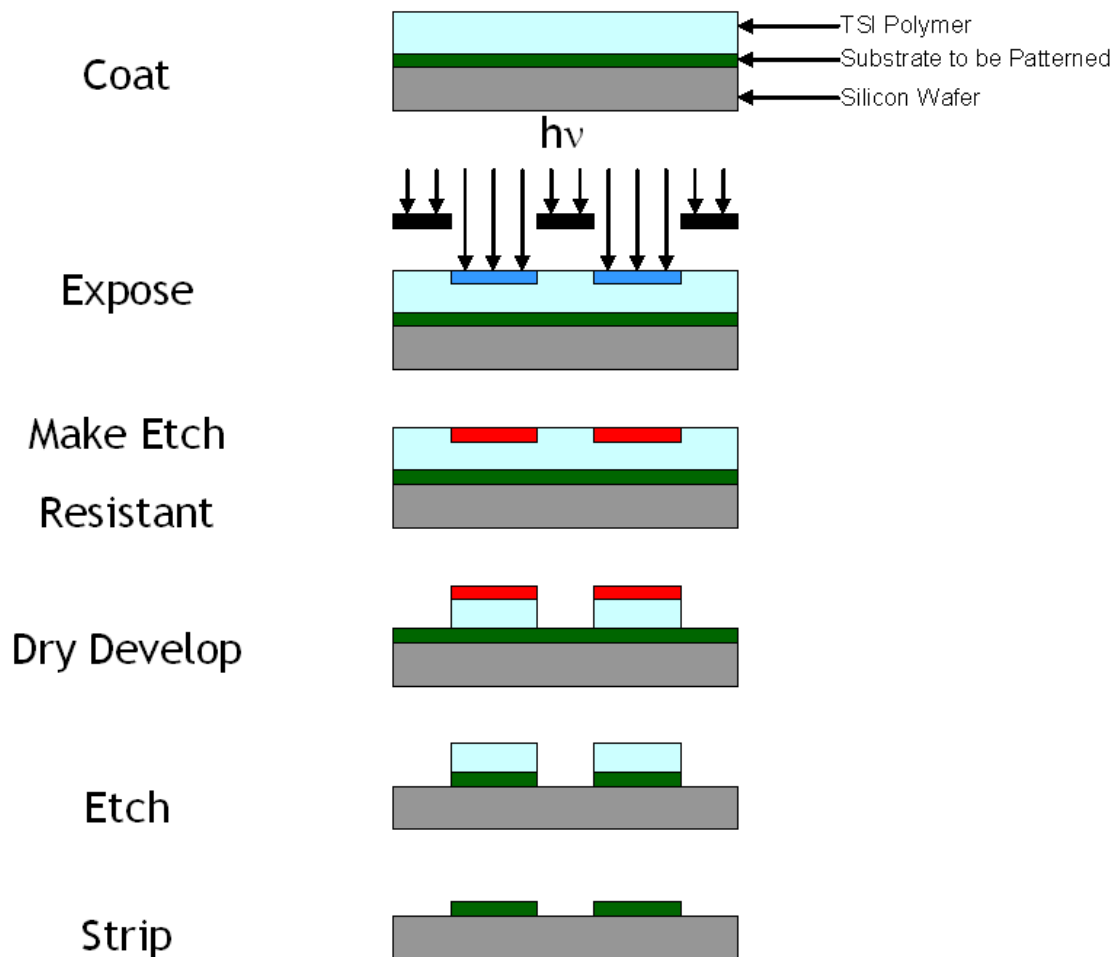


Figure 2.1 Generalized TSI scheme

2.3 MULTILAYER RESISTS

Perhaps the most straightforward technique for TSI is the use of multilayer resists.²² In this technique, multiple layers of material are coated, the top-most of which is patternable. Several multilayer techniques have been developed. For example, one scheme requiring three layers involves coating a thick layer of sacrificial material to provide high aspect ratio pattern, a thin layer of silicon containing material that provides

oxygen etch resistance, and a thin layer of photoresist that can be patterned in the normal manner and also provides fluorocarbon etch resistance. In this scheme, the top layer of resist is patterned in the traditional manner, a CF_4 etch is used to transfer the pattern into the silicon containing layer, and an oxygen etch is used to transfer the pattern into the substrate. Figure 2.2 shows this process with a negative tone resist.

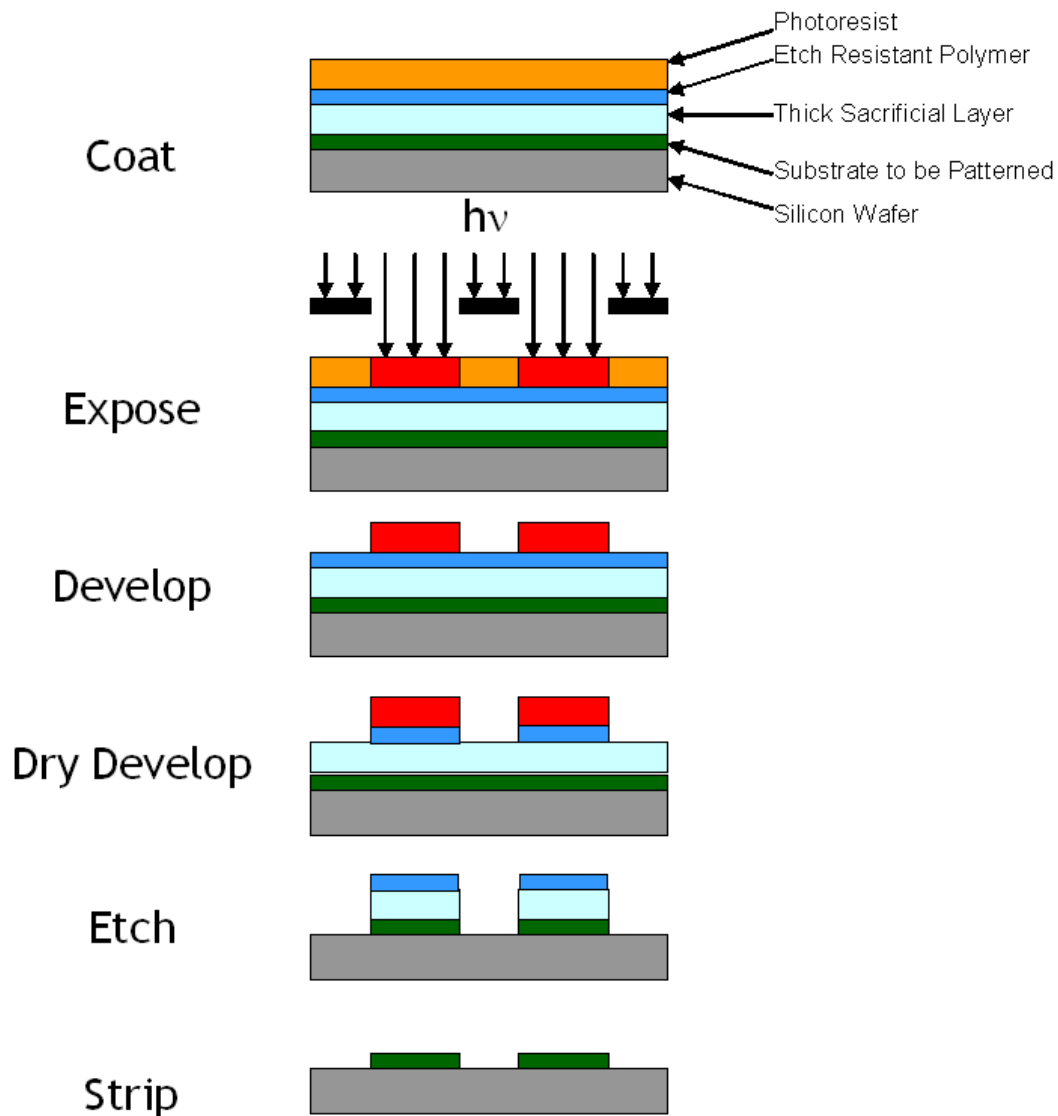


Figure 2.2 Trilayer TSI scheme

A variation on this scheme involves only two layers. In this variation, the patternable layer contains silicon, eliminating the need for the layer of silicon containing material. The challenge with this technique is the development of a resist that contains all the requisite functional groups that provide a solubility switch while maintaining adequate silicon content for etch resistance. Figure 2.3 shows this process using a negative tone resist.

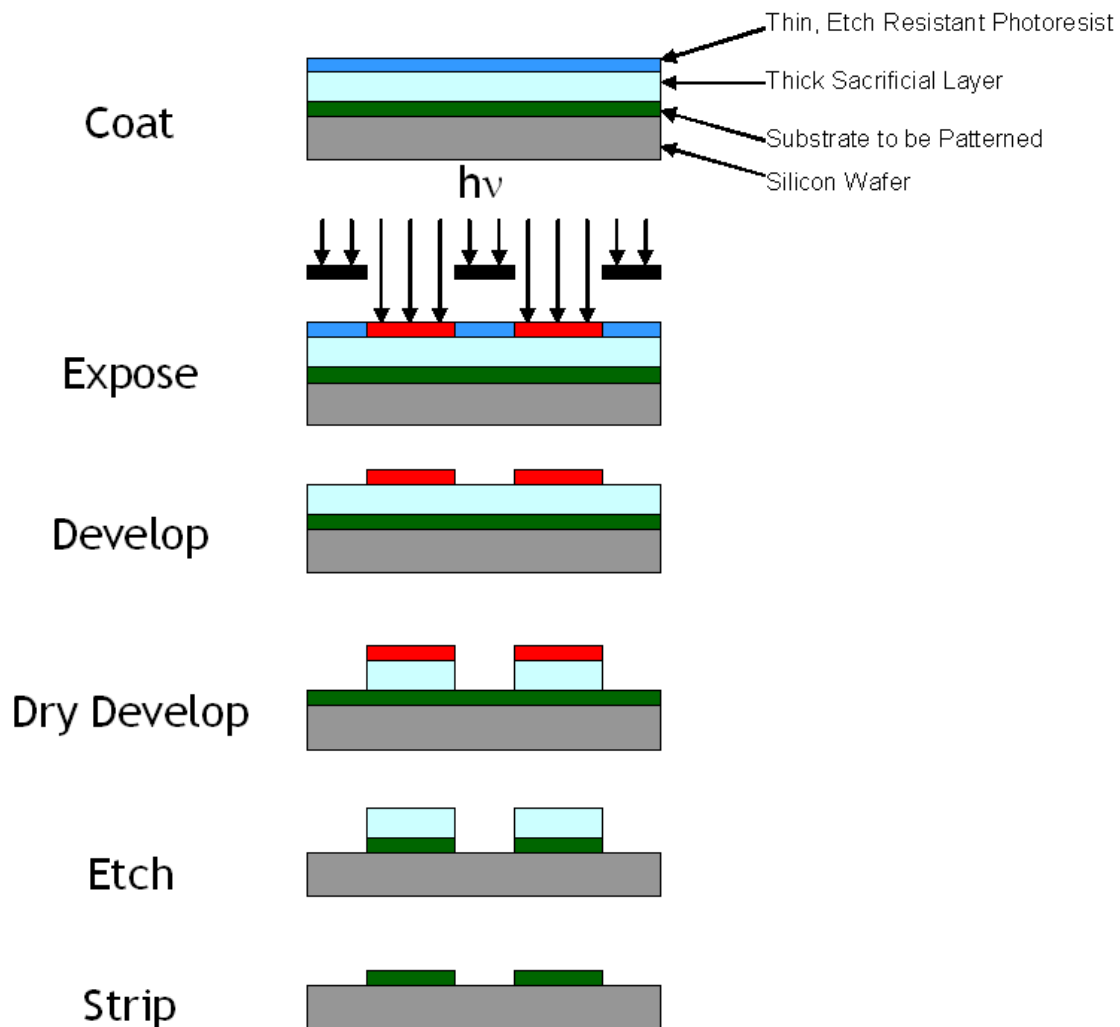


Figure 2.3 Bilayer TSI Scheme

2.4 CARL PROCESS

A process called Si-CARL (Silicon Chemical Amplification of Resist Lines) or just CARL for short provides an interesting twist on bilayer TSI.^{23,24} In this process, a thin photoresist is coated on top of a substrate, but after patterning the resist in the conventional manner, the wafer is immersed in a liquid silylation agent, which causes silicon to become incorporated into the lines of resist. These resist lines now have a high resistance to oxygen etch, which can then be used to transfer their pattern to the underlying substrate. Figure 2.4 shows this process. Once again, a negative tone photoresist is shown.

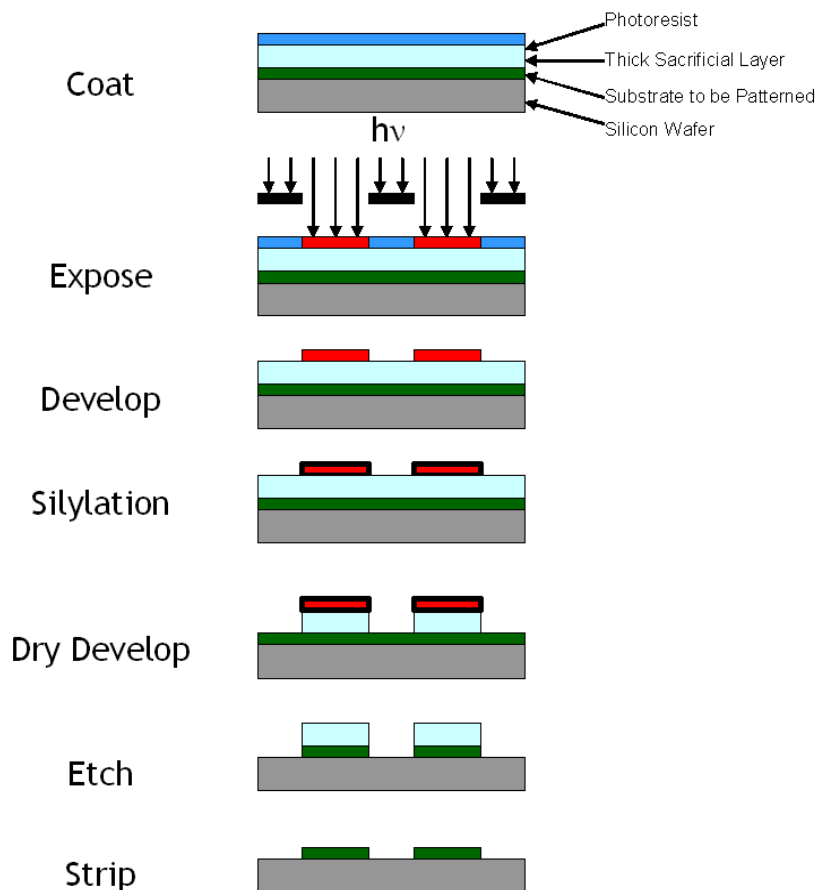


Figure 2.4 CARL TSI process

2.5 DIGITAL SILYLATION

The digital silylation process, similar to the CARL process, uses a gas phase silylation agent instead of a liquid agent and eliminates the develop step.²⁵⁻²⁸ In this process, a photoresist is coated and post exposure baked (PEB), but not developed. After the PEB, these wafers are exposed to a gas phase silylation agent, which is reactive towards the deprotected polymer but not towards the protected polymer. In this manner the deprotected areas of the photoresist have silicon incorporated into them; hence, they become etch resistant to oxygen etch. Figure 2.5 shows this process.

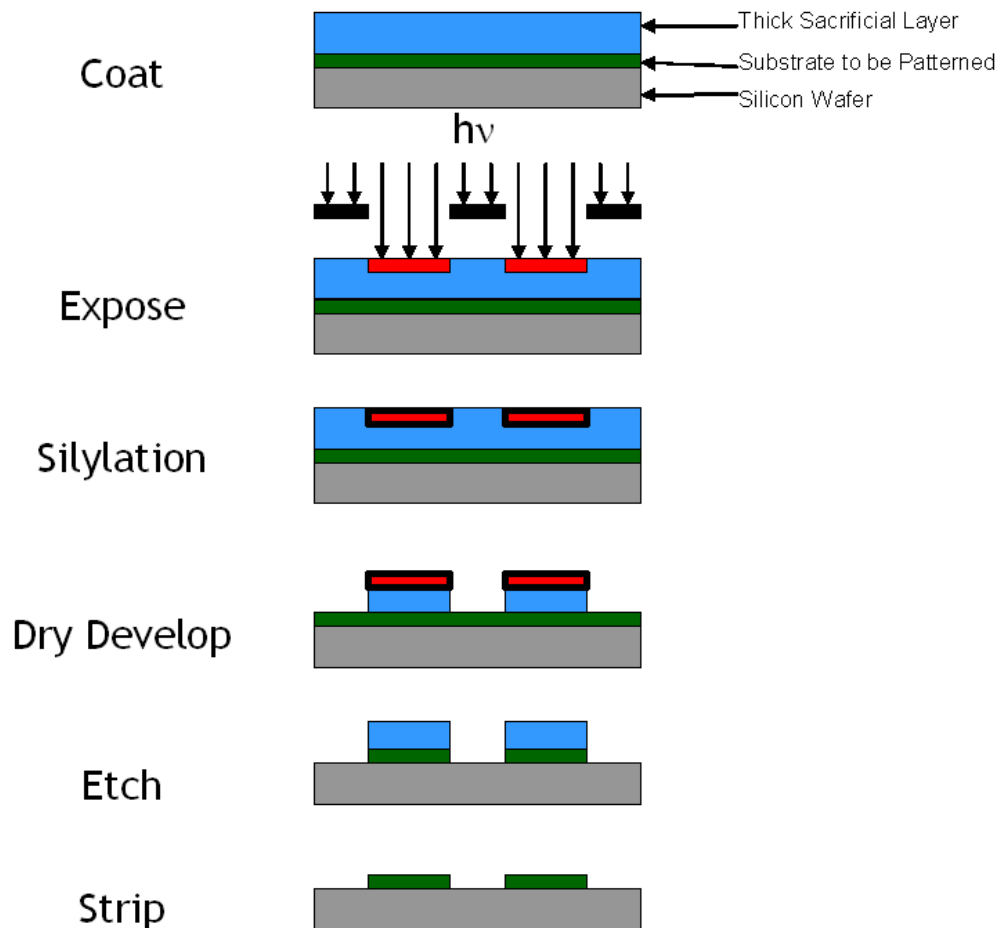


Figure 2.5 Digital silylation TSI scheme

2.6 GRAFT POLYMERIZATION LITHOGRAPHY

One particular method of top surface imaging is known as graft polymerization lithography.²⁹⁻³² The idea behind graft polymerization lithography is to develop a true TSI technique as opposed to a top layer imaging technique. In this process, the etch resistant material is grafted onto the surface, so theoretically, only the very top of the resist is needed. This process begins when light is shined onto the top layer of a resist. In the exposed area, the resist is activated towards polymerization. At this point, monomer is introduced above the resist, and the activated areas of the resist combine with the gas phase monomer to form a layer of polymer, which acts as an etch barrier. The resist can then be developed, etched, and stripped, the net result of which is the formation of a feature on the underlying substrate. The monomer used in this process must meet several constraints in order to function properly. It must be volatile enough to be introduced in the gas phase, must contain enough silicon to function as an etch barrier, and must be reactive towards polymerization. This process is illustrated in Figure 2.6 below.

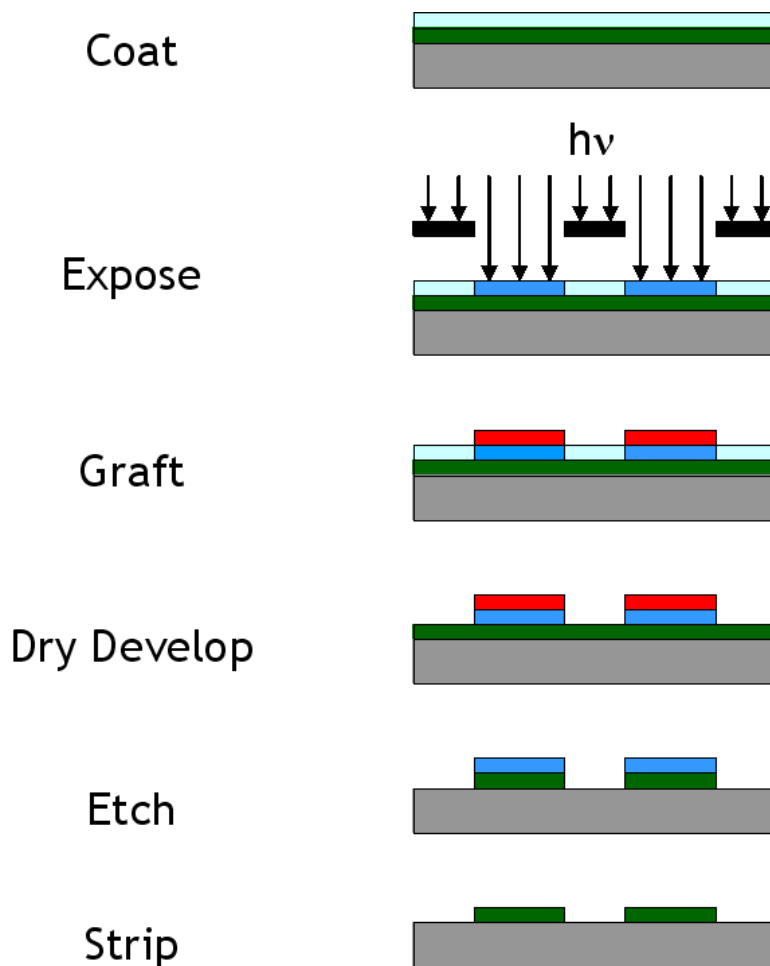


Figure 2.6 Graft Polymerization Lithography

Researchers at The University of Texas at Austin have developed a graft polymerization scheme that uses cations as the initiation mechanism for polymerization.²⁹ This technique has shown promising results, but is limited with regard to the types of monomers that can be used. Of course, only monomers that are reactive towards cationic polymerization such as epoxides and vinyl ethers are usable in this process, and given this constraint along with the requirements for silicon content and volatility, the choices of monomers is quite limited. Also, only a handful of photo-acid generators are strong

enough to initiate cationic polymerizations. Finally, cationic grafting is quite sensitive to airborne base contamination, which has been attributed as the cause of large day-to-day process variations.

Chapter 3: A Free Radical Scheme for Top Surface Imaging

In light of the disadvantages of cationic graft polymerization lithography, as mentioned in section 2.6, it has been proposed that a free radical scheme for graft polymerization lithography be developed. A free radical initiation mechanism provides access to a new library of monomer types that are reactive towards radical polymerization, and free radicals are not sensitive towards basic contaminants. Perhaps the greatest advantage of a free radical scheme is that a much wider array of initiators and initiator chemistries are available. Whereas only a handful of photo-acid generators are strong enough to initiate cationic polymerizations, a number of commercially available and easily synthesized photo-radical generators are available. Of course there are associated disadvantages to the use of radicals as well, the most prominent of which is the fact that radicals can be quenched by oxygen. This section describes the development of a process and the synthesis of materials for free radical graft polymerization lithography.

3.1 INTRODUCTION TO FREE RADICAL GRAFTING

A wealth of literature references that describe liquid phase radical graft polymerization are available,³³⁻³⁹ but far fewer references describing surface grafting from the gas phase are available.^{40,41} Because it is desirable to conduct graft polymerization lithography in the gas phase, early efforts have focused on the development of a system that would allow us to demonstrate the feasibility of this process.

Patterned free radical grafting from the gas phase has been demonstrated in literature previously.^{31,32} Researchers at Rensselaer Polytechnic Institute in collaboration with IBM used electron beams to cleave bonds in poly(methyl methacrylate) (PMMA) and generate radicals. They then exposed the wafer to vapor from acrylic acid to grow

grafts of poly(acrylic acid) on the PMMA film. He then used an organic developer to selectively dissolve the PMMA away. Figure 3.1 shows lines generated by this process

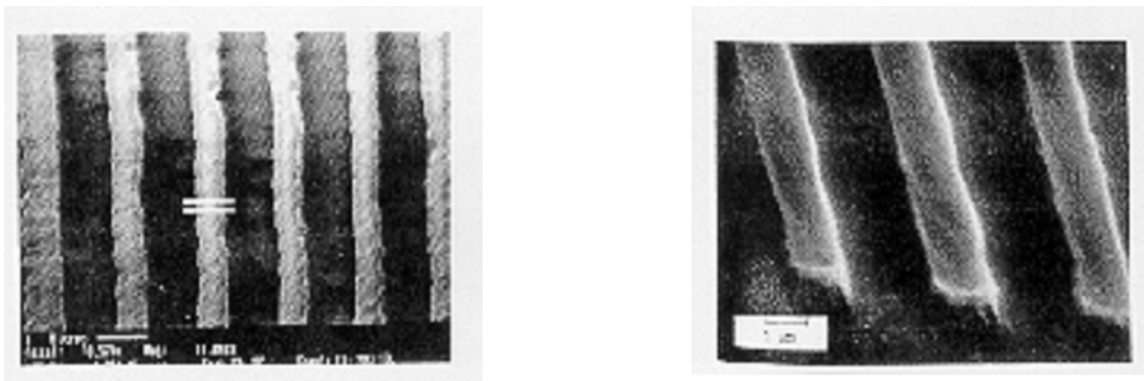


Figure 3.1 SEM images of lines grafted by Moore's graft polymerization scheme³¹

3.2 A LIVING FREE RADICAL PROCESS

From the standpoint of designing a grafting process, the main difference between cationic and free radical grafting is the fact that free radicals are easily quenched by oxygen. The implication of this statement is that the entire process by which cationic grafting is performed will not be amiable to free radical grafting. To avoid having to develop a completely new process, initial efforts focused on developing a living free radical initiator for grafting. Living free radicals are not quenched by oxygen, and hence could be simply substituted into the existing cationic process.

3.2.1 Introduction to Living Free Radical Polymerization

A number of schemes for living free radical polymerization (LFRP) exist, but all types of LFRP operate in the same general way. These schemes all employ different methods to stabilize the radical on the growing chain end. The stabilization must be

strong enough to ensure that the growing chain end is not reactive towards oxygen but still remains reactive enough to incorporate additional monomer units. Several schemes for LFRP are nitroxide mediated living free radical polymerization (NMP),⁴²⁻⁴⁸ atom transfer radical polymerization (ATRP),⁴⁹⁻⁵² group transfer polymerization (GTP),^{53,54} reversible addition-fragmentation chain-transfer polymerization (RAFT),⁵⁵ and iniferters.³³ Subsequent sections describe the two most common methods for LFRP, atom transfer radical polymerization and nitroxide mediated polymerization.

Atom Transfer Radical Polymerization

Atom transfer radical polymerization was developed in the mid 1990s by three different groups, each of which used a slightly different method. ATRP uses the addition of a stabilizing species to the reaction mixture. Matyjaszewski *et al.* pioneered the use of copper complexes as ATRP stabilization agents.⁴⁹ Sawamoto *et al.* developed ruthenium and aluminum based complexes,⁵² and Percec *et al.* used sulfonyl chlorides to initiate the reaction.⁵⁶ Figure 3.2 below shows the mechanism of an ATRP polymerization initiated with a sulfonyl chloride. Figure 3.3 below shows a copper complex that can also be used as a polymerization initiator. Because of the wide variety of initiators that can be used, ATRP has the widest functional group tolerance for LFRP, but because of issues with residual metal contamination, ATRP does not seem an ideal candidate for lithographic applications.

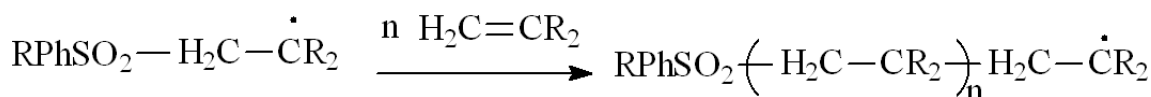
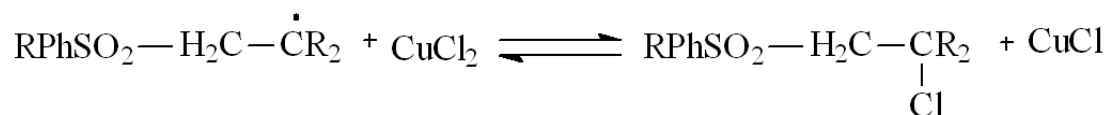
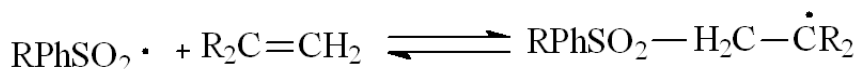
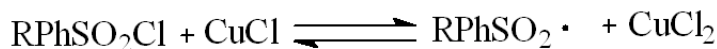


Figure 3.2 Mechanism for a generalized ATRP polymerization scheme⁵⁶

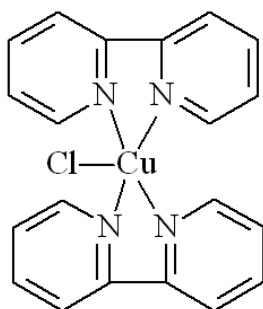


Figure 3.3 Example of an ATRP initiator⁵¹

Nitroxide Mediated Living Free Radical Polymerization

Over the past several years, much work has been done in developing nitroxide-based initiators for radical polymerizations.⁴²⁻⁴⁸ These initiators are predominantly based on the stable free radical 2,2,6,6-tetramethylpiperidinyloxy (TEMPO). In this scheme, TEMPO can be attached to any number of different compounds to create a “macroinitiator” for radical polymerization. At elevated temperatures, usually around 130°C, an equilibrium is established between the macroinitiator and the corresponding

free radicals. The radicals are then able to initiate a free radical polymerization if any monomer units are present. This scheme is shown below in Figure 3.4.

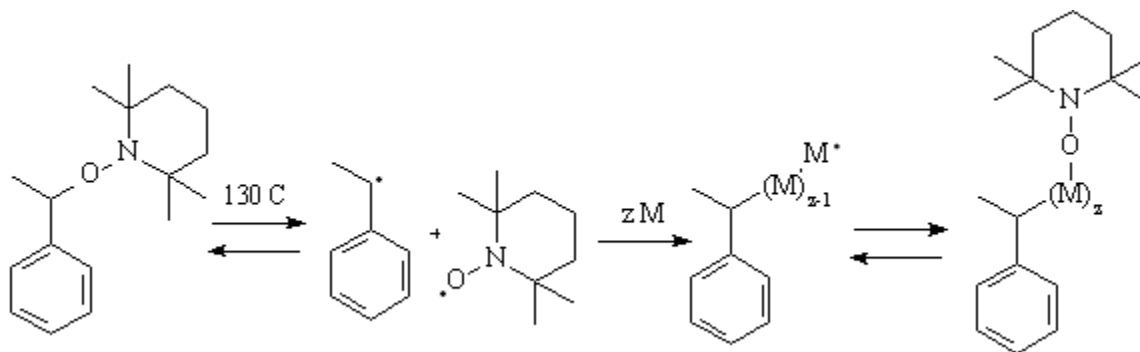


Figure 3.4 Nitroxide based free radical polymerization

3.2.2 Development of a Living Free Radical Initiator for TSI

Nitroxide based living free radical polymerization was chosen as the optimal platform for graft polymerization lithography. It does not use metals, which are undesirable in the semiconductor industry, as does ATRP, and nitroxide based initiators are fairly accessible synthetically. Furthermore, it was decided that rather than create an initiator that is simply physically mixed in with a base layer material, as in the cationic process, to instead create a polymer bound initiator and use that polymer as the base layer material. Creating this compound with a free radical system is relatively simple compared to synthesizing the analogous polymer bound PAG that would be needed in the cationic system. This relative ease is one of the advantages of moving to a free radical based system because having the initiator be bound to a polymer backbone would not only allow initiator concentrations to range from near zero to 100%, as opposed to being restricted to the solubility limit of a physically dispersed initiator, but also would ensure

that the initiator remains much more evenly dispersed throughout the film. In a physically dispersed system, the initiator would be free to aggregate into clumps.

As a first pass, it was decided to combine a nitroxide-based thermal radical generator with styrene via a conventional radical polymerization, which could be carried out at a relatively low temperature so as to not activate the nitroxide towards polymerization. This polymer could then be heated to cleave the oxygen carbon bond and allow the incorporation of a monomer, M. This scheme is illustrated below in Figure 3.5. If successful, this scheme would demonstrate the feasibility of a living free radical polymerization as a platform for grafting, and future, more complicated platforms could be built off of this relatively simple system. Future efforts would include demonstrating grafting from the gas phase and the development of a light based switching group, which would allow the material to be photo-patterned.

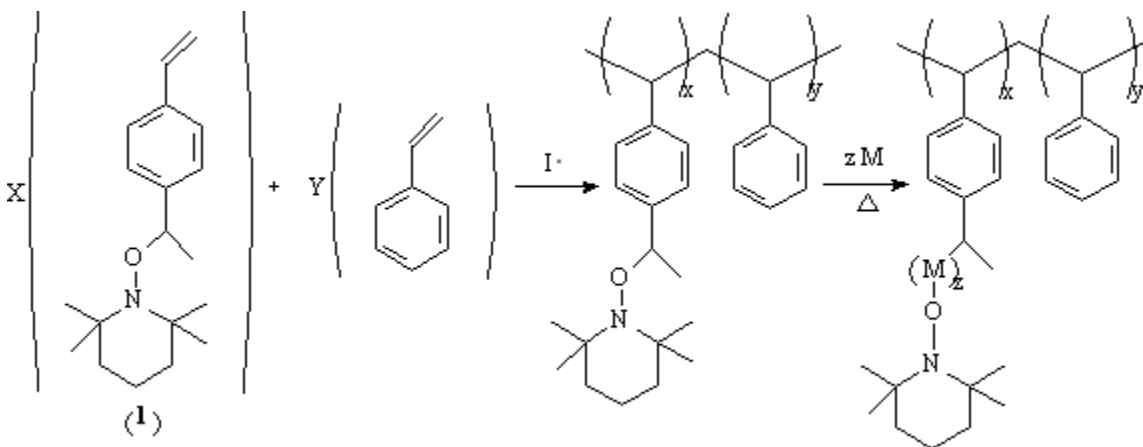


Figure 3.5 Proposed radical graft polymerization scheme

The first challenge associated with this goal was the synthesis of (1). Initial attempts to synthesize this compound were by the reaction of divinylbenzene with

TEMPO in the presence of a catalyst. This reaction scheme, based on the work of Hawker⁴⁴ and McAdams,⁵⁷ is shown in Figure 3.6 as follows:

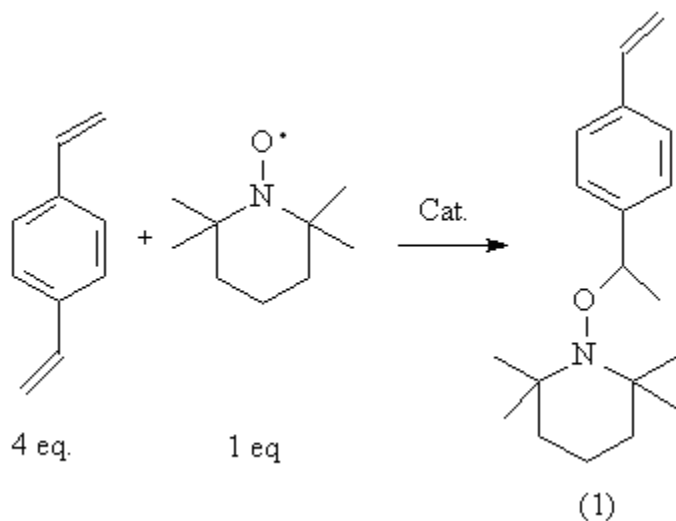


Figure 3.6 Proposed synthesis of living free radical initiator

This reaction was conducted several times and monitored by both thin layer chromatography (TLC) and nuclear magnetic resonance spectroscopy (NMR). Purification of the desired product was attempted by column chromatography, but success was never achieved. The difficulties in purification were attributed to the production of multiple products. The starting material was a mixture of both meta and para isomers, which led to both isomers of the product. Additionally, the di-TEMPO-substituted product could be formed as well. These products were detected with TLC and high pressure liquid chromatography (HPLC). It was ultimately decided to abandon this synthetic pathway because of the difficulty in separation as well as the fact that any di-substituted product impurity would cause cross-linking when polymerized along with the mono-substituted product. The second pathway that was chosen for investigation is shown in Figure 3.7 as follows:

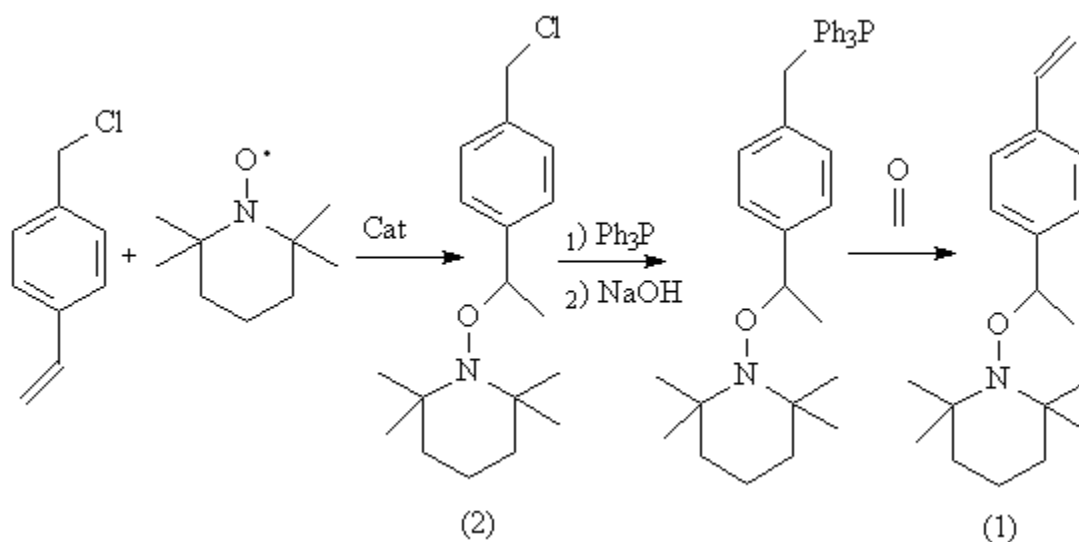


Figure 3.7 Alternate synthesis of living free radical initiator

This synthesis is an improvement because the starting material was available in pure para form, and there is no chance for the di-substituted product to be formed. The first step of the synthesis was performed successfully, but difficulty was encountered with the formation of the Wittig salt. The reaction was run in benzene, so the salt was expected to precipitate out. At room temperature, no precipitate was observed, so the reaction was heated. No precipitate was observed after several hours of stirring at 60°C. The reaction mixture was then refluxed at about 90°C for two days, but still no precipitate was observed. When analyzed by TLC, a large amount of the starting compound (2) was observed to be present even after 2 days of refluxing in benzene. Additional small spots were observed as well, some of which corresponded to the decomposition products of (2).

As a result, the Finkelstein reaction was attempted on (2) to convert the chloride to the more reactive iodide, which could then be used to form the Wittig salt. This reaction initially proceeded as expected with the formation of a precipitate; however, when left overnight, a red color developed. This red substance was observed to be

volatile and hence was theorized to be iodine, possibly produced by the presence of oxidizers or the light induced cleavage of the weak carbon iodine bond. This reaction could therefore be improved by running it under nitrogen, wrapping the reaction flask with foil to prevent light from entering, and not allowing the reaction to continue for as long.

At this point, because of difficulty with the Wittig reaction, a new idea emerged. It was thought that the esterification of compound (2) might go more smoothly than the Wittig reaction. Figure 3.8 below shows the proposed reaction scheme between (2) and a polymerizable carboxylic acid, (3), which was readily available in the lab for a different project. The esterification was performed based on the work of Ono *et. al.*⁵⁸

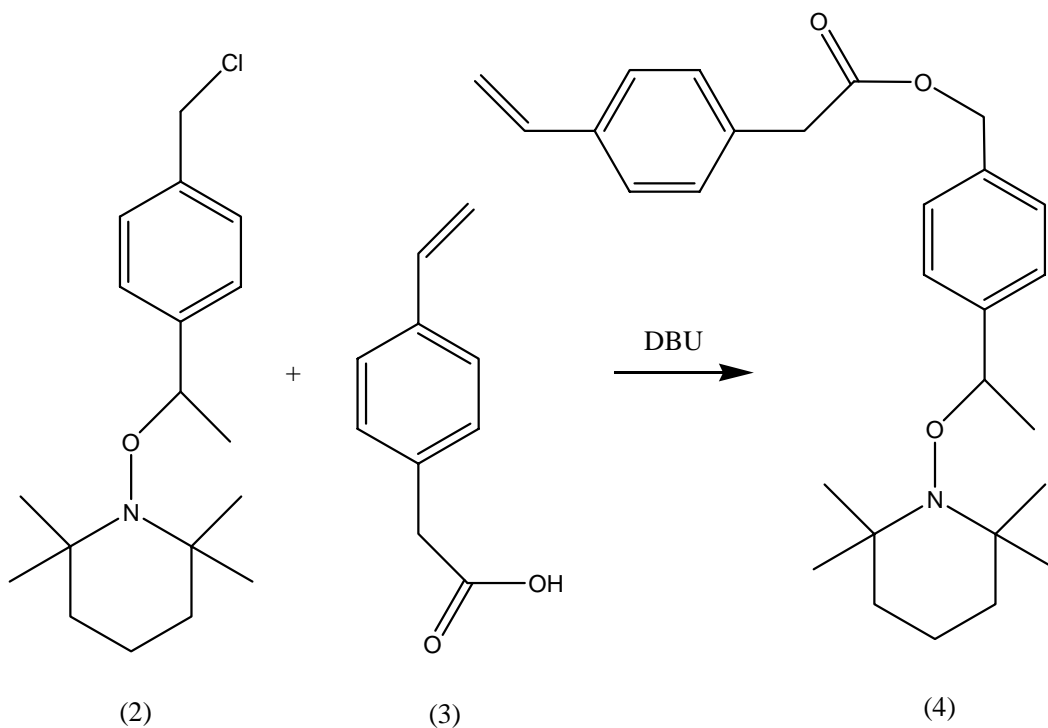


Figure 3.8 Proposed synthesis of an alternate living free radical initiator

The reaction shown in Figure 3.8 was successfully carried out, but thin layer chromatography showed many undesirable side products. The product was difficult to purify and the reaction was low yielding. As a result, the Finkelstein reaction was again used to convert the chloride to the iodide, and the above reaction was attempted again. This time, the reaction was more successful. The product of the reaction with the iodide was co-polymerized with styrene to yield the desired polymer-bound, nitroxide-based radical generator. Styrene was later grafted onto the polymer to verify the activity of the product. The entire process is shown in Figure 3.9 below.

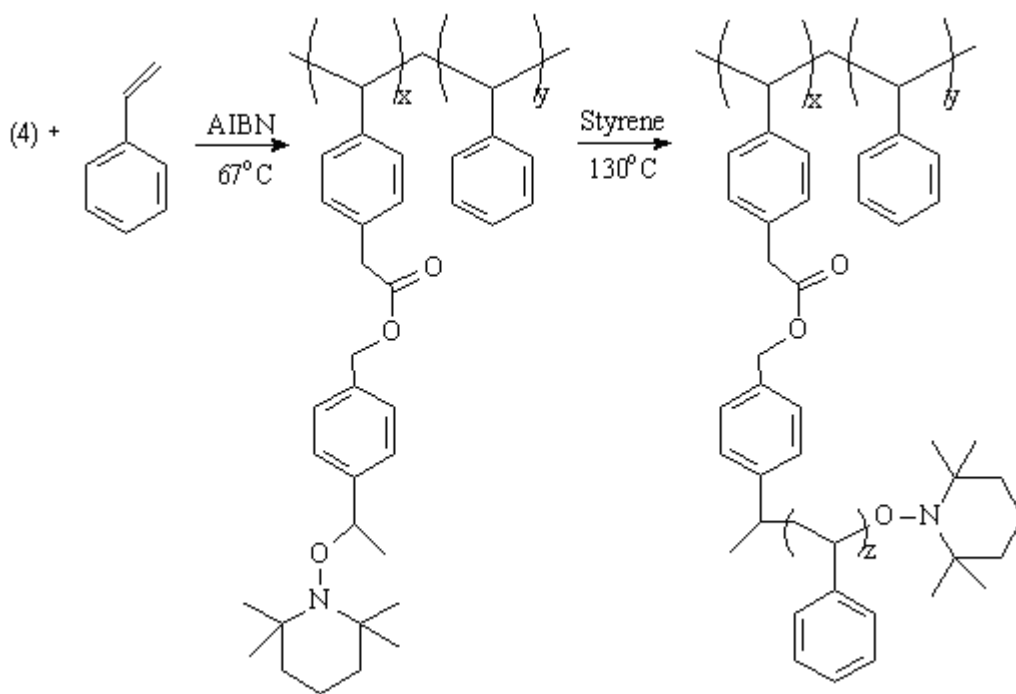


Figure 3.9 Synthesis of a polymer bound living free radical initiator and the use of that initiator to graft styrene onto the backbone

At this point, the basic proof of concept of a nitroxide based initiator for grafting had been demonstrated. The next step was to develop a photochemical switch that would allow a film of the polymer to be patterned. Efforts were expended to discover a suitable

functional group, but little success was realized. Meanwhile, simultaneous work with non-living systems showed great promise. Because of these reasons, work on the living system was halted and efforts were shifted to the more promising non-living route.

3.3 A NON-LIVING FREE RADICAL PROCESS

Despite the many advantages of developing a living free radical initiator suitable for graft polymerization lithography, difficulties in finding a suitable photochemical switching group rendered this route untenable. As a result, efforts were shifted to the development of a non-living system. Numerous commercially available thermal initiators and photo-initiators are available, but no commercial source of polymer bound radical initiator was found; hence, synthetic efforts to produce a polymer bound photo-radical generator were begun.

3.3.1 Initiator Synthesis

Rather than develop an entirely new chemistry, it was decided to base the polymer bound photo-radical generator on existing commercially available small molecule photo-radical generators. The Irgacure series of photo-radical generators (PRG) from Ciba Specialty Chemicals was chosen as a model for the polymer bound set of photo-radical generators. Specifically, Irgacure 2959 and Irgacure 184 were chosen as model compounds. The structures of these molecules are shown in Figure 3.10 below.

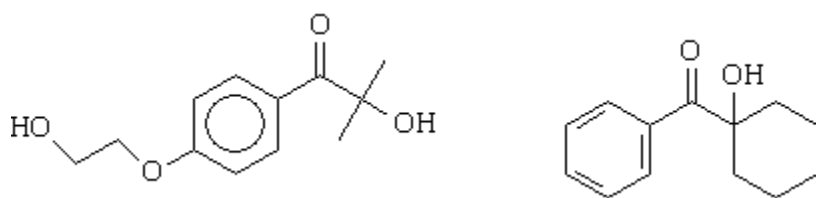


Figure 3.10 Irgacure 2959 (left) and Irgacure 184 (right)

Figure 3.11 illustrates the first attempt to make a polymerizable photo-radical generator.

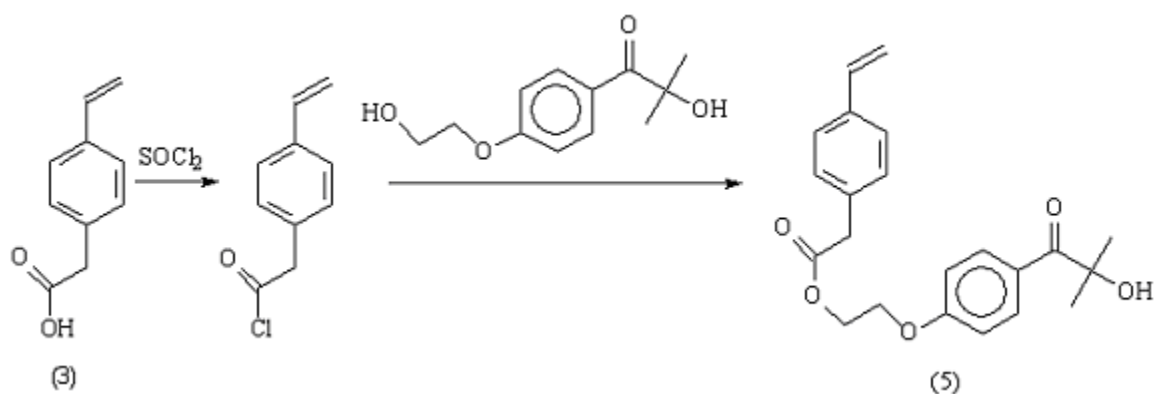


Figure 3.11 Proposed synthesis of a polymerizable photo-radical generator

This reaction was conducted, but NMR analysis showed a multitude of products including the product resulting from the addition of HCl across the double bond of the carboxylic acid. Purification was not attempted. To avoid the chlorination of the double bond, it was decided to first co-polymerize (3) with styrene, and then add SOCl_2 to form the acid chloride, followed by the addition of Irgacure 2959. This synthesis should have produced a copolymer of styrene and (5). Again, the results were unsatisfactory, and no purification was attempted. An alternate route was proposed as shown in Figure 3.12

below. This reaction was completed successfully, and the product was isolated and copolymerized with styrene to give the polymer-bound version of Irgacure 2959, PRG1.

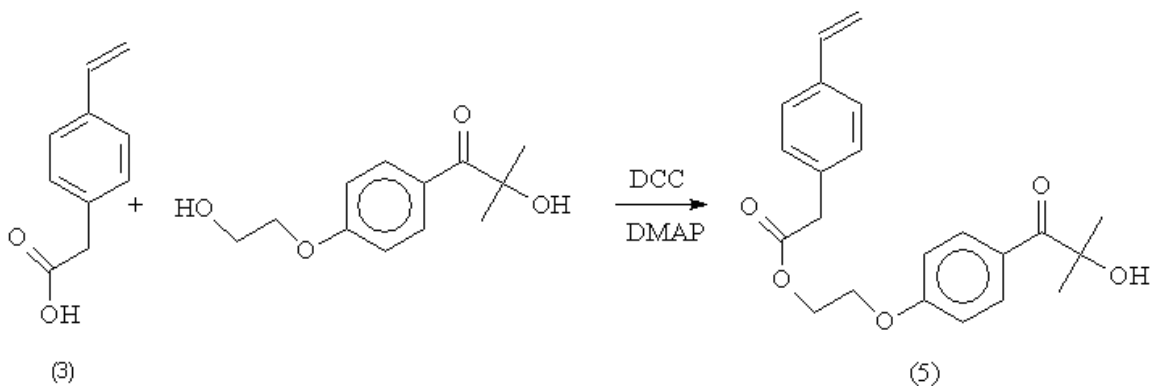


Figure 3.12 Alternate synthesis of a polymerizable photo-radical generator

Figure 3.13 below shows a synthesis that was proposed to make a second polymerizable photo-radical generator. This synthesis was based on the work of Ohta *et al.*⁵⁹

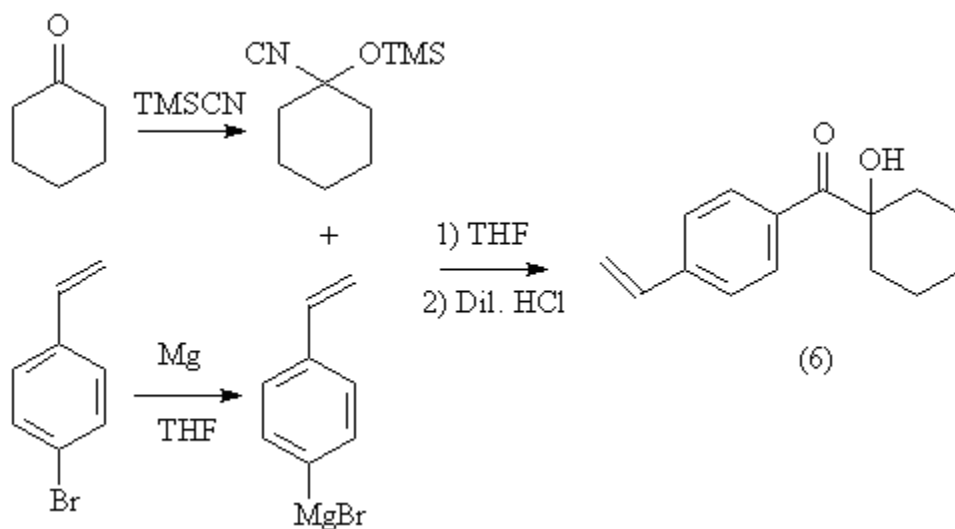


Figure 3.13 Proposed synthesis for a second polymerizable photo-radical generator

The synthesis of the TMS protected cyanohydrin was attempted twice. One attempt used butyl lithium as catalyst, and the other used zinc dibromide as a catalyst. Both attempts were successful, although the former was higher yielding. The synthesis of the Grignard reagent, however, proved to be extremely problematic. Several attempts were made, but none were successful. Eventually, this step was abandoned and instead, bromostyrene was reacted with butyl lithium in a metal/halogen exchange type reaction. The TMS protected cyanohydrin was then added to the lithium complex to form (6). This compound was then co-polymerized with styrene to form a second polymer-bound photo-radical generator, PRG2. This synthetic route is particularly useful, as it could be used to generate a wide range of different structures. The synthetic route used to create PRG1 is useful because it is a relatively simple synthesis, although it is limited to structures containing Irgacure 2959.

The first step in assessing the utility of these polymers was to determine if they actually produced radicals. To do this, four samples of hydroxyethylacrylate were made. In the first a small amount of PRG1 was added. The second contained PRG2, and the third contained Irgacure 2959. The fourth sample was left pure. Each of the samples was irradiated under UV light. The first three formed solid masses whereas the fourth remained liquid. From this experiment, it was concluded that both of the polymers generated free radicals on exposure to UV light.

These two polymers, PRG1 and PRG2, were found to have relatively low glass transition temperatures (T_g). It was postulated that higher glass transition temperature materials would be beneficial for top surface imaging. A higher T_g material would allow less diffusion of gas phase monomer into the film, which could lead to undesirable incorporation of silicon in the film through sorption. Also, materials with high T_g can be

heated to higher temperature without losing their shape, and hence should be better able to maintain the shape of grafted features.

Initial efforts focused on the copolymerization of (5) with a higher T_g comonomer, maleimide. These efforts were unsuccessful. Because of the expertise of the Willson group chemists with norbornene type materials, it was decided to develop a norbornene based system. The first synthetic step was to bind the PRG to a norbornene monomer. Figure 3.14 below shows the coupling reaction between Irgacure 2959 and norbornene carboxylic acid that was used to accomplish this task.

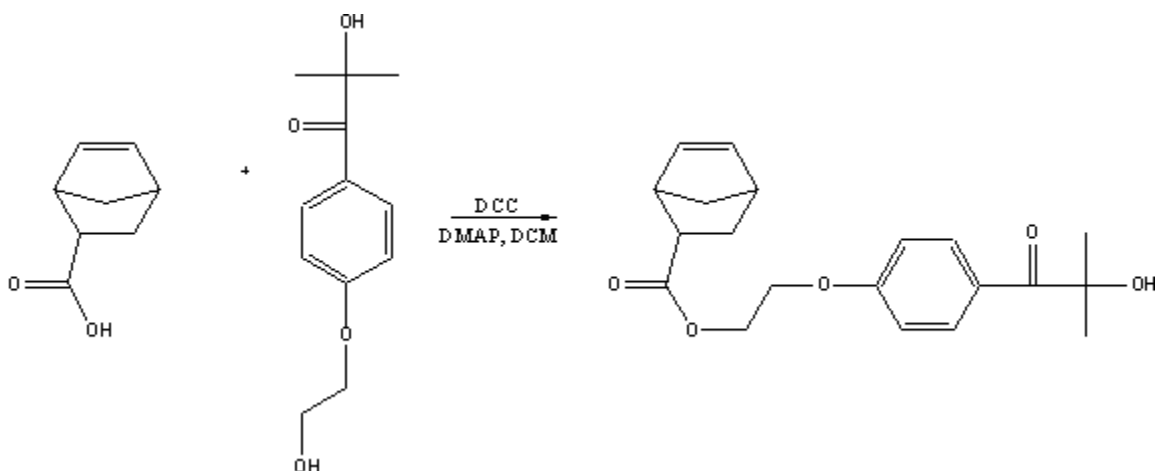


Figure 3.14 Synthesis of the norbornene-bound photo-radical generator

The synthesis of a copolymer containing this monomer was attempted. Maleic anhydride was used as a comonomer to raise the glass transition temperature of the resulting polymer. Figure 3.15 below shows this scheme. This synthesis resulted in extremely poor yield and, hence, was abandoned.

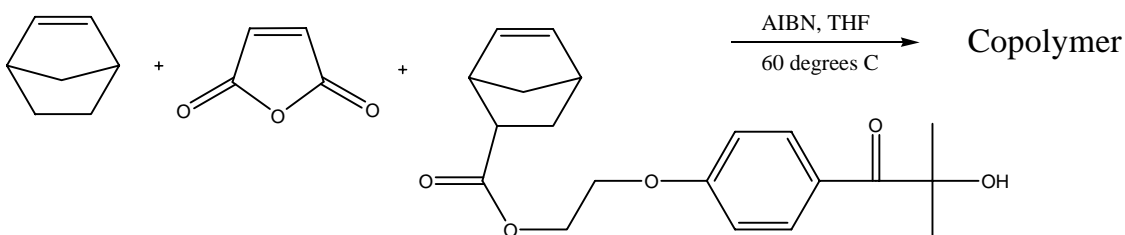


Figure 3.15 Attempted synthesis of a norbornene based, polymer bound PRG

It was thought that the above scheme failed because the norbornene moiety was unreactive towards polymerization. The proposed solution was to use a dinorbornene moiety in its place. Irgacure 2959 was bound to dinorbornene carboxylic acid in a synthesis similar to that shown in Figure 3.11. Figure 3.16 shows this scheme.

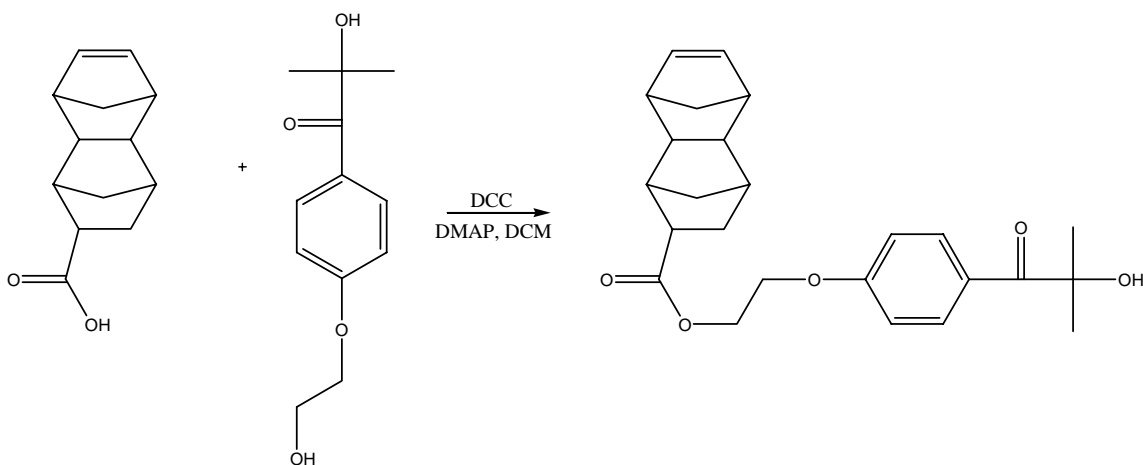


Figure 3.16 Synthesis of the dinorbornene-bound PRG

The copolymerization of this monomer with dinorbornene methyl ester was attempted with t-butyl peroxide as the solvent. The solubility of the monomer was very poor, and as a result, it was necessary to add butanol to the mixture to promote solubility. Precipitation into hexane resulted in a very low yield copolymer. Figure 3.17 shows this scheme.

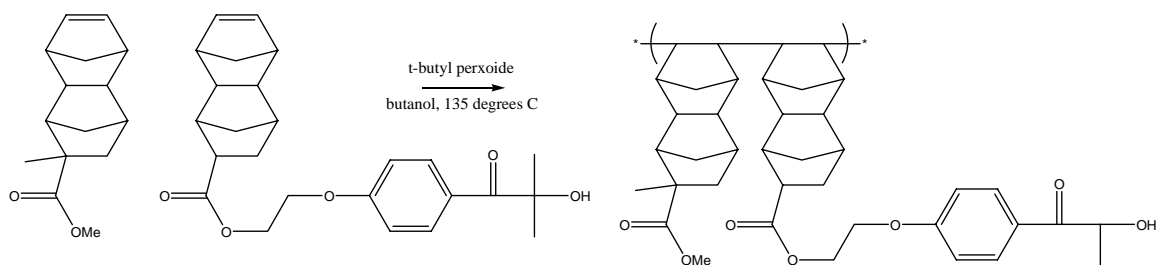


Figure 3.17 Attempted synthesis of a dinorbornene based, polymer-bound PRG

Synthesis of a similar copolymer was attempted with the use of a methyldinorbornene, which is more soluble in t-butyl peroxide. Again, very low yield was achieved. Figure 3.18 shows this scheme.

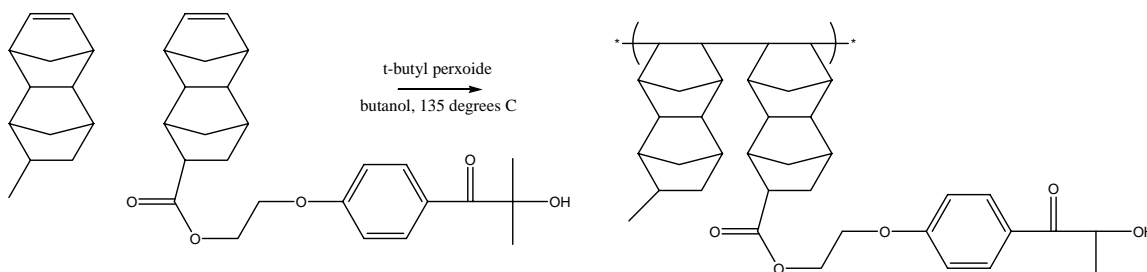


Figure 3.18 Second Attempted synthesis of a dinorbornene based, polymer-bound PRG

Radical polymerization was abandoned because of these discouraging results. It was decided to attempt to induce polymerization using a ring opening metathesis polymerization (ROMP) scheme to produce the copolymer. Figure 3.19 shows this scheme. This polymerization was successful in creating copolymer with a 15:85 mole ratio of PRG to comonomer.

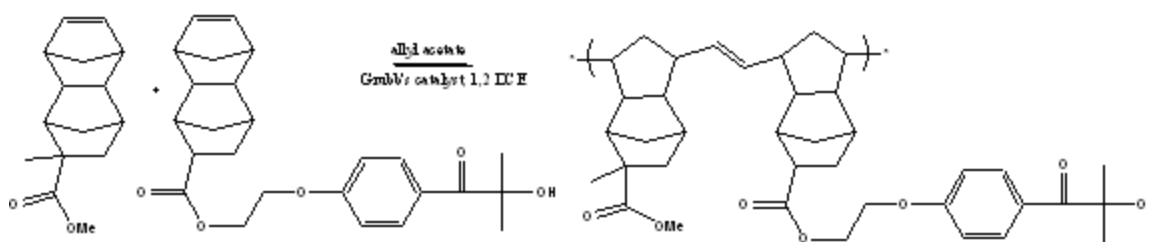


Figure 3.19 Successful synthesis of a dinorbornene based, polymer-bound PRG

3.3.2 Initiator Testing and Early Grafting Results

At this point, several polymer-bound PRGs had been synthesized and were available. The next step was to try to graft gas phase monomer onto a thin film of the polymer. For this simple proof of concept, an oxygen free grafting chamber was required. An oxygen free environment was required so as to not quench the radicals. Also required was a method for delivering gas phase monomer to the wafer. Finally, a UV transparent window was required so that UV light could enter the chamber to generate radicals.

As no chamber meeting these characteristics was available, a simple exposure chamber was constructed out of glass. Quartz was used at the top of the chamber for UV transparent windows. A nitrogen inlet was used to purge the chamber of oxygen. A well at the bottom of the chamber in which liquid monomer could be placed and heated with a water bath provided a source for gas phase monomer. This chamber is shown schematically in Figure 3.20 below.

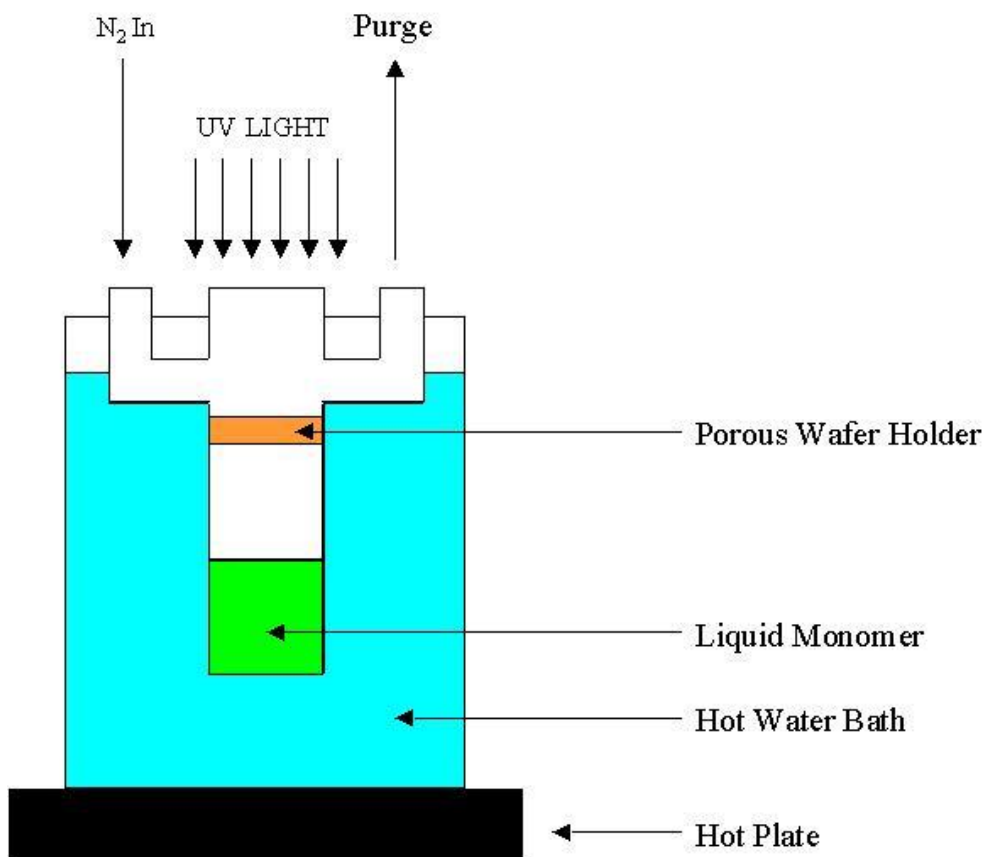


Figure 3.20 Simple exposure chamber schematic

The idea behind this chamber was that a wafer coated with a thin film containing a photo-radical generator could be placed on the wafer holder, and the bottom of the chamber could be filled with liquid monomer. The chamber could then be purged with nitrogen to displace the oxygen from the atmosphere inside the chamber. After removing the oxygen, the hot plate is able to heat the system thereby increasing the vapor pressure of the monomer at the bottom. This vapor should expand to fill the chamber and thereby come into contact with the wafer. UV light could then be shined through the quartz top of the apparatus and onto the wafer. Radicals would be generated where the light hit.

These radicals could then initiate a polymerization reaction with the gas phase monomer and thereby form a graft on the surface. This experiment was carried out with PRG1 as the radical generator and methyl acrylate (MA) as the monomer.

This experiment did result in the growth of grafted polymer and hence, was a successful proof of concept of grafting monomer onto a polymer surface from the gas phase. Unfortunately, the quality of the grafted film was very poor, probably because of the crudeness of the chamber. For example, MA volatilized from the reservoir at the bottom of the tube and condensed at the top of the apparatus where it was able to drip down onto the stage and splash on the wafer. Figure 3.21 shows a photograph of this film. It was readily apparent that polymer had grown, but because of the poor quality of this film, quantitative measurement of the growth was impossible. This experiment made clear the need for a better grafting chamber. Chapter 4 contains a description of further development of a grafting chamber as well as additional grafting results.

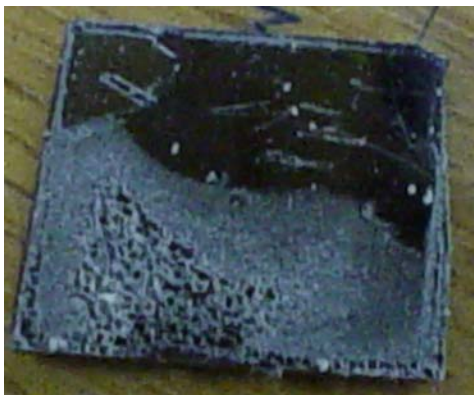


Figure 3.21 A photograph of the first “successful” radical graft of this project

3.3.3 Developing an Imaging Process

At this point, the first photo-radical graft from the gas phase had been made. The next step was to invent a way to form images by this technique. Obviously, it would be impractical to create an oxygen-free environment inside of a stepper in which grafting could be performed. To circumvent this difficulty, a light based “switch” is required such that the wafer could be imaged inside a stepper and then transferred to a secondary chamber in which the grafting could be done. Figure 3.22 below shows three such schemes. In the figure, blue represents area that is active towards graft polymerization, gray represents inactive area, and green represents the graft. The first scheme shows a light-deactivated thermal radical generator, and the second scheme shows a light-activated thermal radical generator. The final scheme shows a light-deactivated photo-radical generator. The deactivation in this case is caused by performing the patterning exposure in the presence of oxygen, where any radicals generated are quenched. When the wafer is then taken to the oxygen-free environment for grafting, only the unexposed areas remain active to grafting.

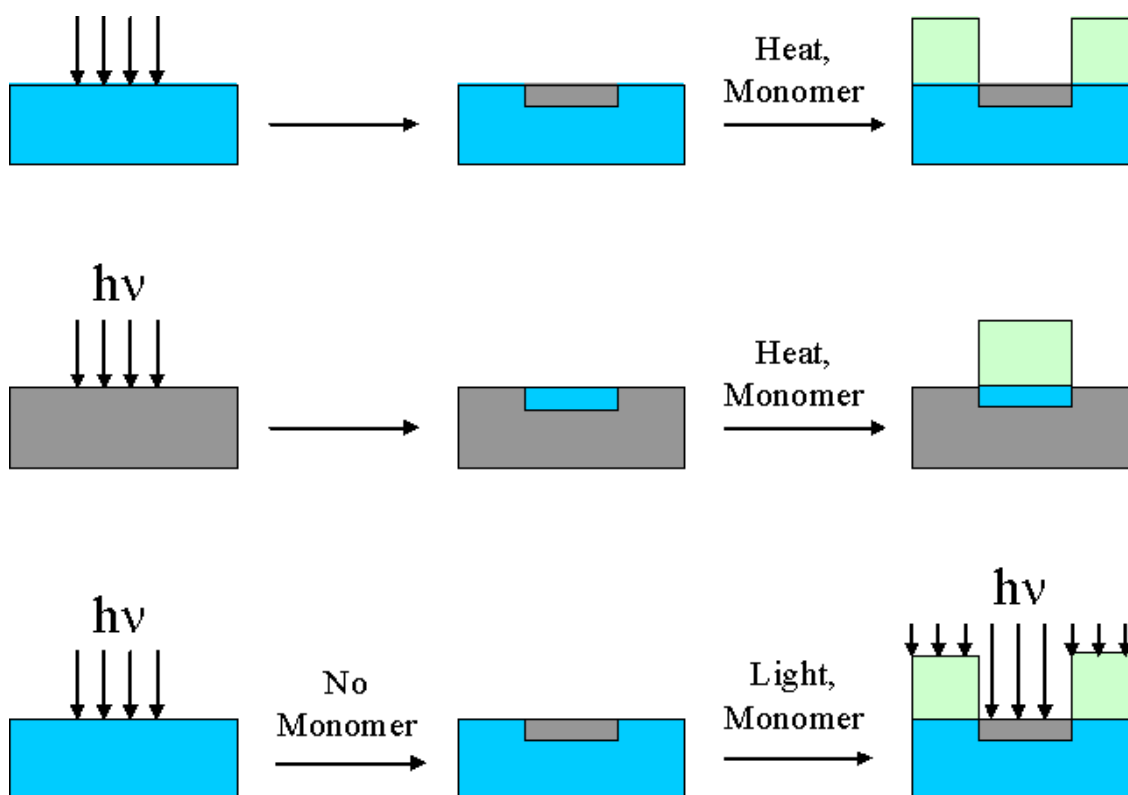


Figure 3.22 Three schemes for imaging using the radical grafting technique

The first two schemes rely on the development of a photochemical switch that either activates or deactivates the film towards thermal radical generation. This fact presents a serious disadvantage over the third scheme, which requires only the presence of oxygen as the switch. Furthermore, it was thought that light induced graft polymerization would occur faster than thermal growth, which is desirable from the perspective of industry. For these reasons it was decided that the third scheme would be pursued. The disadvantage of the third scheme is that it requires exposure to UV light during the grafting process.

3.4 SYNTHESIS OF GAS PHASE SILICON CONTAINING MONOMERS

Now that the process had been chosen and no further synthesis of the initiator group was required, the next step was to synthesize a silicon containing monomer that could be grafted onto the base layer. This material is designed to provide oxygen etch resistance for the grafted features, allowing pattern transfer to the underlying substrate. Studies have shown that ideally, the monomer should contain at least twelve to fifteen percent silicon content to achieve the required etch resistance.⁶⁰ The monomer, of course, must also be radically polymerizable and volatile. No commercially available compounds were found that met all three of these criteria, so two target monomers, shown in Figure 3.23 below, were chosen as synthetic targets.

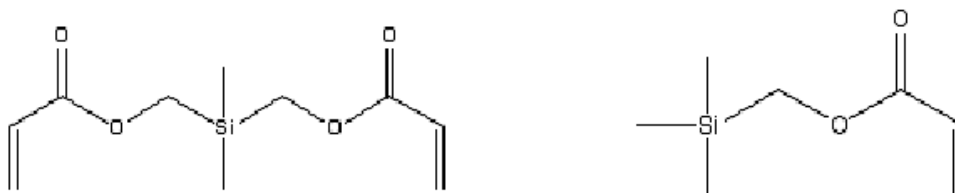


Figure 3.23 Target silicon containing monomers

The diacrylate is desirable because of its crosslinking ability. The monoacrylate is desirable because of its high vapor pressure. The synthetic scheme used to synthesize the diacrylate is shown in Figure 3.24 below. Column chromatography was used to purify the product, but impurities remained. Purification was completed by distillation.

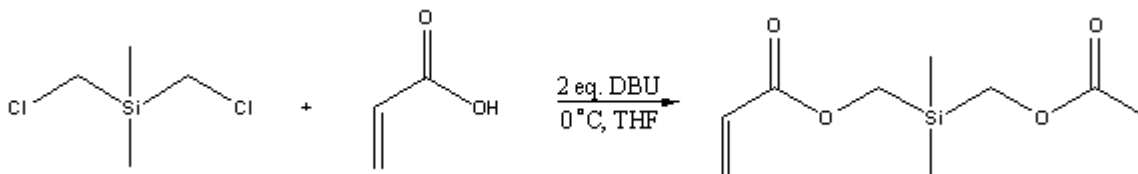


Figure 3.24 Synthesis of a difunctional, silicon containing monomer

Figure 3.25 shows a similar reaction scheme that was used to synthesize the monofunctional acrylate. An NMR spectrum was taken of the unpurified product of this reaction, and it was determined that the desired product comprised 43 percent of the crude. Distillation of the mixture was attempted, but the mixture polymerized, resulting in no yield. Repeated attempts at this synthesis were also unfruitful despite the addition of radical inhibitors.

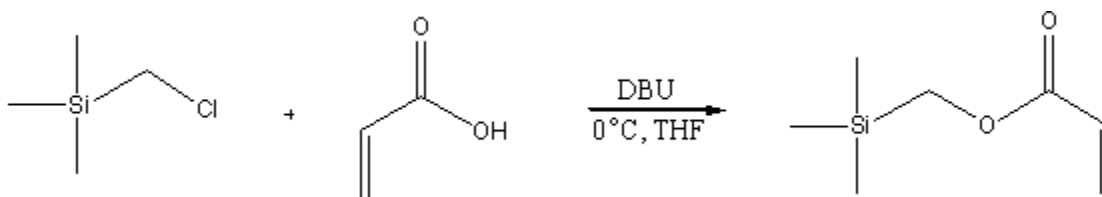


Figure 3.25 Attempted synthesis of a monofunctional, silicon containing monomer

An alternate synthesis of this compound was attempted. Figure 3.26 shows this scheme.

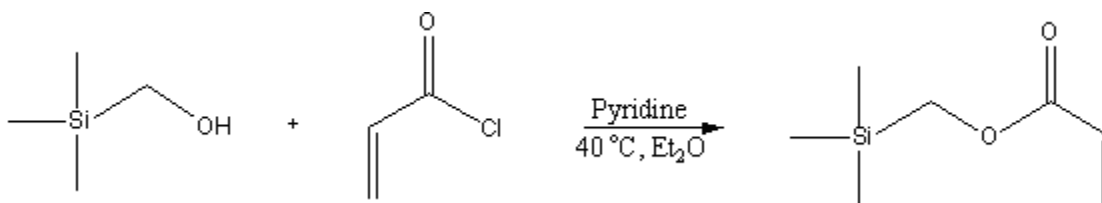


Figure 3.26 Second attempted synthesis of a monofunctional, silicon containing monomer

As in the previous synthesis, NMR indicated that product had been formed, but polymerization occurred upon attempted purification. The difference between the attempted synthesis of the monofunctional monomer and the successful synthesis of the difunctional monomer was the use of column chromatography before distillation. When column chromatography was used on the monofunctional product before distillation and

radical inhibitors were used during the distillation, successful synthesis of the monofunctional monomer was achieved.

3.5 CONCLUSIONS

This chapter describes the evolution of the free radical graft polymerization project from its inception to the first successful graft. Syntheses of both the base layer material and the silicon containing monomer were described. The process by which these materials could be used to generate an imaged wafer was also described. Chapter 4 will outline the remainder of this project including the development of a grafting chamber, grafting kinetics, and imaging results.

3.6 EXPERIMENTAL

3.6.1 Living Free Radical Generator Synthesis

Representative attempt to synthesize (1)

Into a 100 mL round bottom flask was placed 10 mL of a 1:1 mixture of toluene and ethanol. To the flask was added divinylbenzene (1.598 g), TEMPO (0.465 g), [N,N'-bis(3,5-di-tert-butylsalicylidene-1,2 cyclohexanediaminato) manganese(III) chloride, or Jacobsen's catalyst (0.438 g), tertiary butyl peroxide, or TBPO (0.448 g), and sodium borohydride (0.276 g). An additional 15 mL of 1:1 toluene:ethanol was then added to the mixture. The mixture was allowed to stir overnight after which time 5 mL of 50% acetic acid, 50 mL of diethyl ether, and 150 mL of water were added to the flask. The organic layer was separated and washed with 100 mL each of 5% acetic acid, 3% potassium carbonate, and saturated sodium chloride solution. The resulting organic layer was dried over anhydrous magnesium sulfate, and the solvent was removed by rotary evaporation.

The mixture was then purified by flash chromatography with a mixture of 49:1 hexanes to ethyl acetate to yield 0.364 grams of viscous brown oil. TLC and HNMR analysis indicated an impure product.

Synthesis of (2)

Into a 500 mL round bottom flask was placed 200 mL of a 1:1 mixture of toluene and ethanol. To the flask was added p-chloromethylstyrene (2.996 g), TEMPO (3.070 g), Jacobsen's catalyst (1.858 g), TBPO (2.890 g), and sodium borohydride (1.489 g). An additional 20 mL of 1:1 toluene:ethanol was then added to the mixture. The mixture was allowed to stir for 16 hours after which time 30 mL of 50% acetic acid, 200 mL of diethyl ether, and 400 mL of water were added to the flask. The organic layer was separated and washed with 500 mL each of 5% acetic acid, 3% potassium carbonate, and saturated sodium chloride solution. The resulting organic layer was dried over anhydrous magnesium sulfate, and the solvent was removed by rotary evaporation. The mixture was then purified by flash chromatography with a mixture of 20:1 hexanes to ethyl acetate. 4.904 grams (81% yield) of a viscous brown oil was isolated. On standing overnight, this oil turned green in color and eventually crystallized to form a dark green solid. TLC and HPLC as well as the green color indicated the presence of a colored impurity. The crystals were triturated twice in ethanol to remove the impurity. The result was the formation of a white powder in 32 percent yield. M.P 62-64°C; Yield 26%; ¹HNMR (CDCl₃) δ 0.580, 0.939, 1.076, 1.200 (each br s, 12H, CH₃), 1.166-1.402 (m, 6H, CH₂), 1.377 (d, 3H, CH₃), 4.467 (s, 2H, CH₂), 4.702 (q, 1H, CH), 7.187-7.250 (m, 4H, ArH); ¹³CNMR (CDCl₃) δ 17.011, 20.143, 23.362, 24.017, 34.279, 40.134, 46.004, 59.463, 82.528, 126.669, 127.958, 135.663, 145.903; mass spectrum (CI) m/z 310/312 (3:1); high resolution mass spectrum/elemental analysis (CI) m/z 310.193899 C₁₈H₂₉NOCl.

Attempted Formation of the Wittig Salt

Into a 50 mL round bottom flask was added 0.519 grams of (1) dissolved in 10mL of benzene and 0.421 grams of triphenylphosphine dissolved in 10 mL of benzene. This mixture was allowed to stir for 4 hours at room temperature. No precipitate was observed, so the mixture was slowly heated to reflux. The mixture was allowed to reflux for two days, but no precipitate formed. TLC analysis of the reaction mixture indicated a high concentration of starting material remaining along with products that were most likely formed from the decomposition of (1). Two new spots were observed, but they were quite small and difficult to detect. These results indicate a low conversion of starting material to the desired product.

Finkelstein Reaction

Into a 25 mL round bottom flask were added 0.516 grams of (1) and 0.291 grams of sodium iodide. These compounds were dissolved in approximately 10 mL of acetone. Upon stirring, the solution became cloudy and the formation of a precipitate was observed. The reaction was allowed to continue overnight, and in the morning, a red color was observed. The removal of the solvent by rotary evaporation was performed. It was observed that some of the compound that provided the red color was carried over along with the solvent leaving behind a red oil. TLC analysis indicates that a large amount of unreacted starting material was present in the oil along with other compounds.

Synthesis of (4)

Into a 25 mL round bottom flask were added 0.1989 grams of (1) and 0.1077 grams of sodium iodide. These compounds were dissolved in approximately 10 mL of

acetone. Upon stirring, the solution became cloudy and the formation of a precipitate was observed. The reaction was covered tightly in aluminum foil to block entering light and continued overnight. In the morning, a yellow color had developed. The solid precipitate was filtered out, and the solvent was removed by rotary evaporation. The yellow crystals were redissolved in benzene and refiltered to remove additional precipitate. NMR analysis showed 80% conversion to the iodide. Without further purification, the product of this reaction was dissolved in 5mL of benzene and placed in a 25 mL round bottom flask. In a separate flask, 0.104 grams of (2) and 0.105 grams of DBU were dissolved in 5mL of benzene. The second solution was added to the first. A cloudy precipitate and slightly yellow color was observed. The reaction was stirred overnight. The mixture was washed with water, dried over anhydrous sodium sulfate, and purified by flash chromatography using 6:1 hexanes:ethyl acetate. White crystals were isolated (0.1843 g, 65% yield). ¹HNMR (CDCl₃) δ 0.657, 1.022, 1.159, 1.283 (each br s, 12H, CH₃), 1.367-1.471 (m, 6H, CH₂), 1.449 (d, 3H, CH₃), 3.637 (s, 2H, CH₂), 4.780 (q, 1H, CH), 5.102 (s, 2H, CH₂), 5.215, 5.715 (each d, 2H, CH₂=), 6.682 (q, 1H, CH=), 7.213-7.360 (m, 8H, ArH);

Polymerization of (4)

Into a 100mL, three necked, round bottom flask was placed 0.2112 grams of (3), 0.5050 grams of styrene, 0.0876 grams of AIBN, and 11mL of THF. The flask was placed in a hot oil bath at 70°C and refluxed overnight under nitrogen. The solvent was removed by rotary evaporation, and the polymer was purified with two precipitations in hexane yielding 0.0824 grams of a white solid (yield=12%). The resulting polymer was determined by NMR analysis to contain a ratio of styrene:(3) of 9:1. ¹HNMR (CDCl₃) δ 7.2 (b), 6.6 (b), 5.1 (b), 4.9 (b), 3.6 (b), 1.8 (b), 1.5 (b), 1.2 (b), 0.8 (b). GPC: M_n=3,050,

$M_w=5,050$, $Pd=1.656$, relative to polystyrene. DSC: $T_g=67.5^\circ\text{C}$. To 0.0492 grams of this polymer in a 25mL round bottom flask was added 1.04 grams of styrene. This mixture was heated under a nitrogen bath to 135°C overnight. The resulting polymer was purified by precipitation into hexane yielding 0.4741 grams of polymer (yield=44%). $^1\text{HNMR}$ (CDCl_3) δ 7. (b), 6.5 (b), 1.8 (b), 1.4 (b), 0.8 (b). GPC: $M_n=11,700$, $M_w=53,200$, $Pd=4.547$, relative to polystyrene. DSC: $T_g=98^\circ\text{C}$.

3.6.2 Non-Living Free Radical Generator Synthesis

Synthesis of (5)

To a 100 mL round bottom flask were added 1.5908 grams Irgacure 2959, 1.0004 grams of (4), and a catalytic amount of DMAP. This mixture was dissolved in 40 mL of DCM. The flask was placed in a dry ice/acetone bath and cooled to -20°C at which time 7 mL of a 1M solution of DCC in DCM was slowly added. The mixture was warmed slowly to room temperature as the reaction mixture was stirred overnight. Three drops of acetic acid were added to the reaction mixture, and it was stirred for an additional 30 minutes. The mixture was filtered, and the solvent was removed by rotary evaporation. The mixture was redissolved in ethyl acetate and filtered again. The solvent was removed by rotary evaporation, and the resulting yellow oil was purified by column chromatography with 1:1 hexanes:ethyl acetate to give 2.0760 grams of white crystals (yield=91%). $^1\text{HNMR}$ (CDCl_3) δ 1.607 (s, 6H, CH_3), 3.633 (s, 2H, CH_2), 4.208 (t, 2H, CH_2), 4.455 (t, 2H, CH_2), 5.211, 5.695 (each d, 2H, $\text{CH}_2=$), 6.662 (q, 1H, CH=), 6.888-6.917 (m, 2H, ArH), 7.199-7.337 (m, 4H, ArH), 8.016-8.058 (m, 2H, ArH); mass spectrum (CI^+) m/z 369; (CI^-) m/z 367.

Synthesis of 1,1-Cyanotrimethylsiloxycyclohexane

Cyclohexanone (3.961 grams) was dissolved in 85 mL of dry THF. The flask was placed in an ice bath and to it was added 7mL of trimethylsilylcyanide followed by 0.25 mL of 2.5M butyl lithium solution in hexanes. The solution was removed from the ice bath and stirred for 4 hours. To the flask was then added 85 mL of water. The solution was extracted with diethyl ether 3x85mL and dried over anhydrous sodium sulfate. The ether was removed by rotary evaporation, and the resulting liquid was distilled under vacuum ($T_{\text{base}}=110^{\circ}\text{C}$, $T_{\text{top}}=65\text{-}72^{\circ}\text{C}$, $P=200$ mTorr) to yield 7.965 grams of a clear liquid (yield=88.9%). $^1\text{HNMR}$ (CDCl_3) δ 0-0.4 (m, 9H, CH_3), 1.1-2.2 (m, 10H, CH_2); mass spectrum (CI+) m/z 171.

Synthesis of (6)

Bromostyrene (2.5023 g) and THF (25mL) were placed in a 100 mL three necked flask under a nitrogen atmosphere. The flask was cooled to -78°C , and 6 mL of a 2.5M solution of butyl lithium in hexanes was added dropwise. The solution was stirred for one hour before 3.5795 grams of 1,1-cyanotrimethylsiloxycyclohexane was added. The reaction was stirred overnight after which time 50 mL of water was added to quench the reaction. The solution was washed with 50 mL water and the 50 mL brine. The organic layer was collected and dried over anhydrous sodium sulfate, and the solvent was removed by rotary evaporation. THF (25mL) was added along with 5 mL of 10% HCl. This solution was stirred for 2 hours. Finally, the solution was extracted with 3x50mL of ethyl acetate. The organic layer was dried and the solvent was removed. The resulting oil was purified by column chromatography with 5:1 hexane:ethyl acetate. The resulting white crystals (1.2964 grams) were obtained in 41% yield. $^1\text{HNMR}$ (CDCl_3) δ 1.314-

2.086 (m, 10H, CH₂), 3.400 (b, 1H, OH), 5.380, 5.855 (each d, 2H, CH₂=), 6.732 (q, 1H, CH=), 7.448 (d, 2H, ArH), 8.002 (d, 2H, ArH); mass spectrum (CI+) m/z 231.

Polymerization of (5)

Into a 100mL, three necked, round bottom flask was placed 1.5391 grams of (5), 1.0669 grams of styrene, 0.2360 grams of AIBN, and 30.2 mL of THF. The flask was placed in a hot oil bath at 70°C and refluxed overnight under nitrogen. The solvent was removed by rotary evaporation, and the polymer was purified by two precipitations into cold hexane, yielding 1.755 grams (yield=67%) of a white solid. The resulting polymer was determined by NMR analysis to contain a ratio of styrene:(5) of 7:3. ¹HNMR (CDCl₃) δ 8.1 (b), 7.1 (b), 6.5 (b), 4.4 (b), 4.2 (b), 3.7 (b), 3.5 (b), 0.8-2.2 (m,b); GPC: M_n=2,240, M_w=5,600, P_d=2.500, relative to styrene; DSC: T_g=44°C.

Polymerization of (6)

Into a 100mL, three necked, round bottom flask was placed 0.401 grams of (6), 1.6424 grams of styrene, 0.2890 grams of AIBN, and 35.15 mL of THF. The flask was placed in a hot oil bath at 70°C and refluxed overnight under nitrogen. The solvent was removed by rotary evaporation, and the polymer was purified by precipitation into cold hexane, yielding 0.5483 grams of a white solid (yield=27%). ¹HNMR (CDCl₃) δ 7.8 (b), 6.9 (b), 6.5 (b), 5.3 (b), 4.1 (b), 0.8-2.2 (m,b);

Norbornene Based PRG

A three necked round bottom flask (150 mL) was fitted with an addition funnel. One of the other necks was fitted with a nitrogen inlet and the last neck was fitted with a

rubber stopper. Into the round bottom flask was added Irgacure 2959 (5.83 g, 26.0 mmol), norbornene carboxylic acid (4 g, 29.2 mmol), dichloromethane (DCM) (50 mL), and a catalytic amount of 4-dimethylaminopyridine (DMAP). Once a nitrogen flow had been established, the reaction mixture was cooled to -20 °C. The addition funnel was loaded with a 1 molar solution of 1,3-dicyclohexylcarbodiimide (DCC) (28.6 mmol) in DCM (28.6 mL). The DCC solution was added dropwise to the reaction mixture. The reaction was cooled to room temperature overnight. The reaction mixture was filtered, the solvent was removed by rotary evaporation, and the product was redissolved in ethyl acetate (EtOAc). The product was purified with column chromatography using a 1:1 EtOAc:Hexane mixture. The resulting white solid was recovered in a yield of 45%. ¹H NMR (CDCl₃) δ 1.226 (m, 6H), 2.887 (s, 1H), 3.117 (t, 1H), 3.965 (q, 2H), 4.102 (m, 2H), 4.280 (s, 1H), 5.887 (s, 1H), 6.119 (s, 1H), 6.868 (d, 2H), 7.999 (d, 2H).

Dinorbornene Based PRG

A three necked round bottom flask (150 mL) was fitted with an addition funnel. One of the other necks was fitted with a nitrogen inlet, and the last neck was fitted with a rubber stopper. Into the round bottom flask was added Irgacure 2959 (5.83 g, 26.0 mmol), dinorbornene carboxylic acid (5 g, 26.0 mmol), dichloromethane (DCM) (50 mL), and a catalytic amount of 4-Dimethylaminopyridine (DMAP). Once a nitrogen flow had been established, the reaction mixture was cooled to -20 °C. The addition funnel was loaded with a 1 molar solution of 1,3- dicyclohexylcarbodiimide (DCC) (28.6 mmol) in DCM (28.6 mL). The DCC was added dropwise to the reaction mixture. The reaction was cooled to room temperature overnight. The reaction mixture was filtered, the solvent was removed by rotary evaporation, and the product was redissolved in ethyl acetate (EtOAc). The product was purified with column chromatography using a 1:1

EtOAc:Hexane mixture. The resulting white solid was recovered in a yield of 55% ^1H NMR (CDCl_3) δ 1.426 (m, 6H), 2.834 (s, 2H), 4.052 (q, 2H), 4.378 (t, 2H), 4.678 (t, 1H), 5.931 (s, 2H), 7.021 (d, 2H), 8.261 (d, 2H).

ROMP Copolymer

A three necked round bottom flask (150 mL) was fitted with a condenser. One of the other necks was fitted with a nitrogen inlet, and the last neck was fitted with a rubber septum. The dinorbornene based PRG (1 g, 2.5 mmol), dinorbornene methylester (3.34 g, 14.4 mmol), and 1,2 dichloroethane (62 mL) were added to the flask. Allyl acetate (0.169 g, 1.7 mmol) and Grubb's catalyst (0.0048 g, 0.005 mmol) were then added. The reaction was purified over a three-day period with a dialysis bag in DCM. The solvent was changed twice over the three-day period. The solvent was removed by rotary evaporation yielding a pink solid (68% yield). ^1H NMR (CDCl_3) δ 1.24 1.627 1.737 2.014 2.281 2.272 2.965 3.6544.312 5.450 6.950 8.056. M_n = 14,500, M_w = 39,000, PDI =2.7, relative to polystyrene.

3.6.3 Synthesis of Silicon Containing Monomers

Acrylic acid (acryloyloxymethyl-dimethyl-silanyl)-methyl ester

A three necked round bottom flask (150 mL) was fitted with an addition funnel. One of the other necks was fitted with a thermometer, and the last neck was fitted with a nitrogen inlet. Into the round bottom flask was added acrylic acid (2.9 g, 40.1 mmol) and THF (50 mL). The addition funnel was loaded with 1,8-Diazabicyclo[5.4.0]undec-7-ene (DBU) (6.1 g, 40.1 mmol) and THF (20 mL). The system was allowed to purge under nitrogen. The round bottom flask was cooled to 0 °C, and the temperature was

monitored with the internal thermometer. The DBU was then added dropwise into the round bottom flask. The solution was allowed to stir for 5 minutes. The addition funnel was then loaded with bis(chloromethyl)dimethylsilane (3 g, 19.1 mmol) and THF (10 mL). The system was purged for 5 minutes and then the silane was added dropwise. Column Chromatography was investigated because of potential problems in separating monoacrylated product from diacrylated product. A TLC revealed two broadly separated dots. Flash chromatography was used to isolate the bottom dot. The ^1H -NMR showed the product remained dirty, and upon further investigation it was determined that the remaining impurity did not appear on TLC. The product was fractionally distilled with added radical inhibitor at 300mTorr and 97 °C. The fraction was a clear colorless liquid with a 56% yield (3.3 g). GPC revealed a single peak at a retention time of 7.022 minutes. ^1H NMR (CDCl_3) δ .187 (m, 6H), 3.928 (s, 4H), 5.796 (d, 2H), 6.101 (q, 2H), 6.378 (d, 2H).

Chapter 4: Grafting Results and Conclusions

4.1 INTRODUCTION

At this point, efforts with the temporary chamber were abandoned in favor of a new ellipsometry chamber, which had just been built. It was put together by another student in the group, Andrew Jamieson. The new chamber allows in situ monitoring of the growth process and increased control over the processing conditions. It is a small temperature and pressure controlled chamber with a window on top, through which UV exposure can be performed, and it has windows on either side through which an ellipsometer can collect data. The interior of this chamber is large enough to accommodate a 2" silicon wafer. Additional detail about the design and construction of this chamber can be found elsewhere.²⁸ This chamber is schematically shown in Figure 4.1 below.

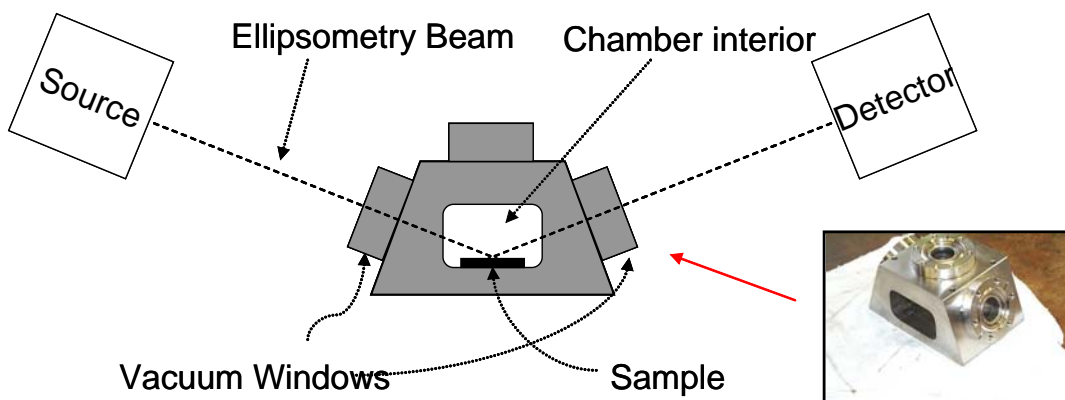


Figure 4.1 Schematic of the improved grafting chamber

4.2 EARLY INVESTIGATION OF THE GRAFTING PROCESS

Now that a tool suitable for easily grafting polymer onto a wafer had been developed, a few basic experiments were performed to better understand the process. First, a comparison of polymer bound grafting versus non polymer bound grafting was undertaken. The control experiment of grafting a wafer simply coated with polystyrene without any type of PRG was performed as well. The first wafer grafted contained Irgacure 2959 dispersed in polystyrene. The second wafer contained PRG1, the polymer bound PRG based on Irgacure 2959 chemically bonded to polystyrene. Both wafers contained approximately the same loading of photoinitiator, ten mole percent. These two PRGs are shown in Figure 4.2 below. A third wafer was coated with polystyrene containing no PRG at all.

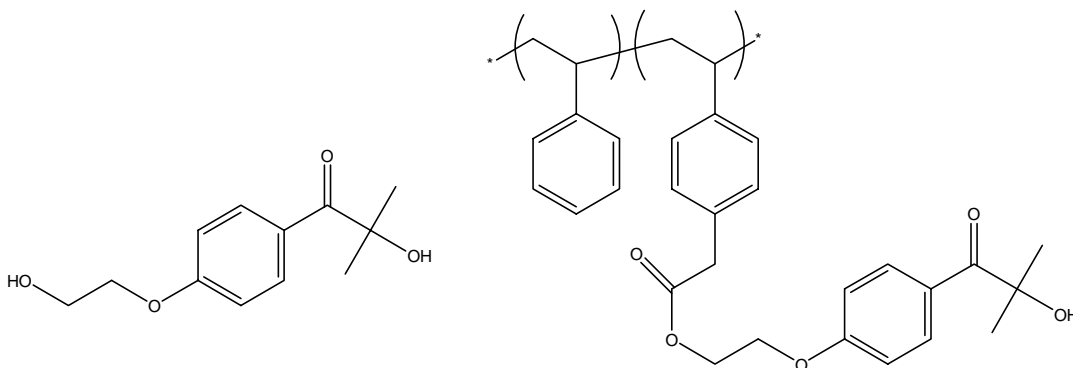


Figure 4.2 Small molecule PRG (left) and Polymer-bound PRG (right)

Polymer was spin coated onto the silicon wafer from a 20 percent solution of PGMEA. The spin coater was set to 2000 revolutions per minute for a time of 30 seconds. This procedure was followed by a 90 second post apply bake at 90°C. The wafer was then placed in the temperature and pressure controlled chamber in which the experiment was to be conducted. The chamber had previously been heated to 60°C. The

chamber was evacuated and refilled with nitrogen three times to ensure that all of the oxygen had been removed. The nitrogen filled chamber was then re-evacuated and allowed to stand for 5 minutes to come to thermal equilibrium. At this point data collection via the ellipsometer began. The chamber was then flooded with 42.5 torr of methyl acrylate. After a short time for equilibration, a Novacure UV curing tool was used to expose the wafer to filtered 248nm light at an intensity setting of 1000 mW. The light intensity inside the chamber at the wafer plane after passing through the light guide, filter, and quartz window was estimated to be approximately 0.1 mW/cm^2 . This number was estimated by shining the light through a quartz plate and 248nm band pass filter and into a light intensity meter outside of the chamber. This was done because a light intensity meter small enough to fit inside the wafer chamber was not available. Upon exposure to this light, a thickness change was observed on the ellipsometer. When the light was turned off, the growth stopped after a short time. When the light was turned back on, growth resumed. The experiment was then concluded by turning off the lamp and evacuating the chamber. Data from the ellipsometer is shown below in Figure 4.3.

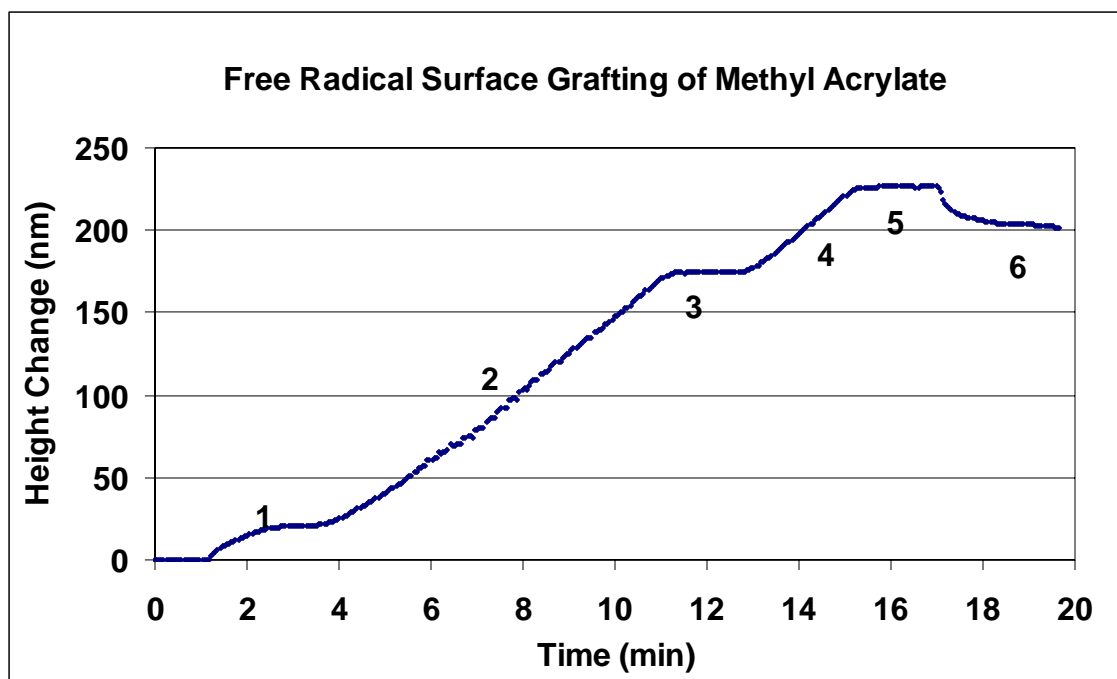


Figure 4.3 Free radical surface grafting of methyl acrylate onto a substrate of polymer bound photo-radical generator coated on silicon. The grafting was done at a temperature of 60°C and a monomer pressure of 42.5 torr. From left to right can be seen: 1) Swelling caused by sorption into the film as the monomer is introduced, 2) Growth as the wafer is exposed to UV light, 3) Cessation of growth as the lamp is turned off, 4) Resumption of growth when the light is turned back on 5) Cessation of growth as the lamp is once again turned off, and 6) Film shrinkage as the monomer is desorbed when the chamber is evacuated.

The next experiment was a repeat of the same experimental conditions, but this time using the non-bound version of the PRG. From observing the ellipsometer data during the course of the experiment, it became clear that something was different. Shortly after the light was turned on, the intensity of the reflected beam began to diminish, and the noise in the experimental data sharply increased. As a result, the ellipsometer data was unusable. When the wafer was removed from the chamber, visual inspection revealed a very rough, non-reflective surface. A photograph of this wafer

fragment is shown in Figure 4.4 below. A scanning electron microscope (SEM) was used to inspect this wafer, and isolated blobs of grafted material were seen rather than a continuous film as was desired. Based on this result, it was theorized that the unbound PRG dispersed in the polystyrene matrix was forming aggregates. A second experiment was conducted in the same manner using a solution containing half as much PRG in an attempt to limit aggregation, but similar results were observed. For comparison, a photograph of the wafer grafted with polymer-bound PRG is shown in Figure 4.5. This result clearly indicates that polymer-bound PRGs are superior to small molecule PRGs for the purpose of free radical graft polymerization lithography.



Figure 4.4 Photograph of polymer grafted onto a film of styrene containing Irgacure 2959, a non-bound PRG. As can be seen the surface is quite rough and is unsuitable for lithography.



Figure 4.5 Photograph of a polymer grafted onto a film of PRG1, a polymer-bound PRG. This film is quite smooth. The reflection of books can be seen on the wafer.

A control experiment was then done to show that the PRG in the previous experiment was indeed responsible for the grafting. The wafer with pure polystyrene containing no PRG was then subjected to the same experimental conditions. Figure 4.6 below clearly shows that there was no change in thickness when the light was turned on.

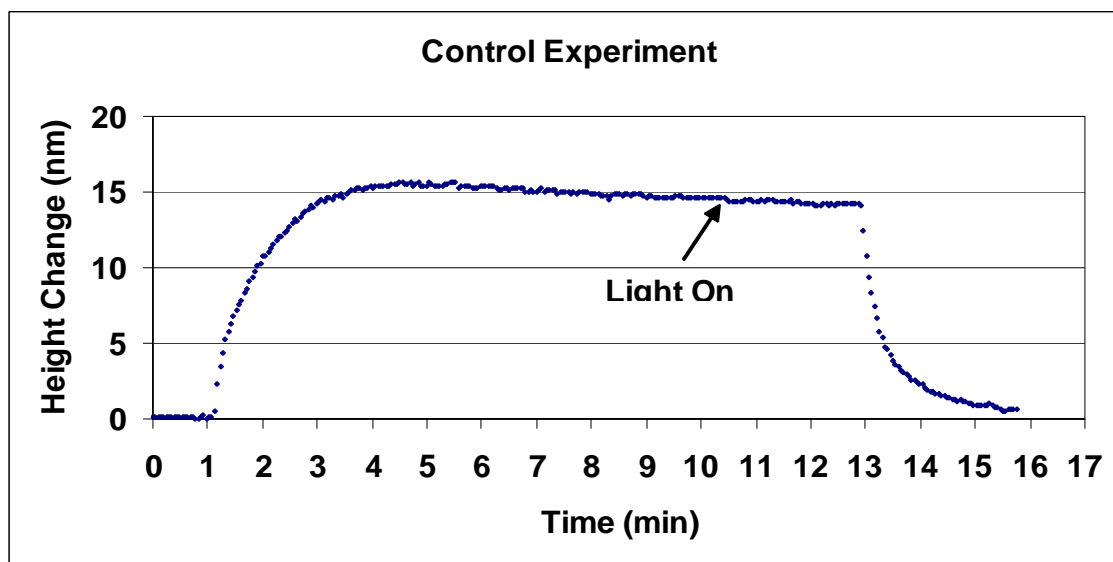


Figure 4.6 Control experiment showing only the absorption and desorption of monomer when no PRG is present. No thickness change was observed when the film was irradiated with UV light.

Now that the chamber had been fully tested and verified to work correctly, it was time to test the silicon containing monomer for activity. An experiment similar to the one described above was performed, and Figure 4.7 shows ellipsometer data from grafting the difunctional silicon containing monomer. The monomer was found to be active although a higher temperature, 100°C, was required to achieve growth. The vapor pressure of this monomer at 100°C is only 12.9 torr, which could explain why it is more difficult to achieve growth.

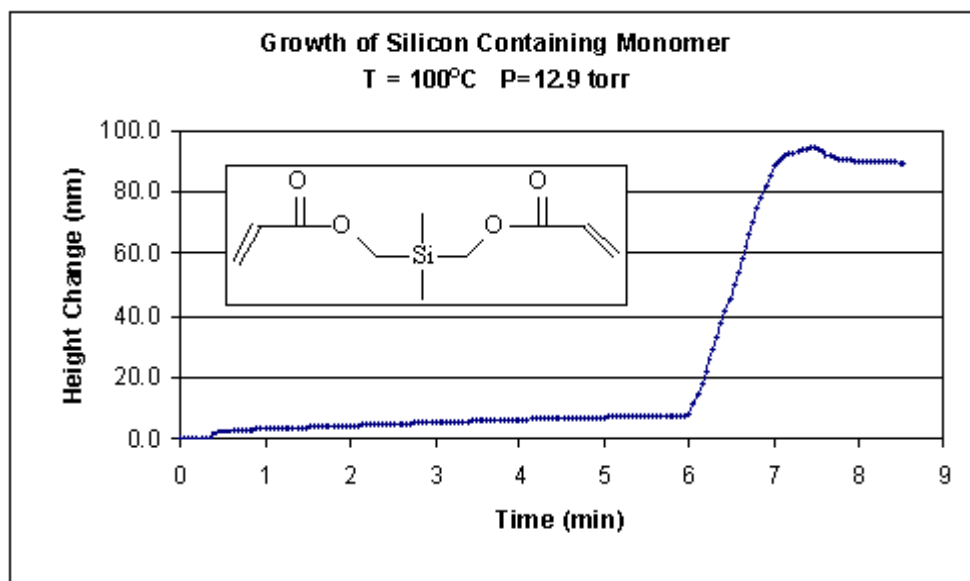


Figure 4.7 Grafting results with the difunctional silicon containing monomer

Only one proof of concept remained. The imaging scheme that had been decided on requires that the PRG be permanently quenched upon irradiation under oxygen. Quenching was performed by irradiating a wafer with a high dose of UV light in the presence of oxygen. Both wafers were grafted under the same experimental conditions as described above. A comparison of growth between quenched and unquenched PRG was performed. Data from this trial is shown in Figure 4.8 below. This experiment shows that good contrast can be achieved between quenched and unquenched material, but some small amount of background silylation will occur. From a practical standpoint, this result is not a problem as long as the background growth is not large compared to the height of the graft. In that case, a breakthrough etch can remove the unwanted silicon containing material, but if the residual layer is too thick, it becomes very difficult to etch it away without damaging the grafts.

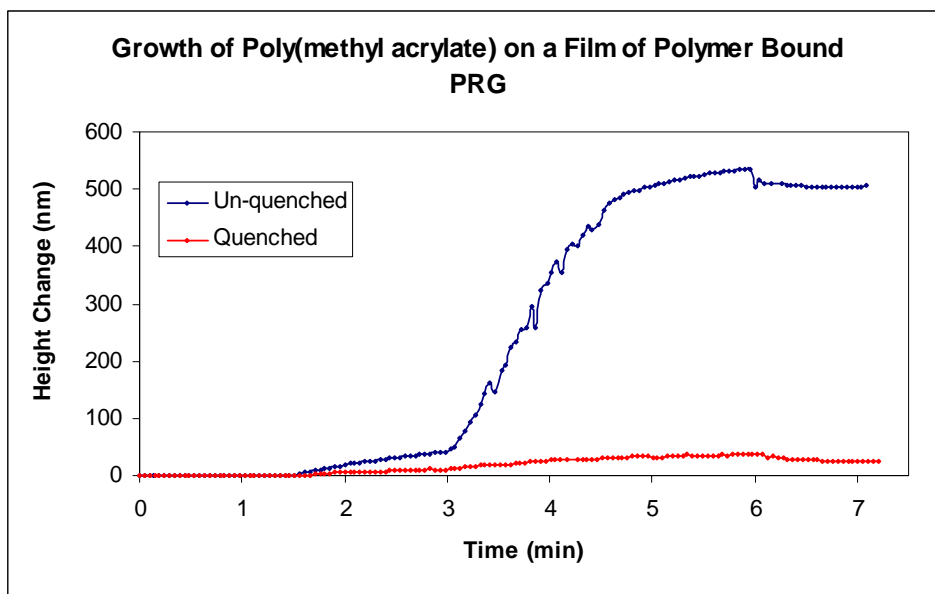


Figure 4.8 Contrast between quenched and unquenched growth

4.3 KINETIC STUDIES

The ellipsometer chamber is ideal to study the kinetics of grafting, and now that the materials and chamber have been verified to function as expected, some experiments were performed to examine the kinetics of the grafting process. These studies were conducted using methyl methacrylate (MMA) as the graft monomer. Figure 4.9 shows the pressure dependence of the grafting process. Figure 4.10 shows the dependence of the grafting process on UV light source intensity.

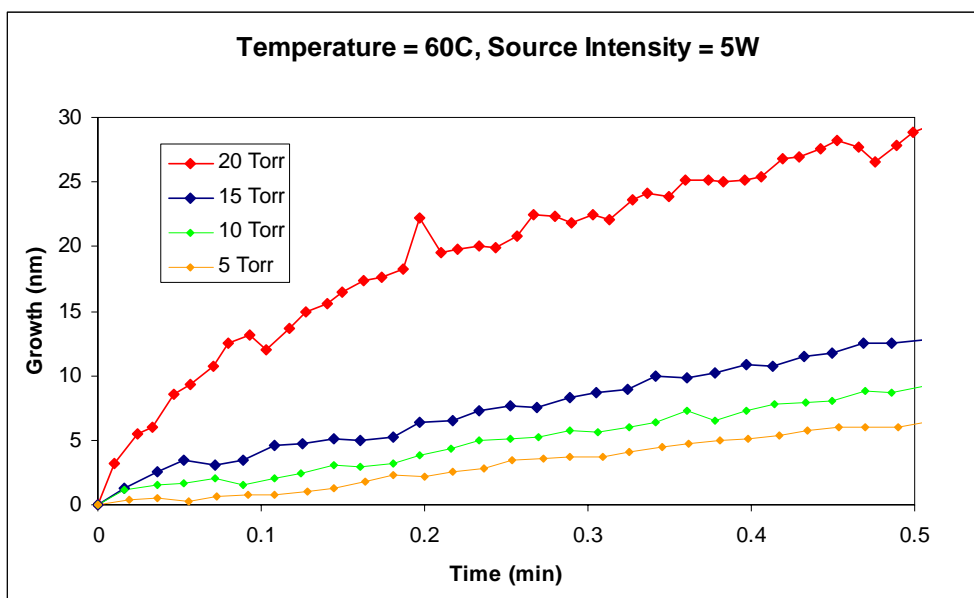


Figure 4.9 Pressure dependence of the grafting process

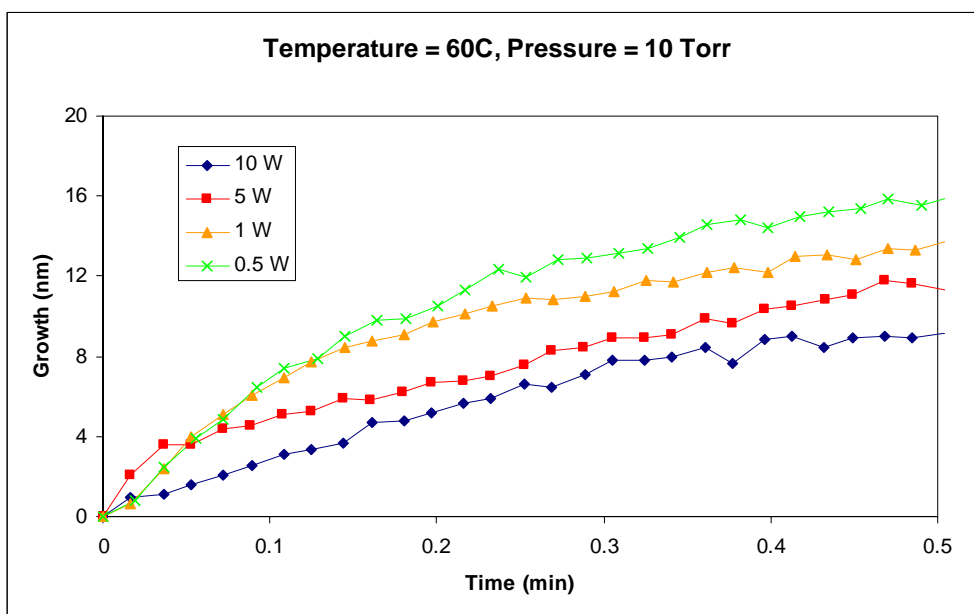


Figure 4.10 Source intensity dependence of the grafting process

The through pressure behavior was as expected, but the through lamp power behavior was not. As can be seen, higher lamp power leads to less growth. This result is possibly due to a larger number of radical-radical recombinations or other quenching events of the photoinitiator at higher lamp intensities. In other words, the principle of reciprocity is not maintained. The principle states that the number of photons a photoresist is dosed with, not the exposure time or source intensity, is what determines photoresist behavior.

Now that a basic understanding of the grafting process had been achieved, a more detailed analysis of the quenching and imaging process was undertaken. A simple simulation was designed to predict the shape of a polymer graft given a particular quenching aerial image used to pattern the wafer. This simulation was based on two simplifying assumptions that could be considered to be a “best-case scenario” for grafting. The first assumption is that all growth is perfectly vertical. The second assumption is that the height of the graft is dependant only on the quenching dose. Under this assumption it is assumed that the height of a graft is a fraction of the unquenched graft height as determined by the quenching efficiency, a quantity that can be measured. Figure 4.11 shows an example of what quenching efficiency might look like. An aerial image can be simulated using commercial software like PROLITH from KLA Tencor. Figure 4.12 shows an aerial image simulation for 160nm nested lines (wavelength=248nm, numerical aperture=0.6, partial coherence=0.6, dose=400mJ/cm²). By coupling the aerial image simulation with the quenching efficiency, a best case prediction of what the grafted feature might look like can be generated. Figure 4.13 shows an example of this result. Given a lower contrast quenching efficiency curve, less ideal grafts are obtained. Figure 4.14 shows a linear quenching efficiency plot, and Figure 4.15 below shows grafted profile that would be obtained from such a system.

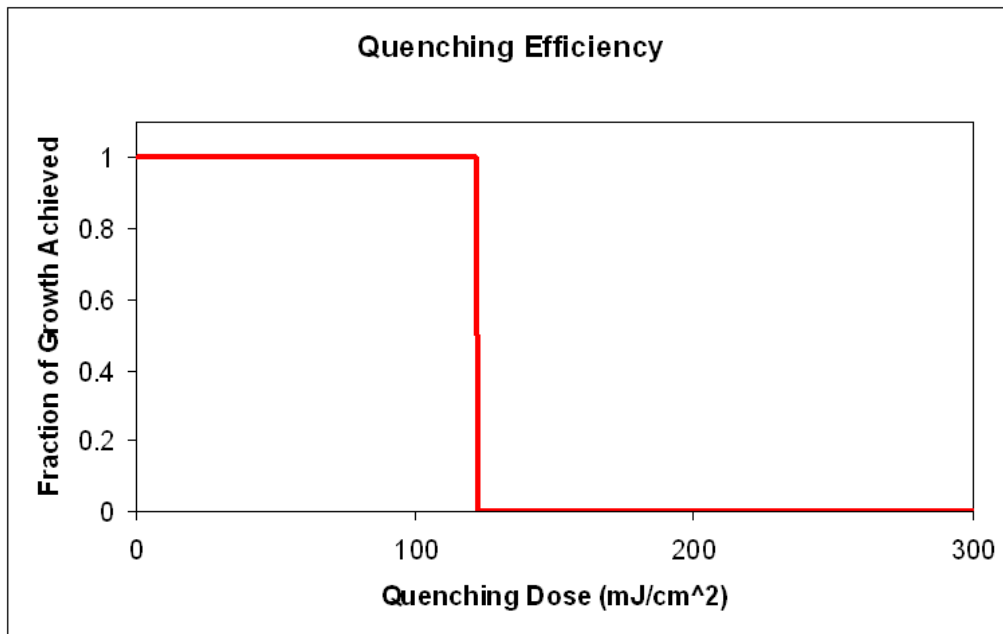


Figure 4.11 Ideal quenching efficiency as a function of quenching dose

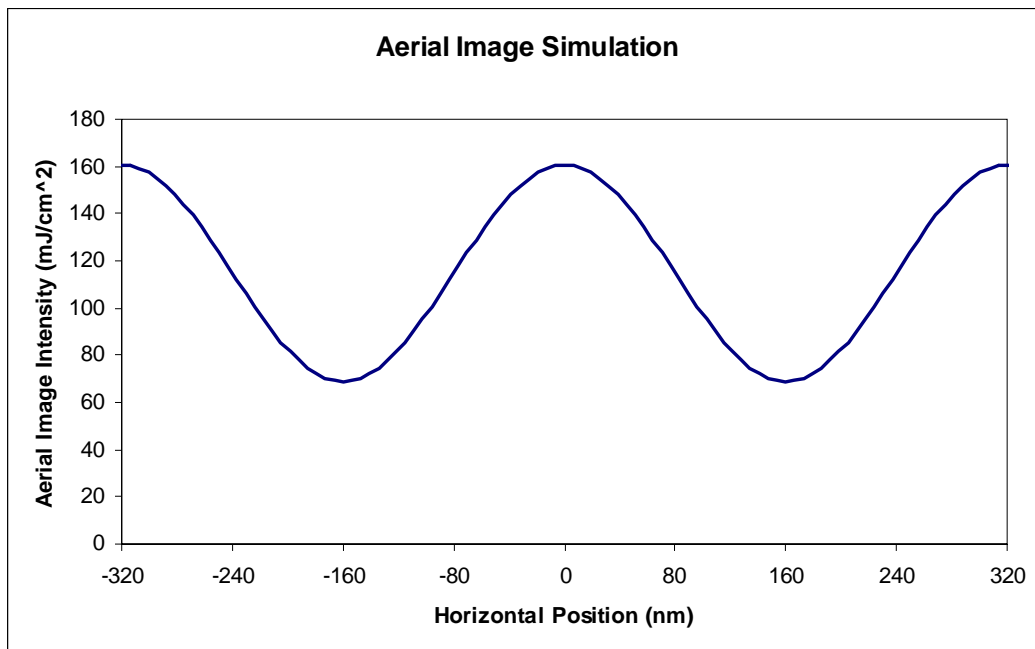


Figure 4.12 PROLITH Simulation of the aerial image of 160nm nested lines

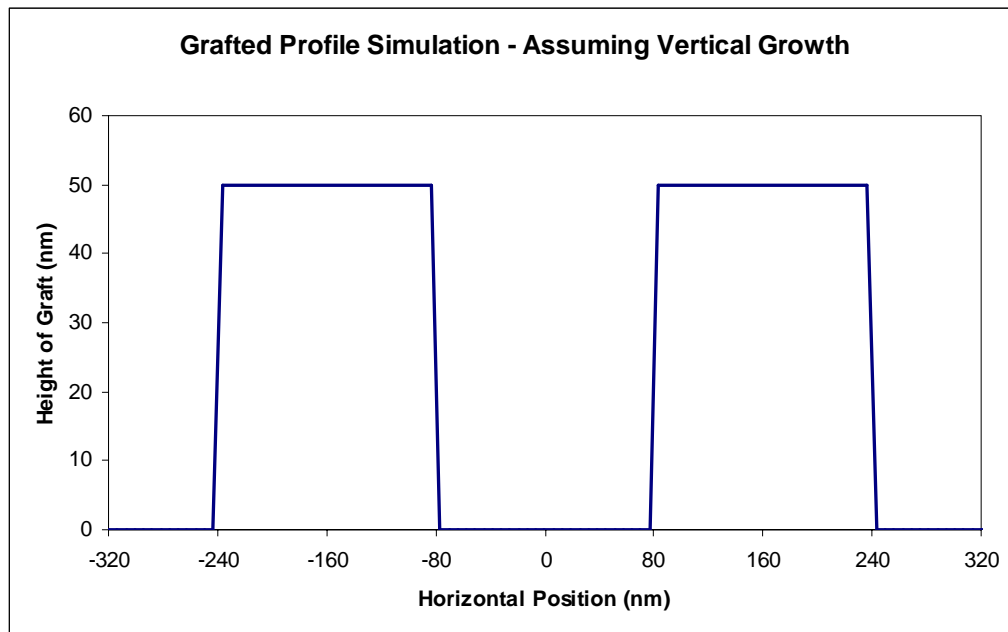


Figure 4.13 Simulated grafted profile given the above aerial image simulation and ideal quenching efficiency

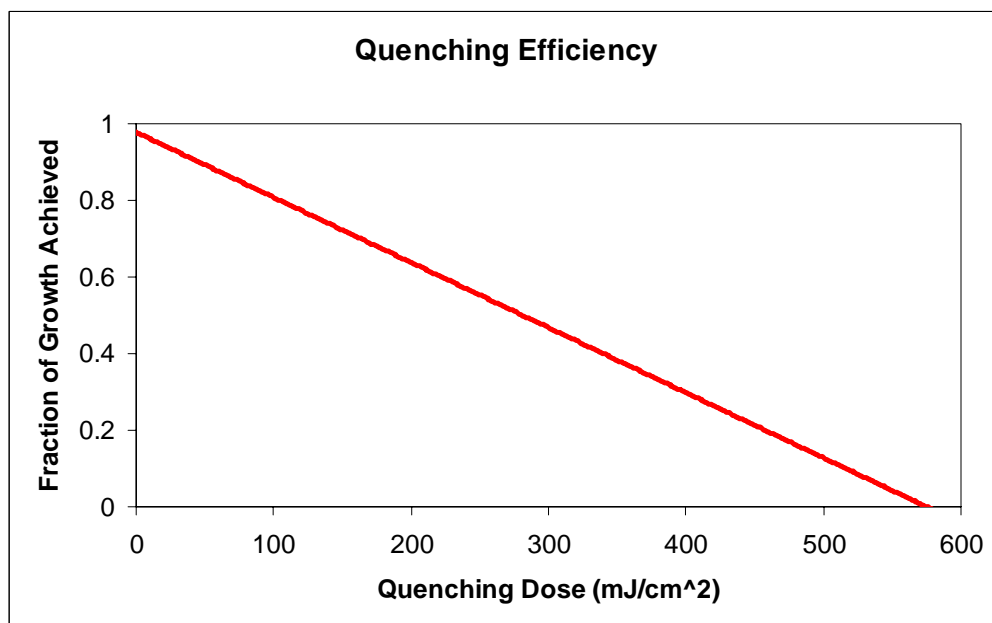


Figure 4.14 Linear quenching efficiency as a function of quenching dose

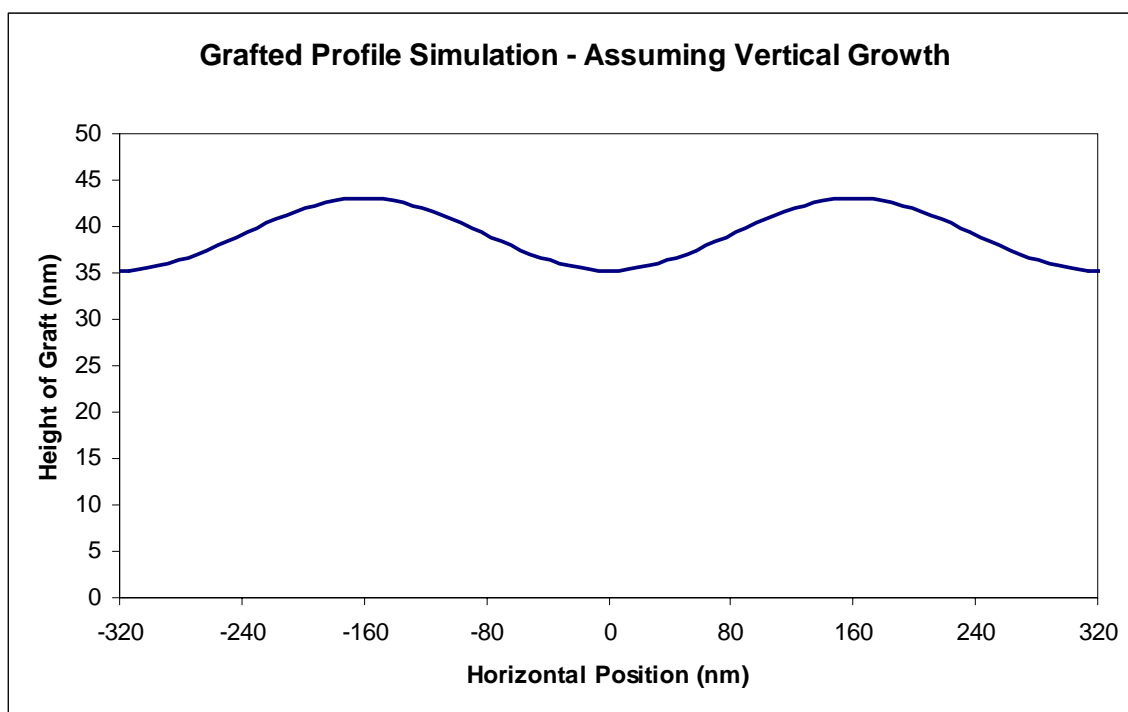


Figure 4.15 Simulated grafted profile given the above aerial image simulation and linear quenching efficiency

Clearly the profile generated from the linear case would be unacceptable for lithography. This result occurred because, according to the linear quenching efficiency, no additional contrast is gained from the quenching process. All the contrast in the system must come from the aerial image, and in this case, the aerial image contrast is insufficient at this imaging condition. In other words, 160nm nested lines could not be resolved in this case.

Data were collected to examine the quenching efficiency of an actual graft. In this example case, MMA was chosen as the monomer. Grafts were made using a 30 second graft time, a source intensity of 10 Watts, a temperature of 60 degrees Celsius, and a monomer pressure of 15 torr. These data are shown in Figure 4.16, where data points are indicated as dots. In order to determine the quenching efficiency at any

arbitrary dose, the data must be fit with a function. In this case, an arbitrary function was chosen to match the shape of the data. This fit is shown in Figure 4.16 by a solid red line. Using the aerial image from Figure 4.12 above, the grafted profile was simulated as shown in Figure 4.17.

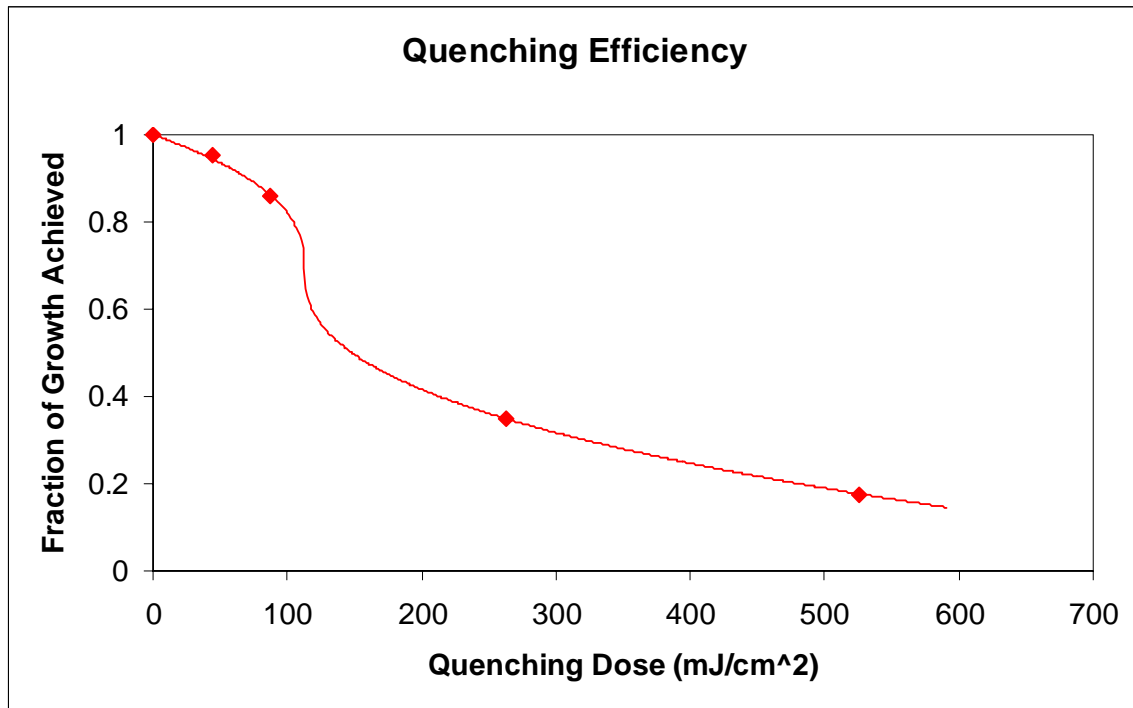


Figure 4.16 Actual quenching efficiency data fit with an arbitrary function to match the shape of the data

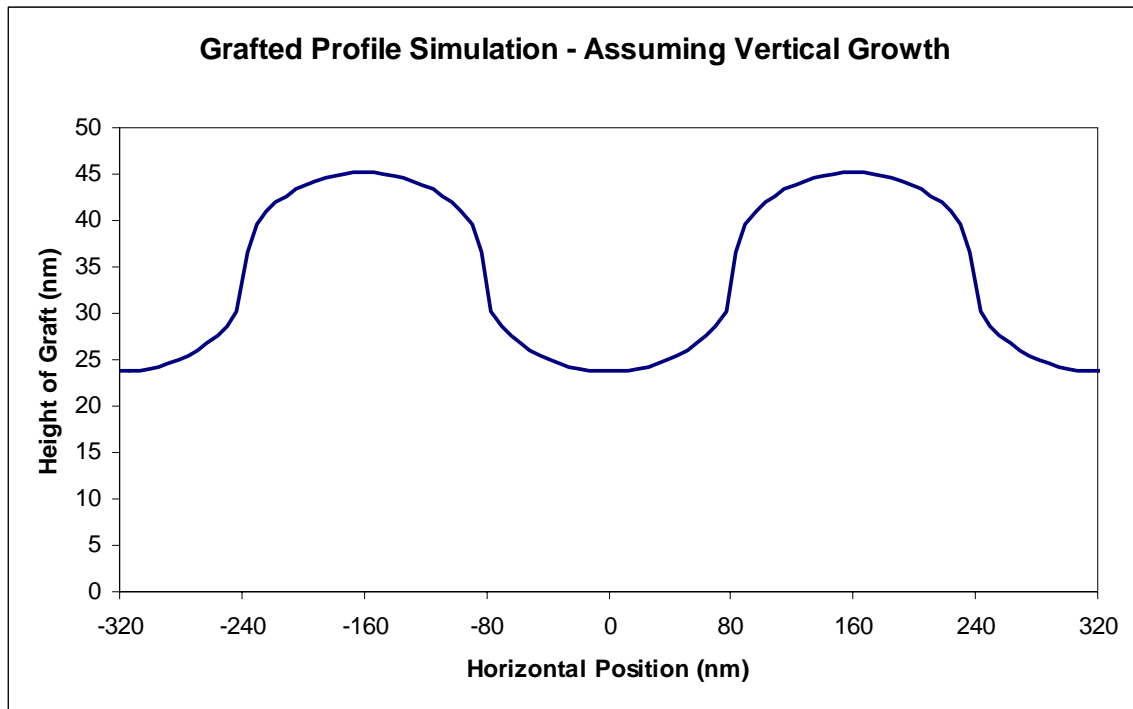


Figure 4.17 Simulated grafted profile based on the measured quenching efficiency

In this case, some contrast was gained through the quenching process. Unfortunately, it was observed that an extremely high dose is required to fully quench the film. Even at a dose of $500\text{mJ}/\text{cm}^2$, the grafted film height was still 20 percent of the unquenched height. Doses that high are impractical from a manufacturing standpoint because of throughput issues, and even with high doses, the contrast of this system is low compared to standard lithographic processes. As a result, the dry develop step becomes very difficult. An extremely anisotropic breakthrough etch would be required to remove the residual layer without destroying the grafts. In the example case shown in Figure 4.17 only 20nm of grafted material are present on top of a 25nm residual layer, and that simulation was generated with the assumption of perfectly vertical growth. Based on the result of this simulation, it is thought that high resolution patterning with free radical

graft polymerization lithography will be extremely difficult and that the most likely chance for a successful graft would be in a case where an extremely high contrast aerial image could be generated. Such a case would be possible in a stepper operating far below its resolution limit or in an alternate imaging scheme such as a contact printing.

After these kinetic trials were completed, a film of cloudy polymer was found on the inside of the quartz window of the grafting chamber indicating that the light had caused the monomer to polymerize on the window. This autopolymerization of the monomer on the window presents yet another drawback of using this process for free radical grafting.

4.4 IMAGING EXPERIMENTS

Despite the discouraging results from kinetic simulation, it was decided to move forward with the imaging portion of this project to fulfill deliverables from the project grant contract. Early attempts to grow features involved a contact printing technique that involved placing a photomask on top of a silicon wafer coated with PRG and exposing. This method of contact printing is a relatively low resolution technique; hence, only a resolution of approximately five microns was achieved. The process was far from optimized, however, and more work remains to achieve higher resolution results. Figure 4.18 shows scanning electron microscope (SEM) images of these features.

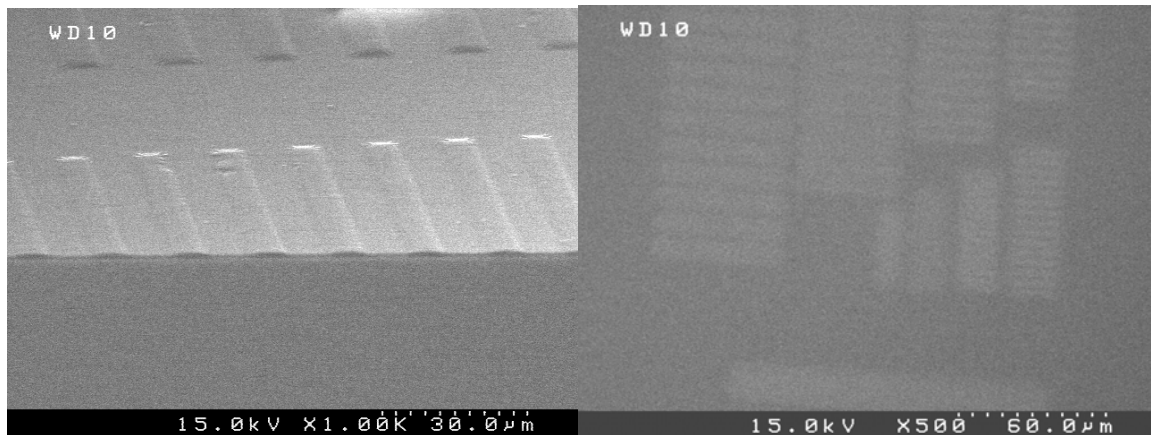


Figure 4.18 SEMs of features printed by contact printing

A higher resolution imaging process was desired, and plans were made to image wafers at International SEMATECH. Wafers were coated with the PRG on an FSI Polaris 2000. Wafers were exposed on an SVG Microscan III, using conventional illumination ($NA = 0.6$, $\sigma = 0.6$). Wafers were exposed with a test pattern at a dose of 50mJ. This wafer was then cleaved and grafted with MMA. An optical micrograph of this wafer is shown in Figure 4.19. Figure 4.20 shows an SEM image of 500nm nested lines on this wafer. The grafts appear to be very small and not well formed, which tends to agree with the simulation in Figure 4.17.

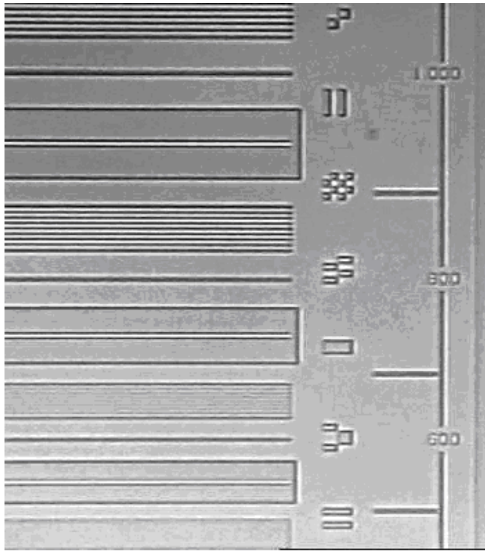


Figure 4.19 Optical micrograph of higher resolution grafted images

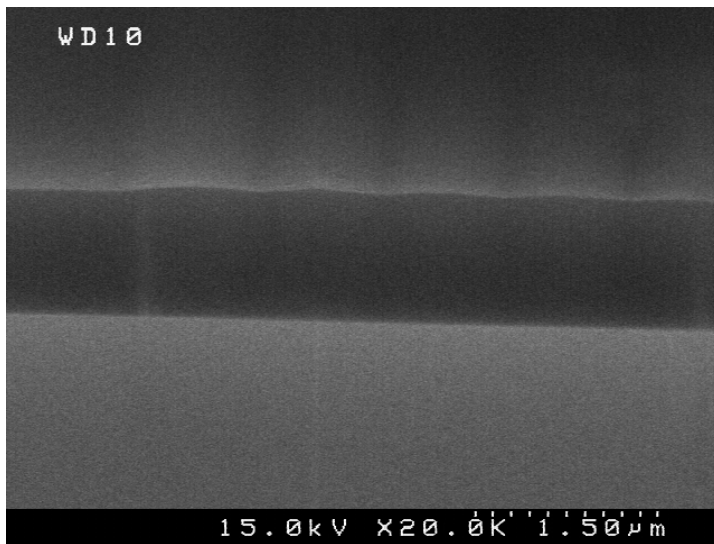


Figure 4.20 SEM image of 500nm nested lines grafted with MMA

A second wafer, imaged in the same way as the first one, was grafted with the difunctional silicon containing monomer. This wafer was taken to the Plasmatherm etcher at Pickle Research Center and etched under an oxygen plasma. Figure 4.21 and

Figure 4.22 show several top-down SEM images of the etched wafer. Figure 4.23 shows several cross sections of the same wafer.

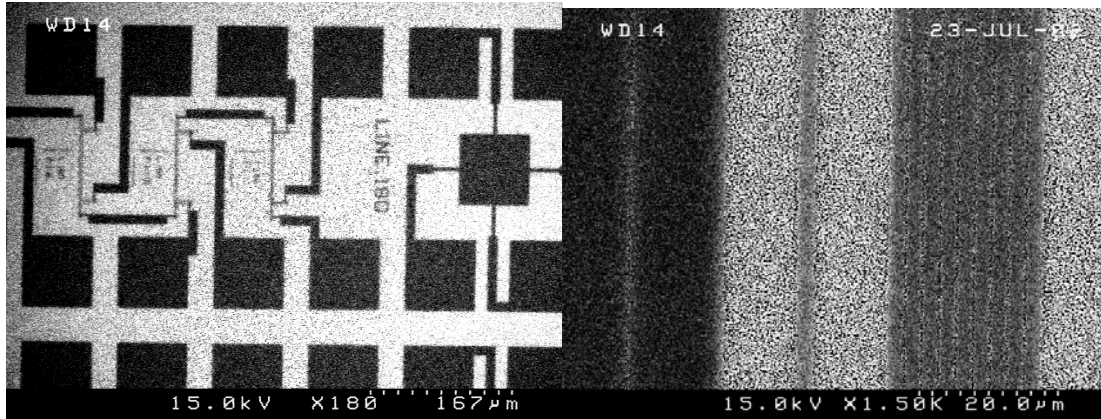


Figure 4.21 Top down SEM images of the etched wafer fragment

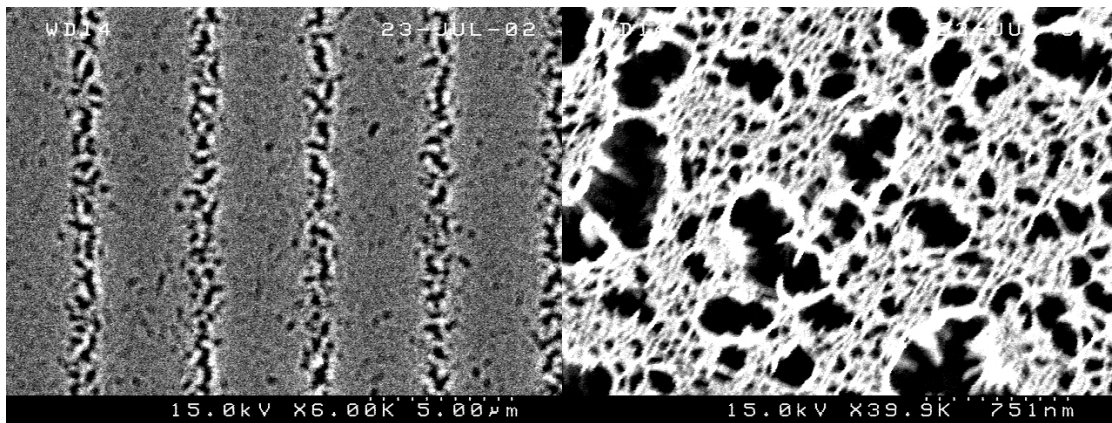


Figure 4.22 Higher magnification SEMs of etched, silicon-grafted wafers

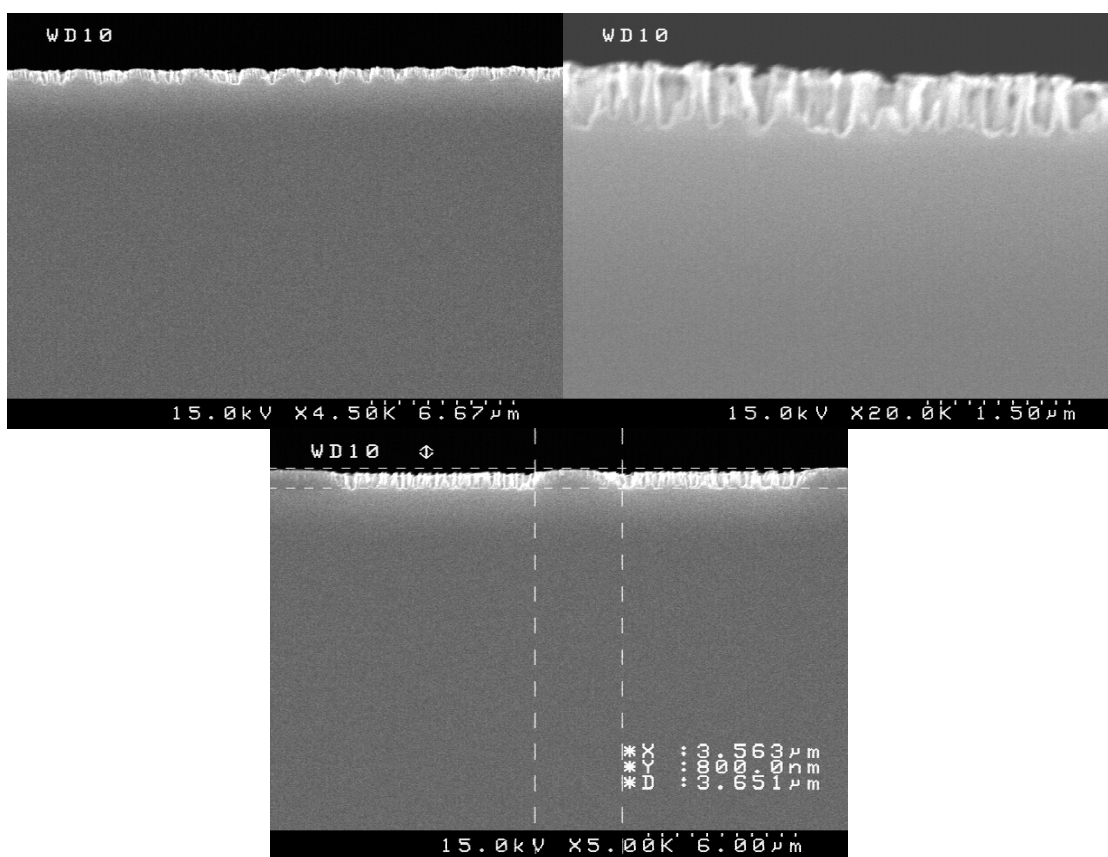


Figure 4.23 Cross section SEMs of etched, silicon-grafted wafers

As can be seen by the above series of SEM images, the etch results were not good. This failure was attributed to the poor quality of the etcher used. The only higher quality etcher available was located at International SEMATECH. This etcher, however, can only accept full 8-inch wafers. Unfortunately, the grafting chamber that had been used up until this point can only accommodate wafers and wafer fragments up to 2 inches in size. Initially, it was thought that small wafer fragments could be grafted and then glued to an 8-inch wafer, which could be run through the SEMATECH etcher. Upon investigation, however, it was found that etching glued wafers is against SEMATECH

policy. Therefore, in order to demonstrate the etch process, a larger grafting chamber was needed.

4.5 DESIGN AND IMAGING RESULTS FROM THE LARGER WAFER CHAMBER

To that end, a commercial genesis silylation tool, obtained through the generous donation of Texas Instruments, was gutted and completely remade to suit our needs. A window was installed on the lower plate of the tool to allow light to be shined on the wafer. The entire monomer delivery system was removed and replaced with a different mechanism. A larger charging chamber was added to allow higher pressures, and also three monomer delivery lines were added to allow multiple gasses. Finally the entire control system was removed and replaced with a custom LabVIEW interface. A schematic of the tool is shown in Figure 4.24, and a photograph of the tool is shown in Figure 4.25. This tool was tested and found to be functional. An optical micrograph of the first graft made on this tool is shown in Figure 4.26.

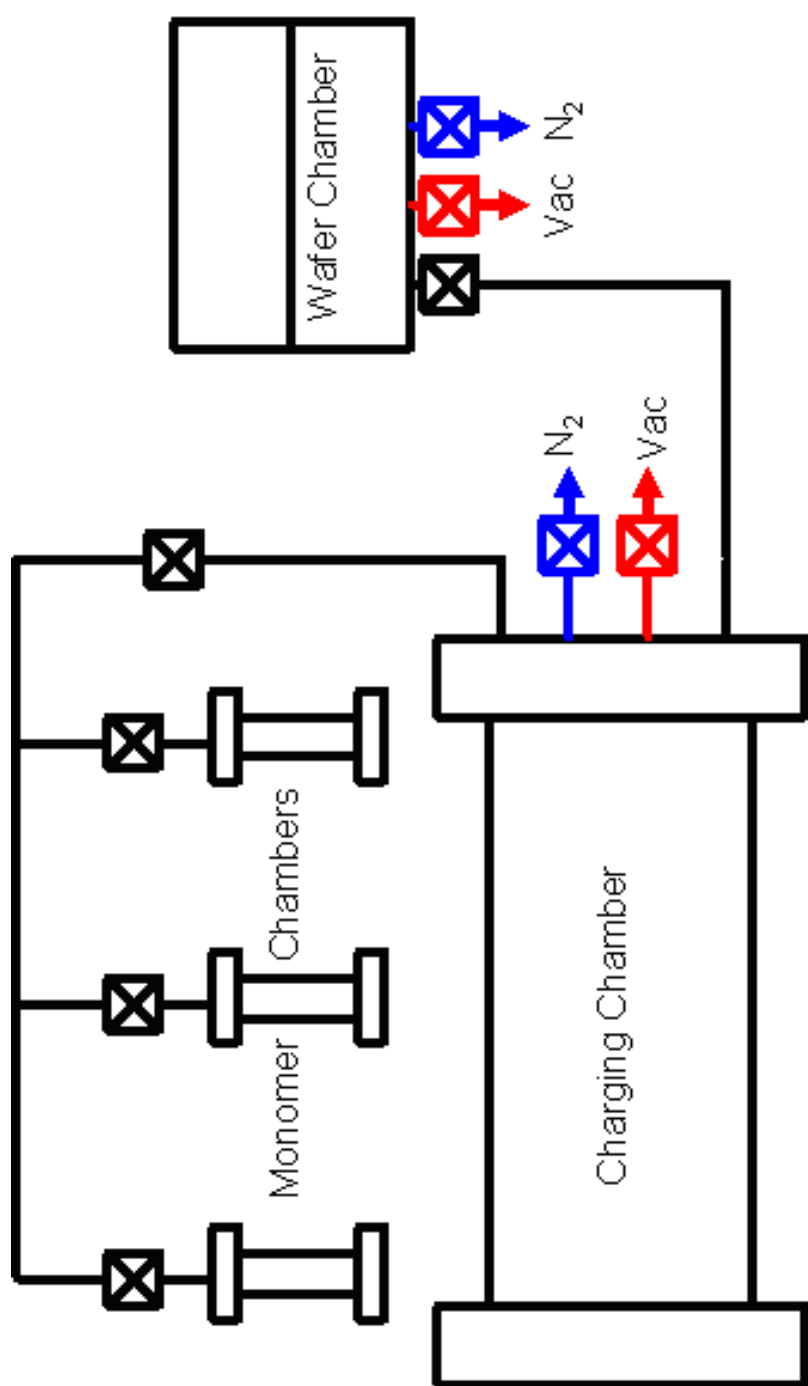


Figure 4.24 Schematic of the large wafer chamber

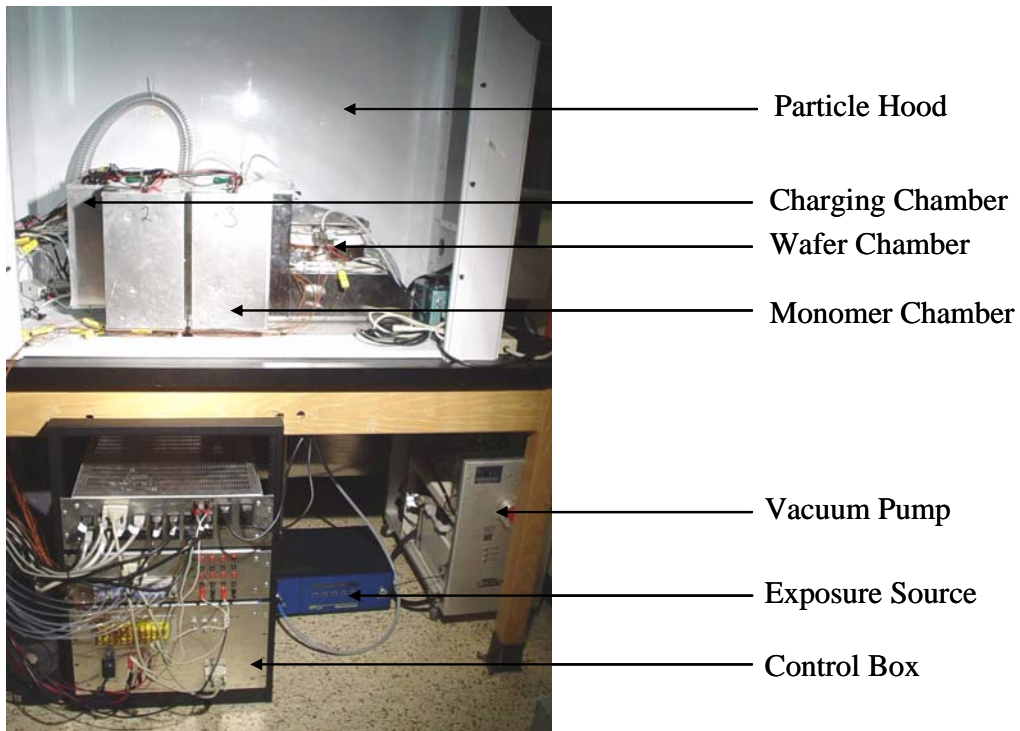


Figure 4.25 Photograph of the large wafer chamber

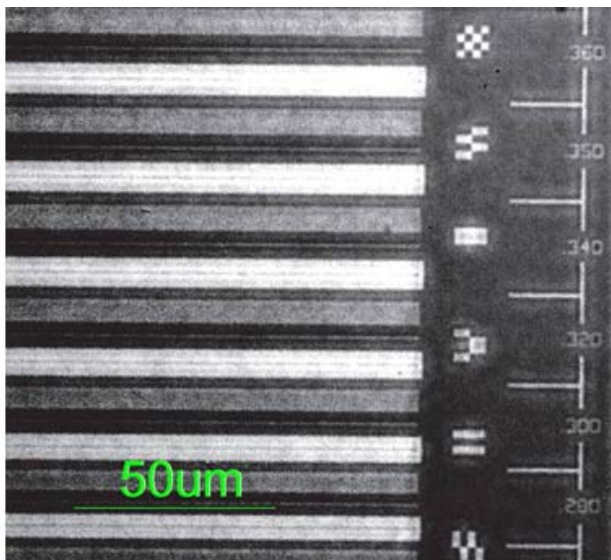


Figure 4.26 First grafted image using the new tool

4.6 CONCLUSIONS AND RECOMMENDATIONS

The goal of this project was to develop a scheme for free radical graft polymerization lithography. Materials were synthesized, equipment was constructed, and the process was developed. With the eventual successful etch transfer of a grafted image, the process was demonstrated from start to finish. At this point, the remaining issue is to determine if the process works well enough to merit further investigation.

There are numerous drawbacks to using this technique as opposed to cationic grafting or even conventional lithography. First, it was observed that high doses are required to fully quench the base layer materials used in this study. Furthermore, the quenching process was observed to be very low contrast. These two factors tend to indicate that high resolution patterning with this technique would be difficult if not impossible. As a result, this technique seems to be more suitable for patterning larger features that have high contrast aerial images such as those much larger than the resolution limit of a stepper or those printed with techniques such as contact printing. Furthermore, even the large features were observed to grow grafts with rounded profiles possibly because of isotropic growth of the grafted polymer. The “rolling hills” shaped grafts are much more difficult to etch than are square shaped profiles generated in conventional lithography. This fact adds further complexity to the process. Also, the monomers used in these grafting studies were observed to undergo autopolymerization on the surfaces of the windows of the chamber on exposure to UV light. This unintended effect causes a cloudy film to build up on the inside of expensive and hard to clean surfaces in the grafting chamber.

These difficulties all indicate that this process will most likely not become a useful patterning technique. Conventional lithography or even cationic graft polymerization lithography can generate higher resolution images with much greater

ease. Because of these many drawbacks, it was decided not to devote further efforts to the study of this process. If future researchers were interested in pursuing this project, the current imaging scheme should most likely be abandoned. Based on the results of these experiments, any process requiring the quenching of an active species to allow grafting in the unexposed areas is not recommended. The reason behind this recommendation is high doses are required to achieve high levels of quenching, and even then incomplete quenching will likely be achieved. Instead, researchers should develop a light-activated species. Furthermore, the photo radical generator used in these studies should probably be replaced with a thermal radical generator. Even though the grafting process may be significantly slower in a thermal process, the use of a thermal radical generator would eliminate the need for exposure during the grafting process as well as the possibility of fouling the chamber windows with undesired polymer. The development of a thermally stable species that on exposure to UV radiation becomes a thermal radical generator is a challenging chemistry project that is beyond the scope of this work. Finally, perhaps the idea of using a living free radical initiator should be revisited to eliminate entirely the oxygen sensitivity issue.

Chapter 5: Neutralization Byproducts in Photoresists

5.1 INTRODUCTION

Base quenchers have been used in photoresist formulations for over a decade because they were found to limit acid diffusion and combat problems such as T-topping, but surprisingly, little is known about how they actually function within a resist film. Different resist manufacturers use different bases or even combinations of bases to yield the best results. Commercial photoresist formulations are often established by trial and error empiricism. Very little literature even exists that describes exactly how bases influence lithographic performance to guide future efforts. Base quenchers have been observed to influence properties such as iso-nested bias, dissolution rate, diffusion bias, and even resist contrast. As time progresses and the limits of lithography are stretched to produce increasingly smaller features, it becomes more and more critical to obtain a quantitative understanding of exactly how base quenchers work.

Historically, most if not all models of photoresist systems have viewed base quenchers as an acid trap. In other words, when a base molecule reacts with an acid molecule, the product is assumed to be inert and drops out of consideration. Furthermore, there is little understanding of the kinetics by which that neutralization occurs. General chemistry indicates that the product of an acid base reaction is a salt, so the initial focus of this project was to determine the properties of this salt. General chemistry also indicates that typical acid base reactions are equilibrium reactions. In the case of photoresist systems, the acid tends to be strong, while the base is usually much weaker. This type of system should favor a high equilibrium concentration of salt, and the resulting salt should have a slightly acidic pH. Given this information, it seems entirely possible that the salt formed by the acid base neutralization could either

decompose to regenerate photoacid or be acidic enough itself to catalyze the deprotection of the resist.

Perhaps this concept is best illustrated with an example. In the simplest case, one could imagine the reversible reaction of ammonia with triflic acid, the photoacid produced from the PAG triphenylsulfonium triflate. This reaction is shown below in Figure 5.1. As you can see, this reaction is an equilibrium reaction. To some extent, the salt formed by the reaction of acid and base could potentially decompose to regenerate triflic acid. In this example in particular, ammonia is volatile, so any ammonia present in the resist should volatilize out of the film thereby driving the equilibrium to the left and generating triflic acid.

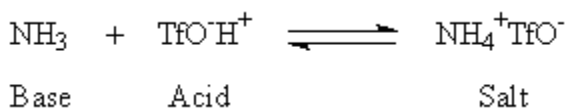


Figure 5.1 Acid base equilibrium

In order to study the influence of salts in photoresist films, it was decided to isolate the salt formed by the reaction of photoacid and base in order to directly study that molecule. Prior research has been performed on these salts; however, that research has been primarily focused on the influence of these salts on post exposure delay (PED).^{61,62} Subsequent sections describe the synthesis of these salts and their evaluation in photoresist films.

5.2 SALT STUDIES

With the goal of studying the influence of salts in photoresist films, several salts were synthesized. In general, the salts were synthesized by adding the appropriate acid to

a ten percent excess of the base of interest. This procedure was performed in a solvent in which both the acid and base, but not the salt, were soluble. This procedure ensured that the salt would precipitate out of solution and could be collected and washed with cold solvent to obtain a pure product. Once the salt was synthesized, it had to be evaluated for activity in photoresist films. To accomplish this goal, spin coated films of these salts dispersed in poly(t-butyloxycarbonyloxystyrene) (TBOC) and coated on silicon wafers were heated to typical post exposure bake temperatures while an FTIR was monitoring the film. TBOC is an excellent resist for evaluation in the IR because it possesses a prominent carbonyl peak at a wavenumber of approximately 1750cm^{-1} . This peak is only present in the protected form of TBOC. Once the polymer undergoes deprotection to become poly(hydroxystyrene) (PHOST), the peak disappears. If these salts are capable of generating acid and influencing photoresist deprotection, the t-butyloxycarbonyl protecting groups would be cleaved by the acid to form PHOST, and extent of reaction could be quantified monitoring the carbonyl peak in the IR. Further details of the experimental procedure can be found in the experimental section of this chapter.

The first salt produced by this method was the salt of trifluoromethanesulfonic acid (triflic acid) and the base imidazole. Triflic acid is the acid formed from the commonly used PAG triphenylsulfonium trifluoromethanesulfonate (TPS triflate). When this salt was tested for activity in photoresists, contrary to what is predicted from the acid trap model, deprotection of the photoresist was observed.

Early attempts to study these salts yielded unsatisfactory results. Figure 5.2 shows the results of baking four wafers coated with TBOC. One wafer contained no additives, and the second contained the TPS triflate. The TPS triflate wafer had been exposed to UV light to generate the acid. The final two wafers contained two different

batches of imidazolium triflate. The results from the two different salts showed a large discrepancy.

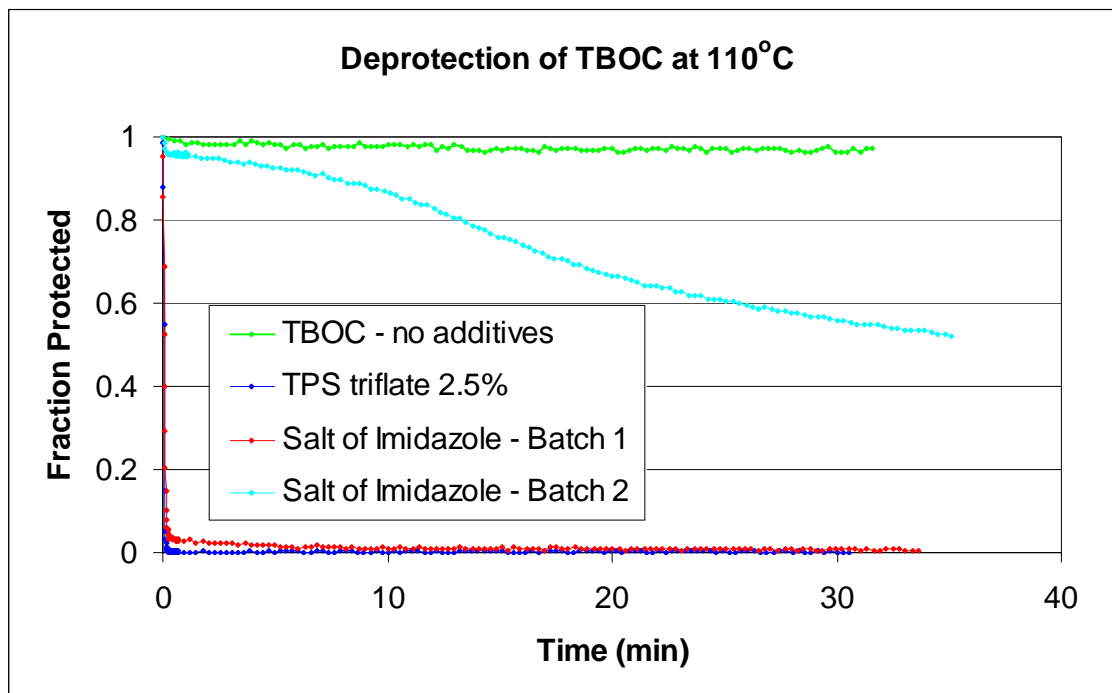


Figure 5.2 Initial results for the deprotection of TBOC at 110°C

Eventually, the source of this discrepancy was traced back to atmospheric humidity. It was found that these salts are hygroscopic. Furthermore, the nitrogen purged bag in which the initial salts were synthesized was found to leak. A third and fourth batch of the imidazolium triflate salts were synthesized in a new, airtight dry bag. These salts were also stored under nitrogen when not in use. With these new precautions in place, no further discrepancies in salt performance were observed. Figure 5.3 shows data to this effect.

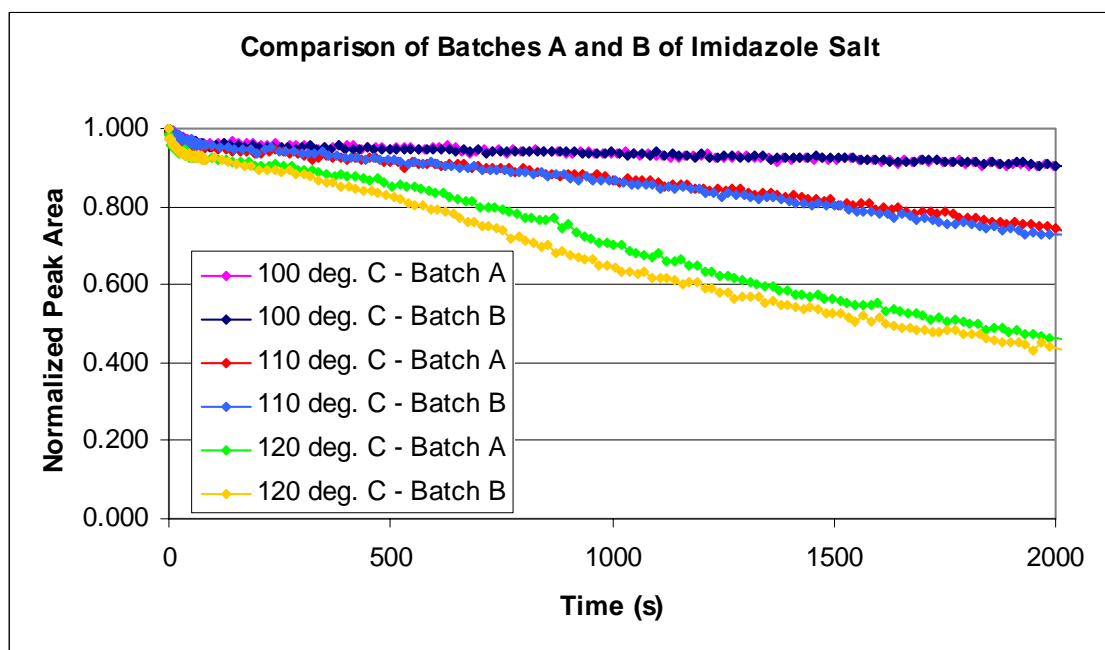


Figure 5.3 Comparison of two batches of the imidazolium triflate salt that had been synthesized and stored under dry conditions

A set of controls had to be collected to establish a point of comparison. A wafer was coated with pure TBOC and was analyzed on the IR at temperatures of 90, 100, 110, and 120 degrees Celsius. The TBOC showed no signs of decomposition at these temperatures. Next, a mixture of the TBOC solution and TPS triflate was prepared. The ratio of PAG to TBOC was 2.5 mole percent. First, the solution was run unexposed at temperatures of 90, 100, 110, and 120 degrees Celsius. These trials showed no deprotection of the resist. The trials were then repeated with samples that had been exposed to a high dose of ultraviolet light. In this case, high dose refers to a dose much higher than that which would be required to convert most of the PAG to acid. This dose was achieved by allowing the wafer to sit for at least 3 minutes under a 248nm UV lamp. Intensity was measured to be approximately 7mW/cm^2 , resulting in exposure doses of over one Joule. All exposures described in this chapter were performed in this manner.

At a temperature of 90 degrees Celsius, the reaction was too fast to extract useful data. Therefore, the experiment was repeated at temperatures of 40, 50, 60, and 70 degrees Celsius. These temperatures produced much more useful data, as seen in Figure 5.4 below.

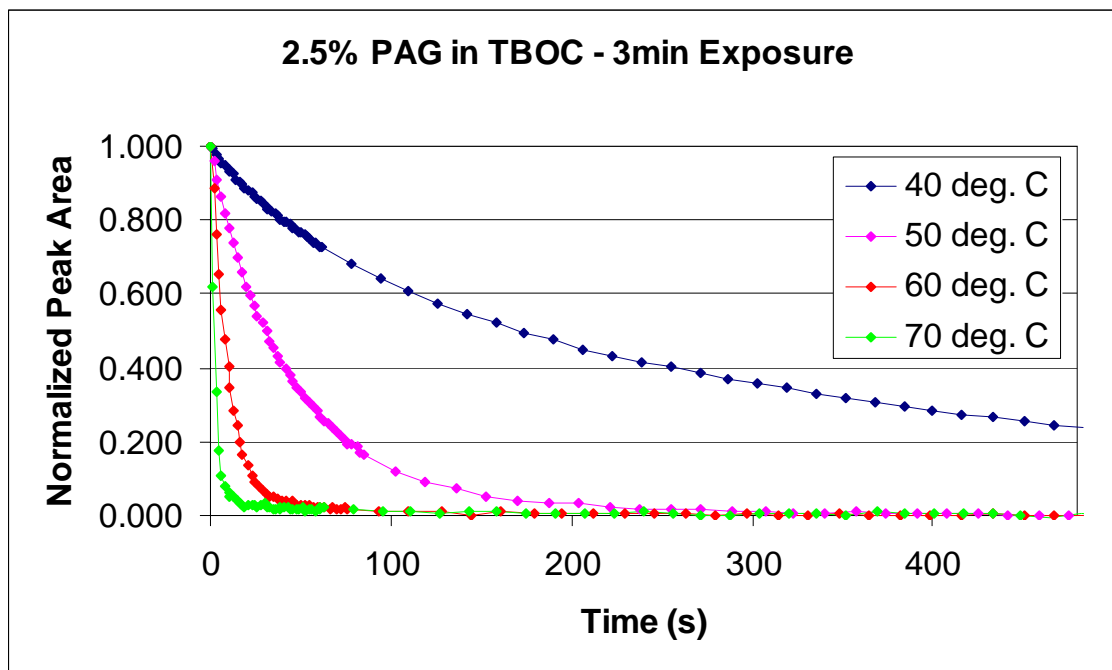


Figure 5.4 Deprotection of TBOC with triflic acid at low temperatures

The next step was to examine the effects of the base, imidazole, on the resist films. First, wafers containing 2.5 mole percent of imidazole were analyzed. Baking these wafers at 90, 100, 110, and 120 degrees Celsius yielded no reaction. A solution of 2.5 mole percent imidazole and 2.5 mole percent PAG was created, exposed, and tested at the same temperatures. The results are shown in Figure 5.5.

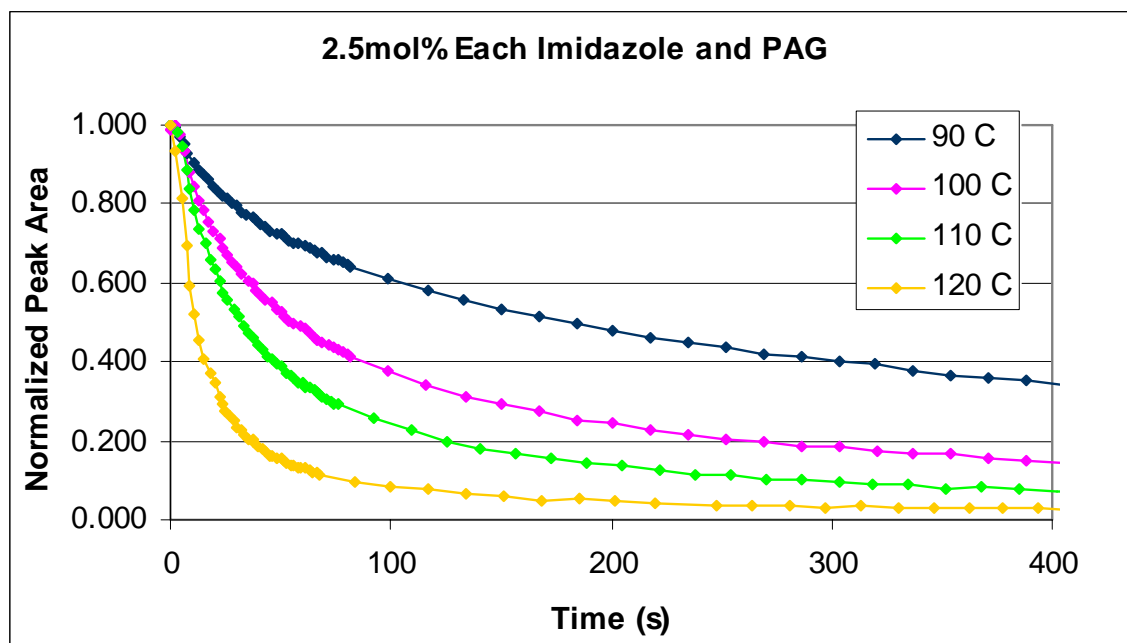


Figure 5.5 Deprotection of TBOC with an equimolar ratio of triflic acid and imidazole

As expected, the addition of base greatly slowed the deprotection reaction. It is notable that the deprotection reaction still occurs despite the fact that there is an equal amount of acid and base in the film. Based on the acid trap model, one might expect that all the acid would be quenched by the base and no reaction would occur. This was not the case. Furthermore, one might expect that an equimolar ratio of acid and base might react to quickly form the salt, and that this mixture might show the same behavior as an equivalent amount of the salt. This hypothesis was tested by evaluating a wafer containing 2.5 mole percent imidazolium triflate. These results are shown in Figure 5.6 below. Clearly, these results are different than those in Figure 5.5 above.

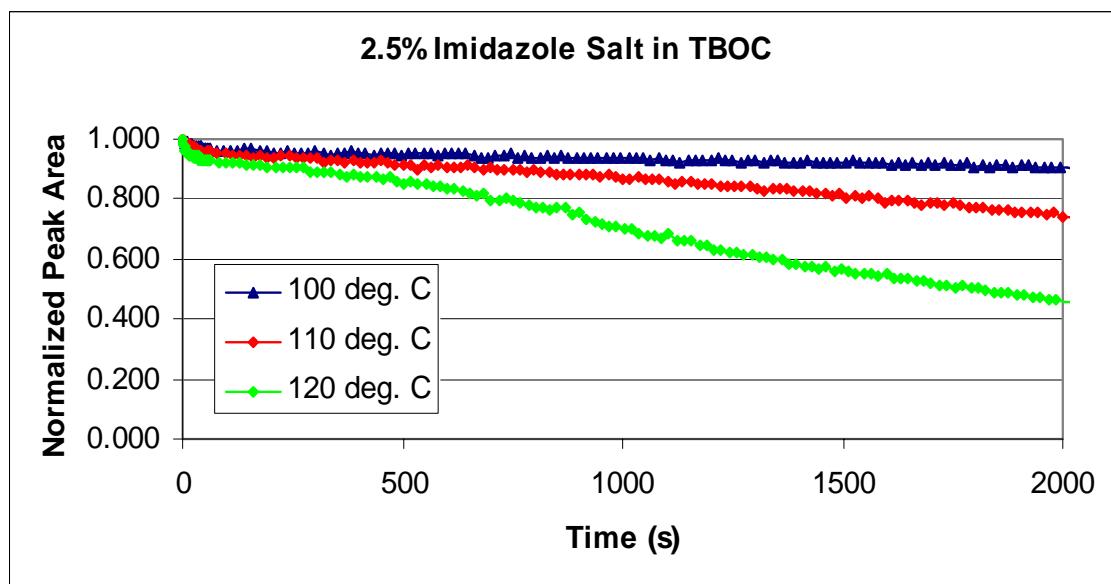


Figure 5.6 Deprotection of TBOC with the salt imidazolium triflate

This discrepancy between the results shown in Figure 5.5 and Figure 5.6 indicate a difference between the salt generated in the film and the salt added to the film. Likely this difference is caused because the neutralization of the acid and base inside a photoresist film is not instantaneous.

Finally, it was decided to see how the presence of salt influenced deprotection kinetics in the presence of exposed PAG. A solution of the salt and PAG in a 1:1 (2.5:2.5 mole percent) ratio was analyzed. The results are presented and are compared to the deprotection kinetics shown previously in Figure 5.4. Figure 5.7 shows this comparison. In this figure, the points represent mixtures of both PAG and salt, whereas the solid lines represent PAG alone. As can be seen, the presence of salt does not greatly influence the deprotection reaction.

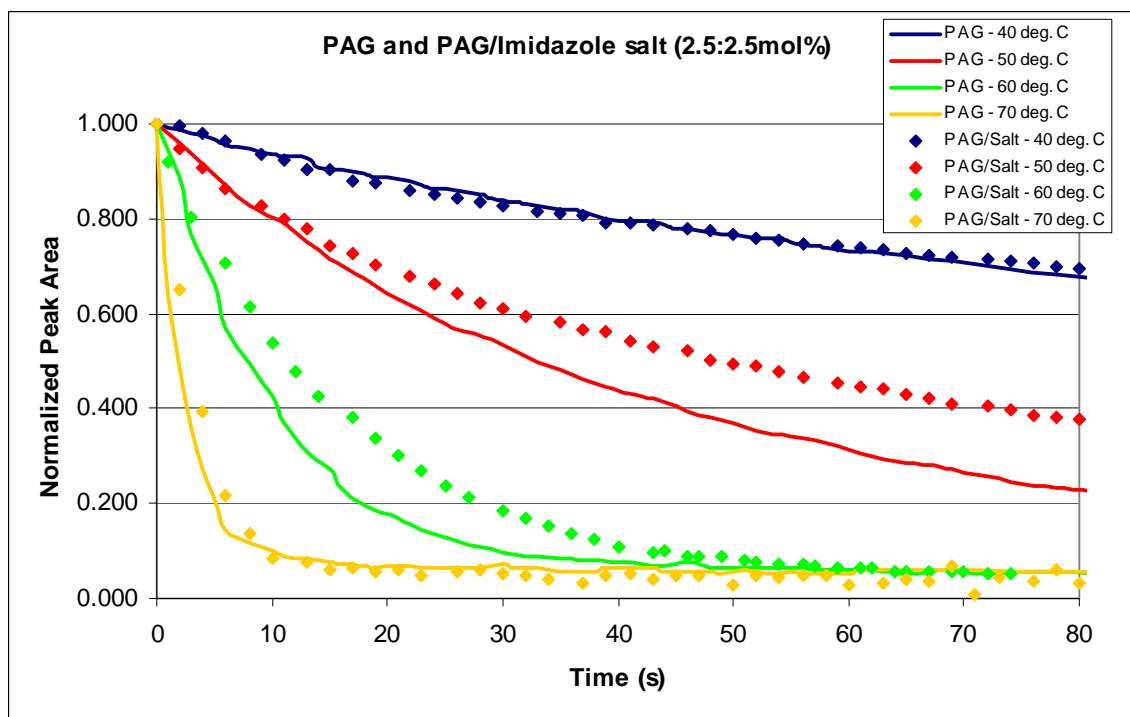


Figure 5.7 Comparison of the deprotection of TBOC with triflic acid alone versus a mixture of triflic acid and imidazolium triflate.

Finally, additional salts were both synthesized and purchased from commercial sources. In addition to the triflate salt of imidazole, the triflate salts diisopropylamine, tributylamine, morpholine, pyridine, and potassium hydroxide were synthesized. The triflate salts of ammonia and tetrabutylammonium hydroxide (TBAH) were purchased from Aldrich chemical company. The TBAH salt of perfluorobutanesulfonic acid was also purchased from Aldrich. Finally, the ammonium salts of triflic, acetic, and benzoic acid were purchased as well. All of these salts were tested for activity in photoresists. The results of these tests are summarized in Table 5.1 below.

Table 5.1 Acid and base components of various salts tested for activity in TBOC films

Acid	Base	Reaction Observed?
Triflic	Ammonia	Yes
Triflic	Imidazole	Yes
Triflic	Diisopropylamine	Yes
Triflic	Tributylamine	Yes
Triflic	Morpholine	Yes
Triflic	Pyridine	Yes
Acetic	Ammonia	No
Benzoic	Ammonia	No
Triflic	Potassium Hydroxide	No
Triflic	Tetrabutylammonium Hydroxide	No
Perfluorobutanesulfonic	Tetrabutylammonium Hydroxide	No

As can be seen from the above results, only the salts formed from the reaction of the strongest acids with amine bases, exhibited activity in the photoresist film. Amine salts of weaker acids did not deprotect the film. The salts of ionic bases also did not deprotect the film. It should also be noted that in all cases the rate at which the salts were observed to deprotect the photoresist film was very much slower than the rate at which free acid would deprotect the film.

One possible explanation for the non-reactivity of salts formed from ionic bases is the fundamentally different mechanism by which they react with acids, as shown in Figure 5.8. When an ionic base reacts with an acid, it forms a water molecule in addition to the salt; however, when an amine reacts with an acid, no water is formed. It is possible

that ionic bases require the presence of this water molecule in order to facilitate the deprotection reaction, but insufficient water is available in the photoresist film. It is also possible that because ionic bases tend to be stronger than amines, ionic bases simply bind the acid molecule more tightly than the amine is able to, thereby rendering the acid unable to deprotect the TBOC. Most likely, the salts of weaker acids were unable to deprotect the film because the acids themselves are not strong enough to facilitate the deprotection of photoresist.

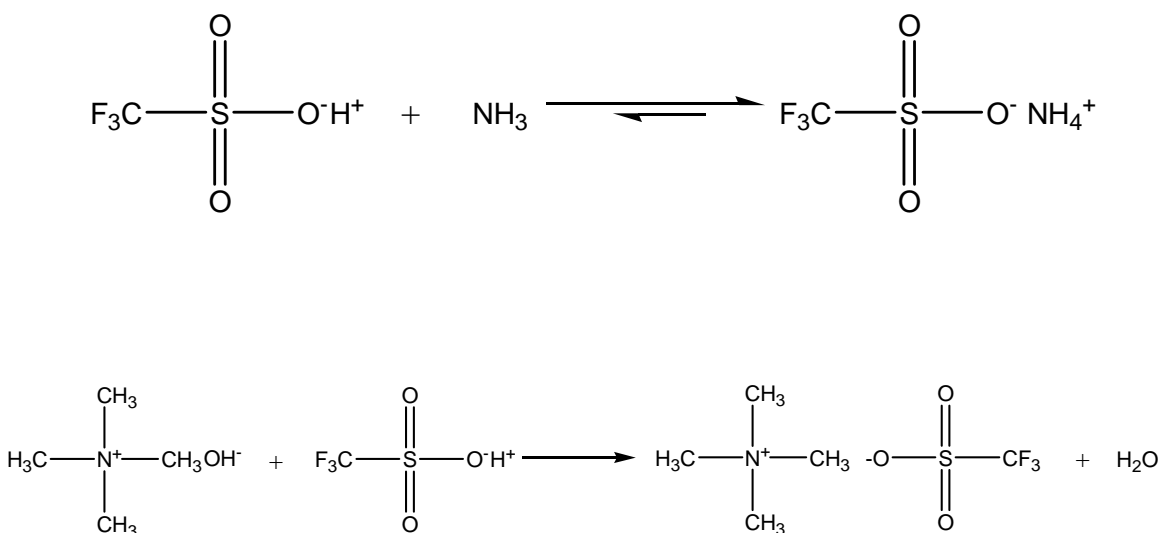


Figure 5.8 The difference between the reaction of an amine and an ionic base with an acid. Shown is the reaction of ammonia and TBAH with triflic acid.

5.3 CONCLUSIONS AND RECOMMENDATIONS

In order to study the role of acid/base neutralization byproducts in photoresist films, several salts were synthesized and tested for activity. Films of TBOC loaded with different salts were coated onto silicon wafers and then subjected to typical post exposure bake temperatures. These films were monitored with IR spectroscopy for any change.

Salts formed from the reaction of strong acids with amine bases were observed to deprotect the resist films without the presence of free acid. The time required for this deprotection in TBOC films, however, is much longer than the time required for free acid to deprotect the film. Salts of weak acids were not observed to cause any change in the film. This result is probably because the weak acids are not strong enough to initiate the photoresist deprotection reaction.

Salts of ionic bases were also not observed to initiate the deprotection of photoresist films. It was concluded that this result was likely caused by the fact that these salts cannot undergo the reverse reaction to regenerate acid without the presence of water. Also, it was observed that salts that had been synthesized or stored in the presence of water produced varying results. These results tend to indicate that water plays an important role in photoresist deprotection kinetics. At this point, no equipment suitable for studying photoresist deprotection kinetics under varying levels of humidity is available in the Willson group labs, but it is recommended that such equipment be acquired or constructed if further studies of photoresist deprotection kinetics are to be undertaken.

Photoresist films containing active salts were observed to initiate the deprotection of TBOC films, but this deprotection was extremely slow compared to deprotection initiated by free acid. Furthermore, the presence of salt did not seem to greatly influence the rate at which TBOC is deprotected by free acid. Because of these factors, it was concluded that although salts can be active in photoresist films, the time scale at which salts react with the photoresist is much slower than the time scale at which free acid is active. Because of this salts do not likely contribute significantly to the lithographic process. Although the neutralization byproducts of acid/base neutralization do not contribute significantly to deprotection kinetics, there is much more to learn about how

bases function in photoresists. Subsequent chapters will describe further research in this area.

5.4 EXPERIMENTAL

5.4.1 General Procedure for the Synthesis of Triflate Salts

Although there are other alternatives, it was decided to synthesize salts by the most direct and simple method possible. Acid plus base yields salt. The tricky part of this synthesis is to find an unreactive solvent that will dissolve the base but not the salt. In each case a ten percent molar excess of base dissolved in a predetermined amount of dry solvent. The solution was then placed in a glove bag. A dewar with liquid nitrogen was also placed in the glove bag to cool the reaction as necessary. The experimenter used 5 gram ampules of triflic acid. The ampules were placed into the glove bag and cracked open. The correct volume of acid was slowly pipetted into the solution. As the acid was added, the experimenter observed the formation of a precipitate. The solution was removed from the glove bag and filtered through a fritted filter. The precipitate was washed several times with dry solvent to ensure that excess base was washed out of the solution. The salt was then dried under a 60 mTorr vacuum for several hours. The salts, when exposed to atmosphere, began to look wet after a few days, and were therefore considered to be hygroscopic and were stored under nitrogen or argon. Specifics to each salt synthesis are found below.

5.4.2 Purity Analysis

The purity of the salts that were synthesized was examined with ^1H -NMR to determine if unreacted base was present in the purified salt. It was observed by

comparison of the NMR of imidazole to the NMR of imidazolium triflate that the peaks of the salt's NMR were shifted significantly to the left. This shift provided a convenient way to differentiate between the base and the salt. In no case was unreacted base observed by NMR. Furthermore, IR spectra were taken of all the salts. In every salt, a large broad peak was observed in the 3400 inverse centimeter range. This peak could correspond to the amine in the salt or it could indicate the absorption of water. Because this peak was also seen in potassium triflate, it was concluded that it could very well correspond to water absorbed into the salt and was therefore considered further evidence that the salts are hygroscopic. Because of this result care was taken to ensure that salts were kept in humidity free environments from the time of synthesis to the time of use.

5.4.3 Infrared Spectroscopy (IR)

Infrared spectroscopy is carried out on a Nicolet Magna-IR Spectrometer under a nitrogen purge. For these experiments a left arm extension is used to analyze silicon chips placed on a hot plate. The spectrometer is controlled using Omnic software. Solutions were made by adding the desired amount of salt, base, or PAG to a stock solution of 15 weight percent TBOC in propylene glycol methyl ether acetate (PGMEA). Approximately one inch square aluminum-backed silicon wafer fragments were spin coated with four drops of the desired solution at (2500 rpm for 30 seconds). No post apply bake was performed because the temperature of the bake would be high enough to initiate deprotection in wafers that contain salt.

Data are collected by allowing the IR to begin scanning and then quickly placing the wafer in the beam path of the IR on a heated stage. The wafer quickly reaches temperature and begins to bake. The resulting series of IR spectra are then analyzed by

integrating the area under the carbonyl peak at 1750 cm^{-1} . The data are normalized by dividing by the starting area under the carbonyl peak.

5.4.4 Specific Salt Synthesis Information

Imidazolium triflate

In a 100mL round bottom flask, 2.26 grams of imidazole were added to 50mL of dichloromethane (DCM). Next, 5 grams of triflic acid were added to the mixture dropwise. The mixture was filtered, and the precipitate was washed several times with dry DCM. The product was dried under vacuum. Yield: 84% of white powder. MP: $198\text{-}201^{\circ}\text{C}$ $^1\text{H-NMR}$ (D_2O ,): 7.32 (d, 2H, 0.01Hz), 8.53 (s, 1H) FTIR (KBr, cm^{-1}): 3139 (s), 3008 (m), 2875 (w), 2749 (w), 2633 (w), 1642 (w), 1587 (m), 1448 (w), 1254 (s), 1166 (s), 1097 (s), 1053 (m), 1033 (s), 823 (m), 771 (m), 646 (s), 579 (m), 516 (m)

Pyridinium triflate

In a 100mL round bottom flask, 1.4 grams of pyridine were added to 50mL of DCM. Next, 2.5 grams of triflic acid was added to the mixture dropwise. The mixture was filtered, and the precipitate was washed several times with dry DCM. The product was dried under vacuum. Yield: 44 % of white powder. MP: $232\text{-}235^{\circ}\text{C}$. $^1\text{H-NMR}$ (D_2O ,): 7.95 (t, 2H, 0.03Hz), 8.50 (t, 1H, 0.01 Hz), 8.65 (d, 2H, 0.02 Hz). FTIR (KBr, cm^{-1}): 3452 (w), 3240 (m), 3177 (m), 3142 (m), 3116 (m), 3085 (m) 2963 (m), 2912 (m), 1636 (m), 1610 (m), 1540 (m), 1489 (m), 1266 (s), 1159 (s), 1092 (m), 1031 (s), 900 (w), 802 (m), 759 (m), 684 (m), 644 (m), 576 (m), 519 (m)

Tributylamonium triflate

In a 100mL round bottom flask, 4.3 grams of tributylamine were added to 50mL of DCM. Next, 3.2 grams of triflic acid added to the mixture dropwise. A precipitate was formed, but once filtered the precipitate had a brown color, possibly from the base. The solid was dissolved in water and then precipitated into hexane. The resulting white solid was washed repeatedly with dry DCM and then dried under vacuum to obtain white solid. Yield: 25 % of white powder. MP: 130-132 °C. ¹H-NMR (D₂O,): .806 (t, 9H, 0.03 Hz), 1.28 (m, 6H, 0.02 Hz), 1.55 (m, 6H, 0.02 Hz), 3.00 (t, 6H, 0.01 Hz). FT-IR (KBr, cm⁻¹): 3433 (w), 3055 (m), 2966 (s), 2939 (m), 2879 (m), 2816 (w), 1471 (m), 1384 (w), 1289 (s), 1239 (s), 1161 (s), 1031 (s), 928 (w), 749 (w), 640 (s), 576 (w), 516 (w)

Potassium triflate

In a 100mL round bottom flask, 1.03 grams of potassium hydroxide were added to 50mL of Methanol. Next, 2.5 grams of triflic acid were added to the mixture dropwise. Only small amounts of precipitate were observed. The precipitate was filtered out and then washed repeatedly with dry methanol. The resulting solid was a fine powder, which was dried under vacuum. Yield: 5 % of white powder. MP: 242-244 °C. ¹H-NMR (D₂O,): No Hydrogens. FTIR (KBr, cm⁻¹): 3479 (w), 2365 (w), 1624 (w), 1273 (s), 1179 (s), 1034 (s), 768 (w), 651 (w), 580 (m), 520 (m)

Diisopropylamonium triflate

In a 100mL round bottom flask, 1.85 grams of diisopropylamine were added to 50mL of hexane. Next, 2.5 grams of triflic acid were added to the mixture dropwise.

Upon filtration, large chunks of precipitate were collected. These chunks were broken up by stirring them in hexane and refiltering them. The resulting solid was dried under vacuum. The solid was then allowed to stir in DCM for several minutes, and the mixture was filtered again to obtain a fine powder. The product was dried under vacuum. Yield: 76 % of white powder. MP: 158-161 °C. ¹H-NMR (D₂O, δ): 1.74 (d, 12H, 0.02), 3.38 (m, 2H, 0.02 Hz). FTIR (KBr, cm⁻¹): 3130 (m), 2992 (w), 2875 (w), 1603 (w), 1475 (m), 1453 (m), 1405 (m), 1291 (s), 1240 (s), 1165 (s), 1099 (m), 1035 (s), 641 (s), 518 (w)

Morpholinium triflate

In a 100mL round bottom flask, 3.2 grams of morpholine were added to 50mL of hexane. Next, 5 grams of triflic acid were added to the mixture dropwise. The precipitate was collected by filtration. The impure precipitate was placed in DCM and stirred for several minutes. The resulting filtrate was a fine powder, which was dried under vacuum. Yield: 34 % of white powder. MP: 108-110 °C. ¹H-NMR (D₂O, δ): 3.17 (t, 4H, 0.02 Hz), 3.83 (t, 4H, 0.02Hz). FTIR (KBr, cm⁻¹): 3421 (m), 3284 (m), 3048 (m), 2868 (m), 2816 (m), 2442 (w), 1634 (m), 1560 (m), 1455 (m), 1432 (m), 1250 (s), 1174 (s), 1103 (s), 1031 (s), 897 (m), 871 (s), 640 (s), 578 (m), 519 (m)

Chapter 6: The Influence of Base on Bias

6.1 INTRODUCTION

In photolithography, the trend is always towards smaller features. This continuous reduction in feature size is also associated with a reduction in allowable line-edge roughness.⁶³ Meeting these tight controls requires an ever expanding understanding of photoresists behavior and performance. One of the most powerful “knobs” available for a photoresist formulator to influence chemically amplified resist performance is the addition of small amounts of base additives. These base quenchers have been observed to influence imaging properties such as line-edge roughness, contrast, iso-nested bias, isofocal bias, resistance to airborne and substrate base contamination, and more; however, there are few systematic studies in literature describing how base type and loading affects imaging performance. To name a few examples of recent work in the area of base quenchers, researchers at IBM have developed a reaction diffusion model for photoresists that contain base quenchers,^{64,65} as have researchers from Hitachi.^{66,67} These models have been applied to understanding the role of bases in image blur and bias in chemically amplified photoresists. As people continue to investigate quencher effects in photoresists, increasing levels of complexity begin to surface, and the need for further study becomes apparent.⁶⁸ This chapter describes from both a theoretical and experimental perspective the influence of base on photoresist diffusion bias.

Isofocal CD (critical dimension) is another critical parameter for photoresists. An examination of aerial image intensity through focus will reveal a point on the aerial image at which the light intensity is the same regardless of focus. This point is known as the isofocal point. Figure 6.1 below shows a PROLITH simulation of aerial image intensity as a function of horizontal position for four arbitrary focus values. This

simulation is for 160nm lines at 320nm pitch. Notice that the isofocal point occurs at exactly half pitch. This is generally the case for nested lines. It is not always the case, however, that the actual features printed in photoresist will exhibit an isofocal CD at half pitch. In fact, printed isofocal CDs are not necessarily equal to the aerial image isofocal CD and can be either larger or smaller depending on the resist type. Understanding exactly what controls this shift, or bias, in isofocal CD is critical to logical resist design. Semiconductor manufacturers would clearly like to be able to print the critical dimension at the isofocal condition. This condition gives the maximum depth of focus and correspondingly the biggest process window. Researchers have determined isofocal CD to be a function of develop parameters, resolution, and bake conditions.⁶⁹⁻⁷²

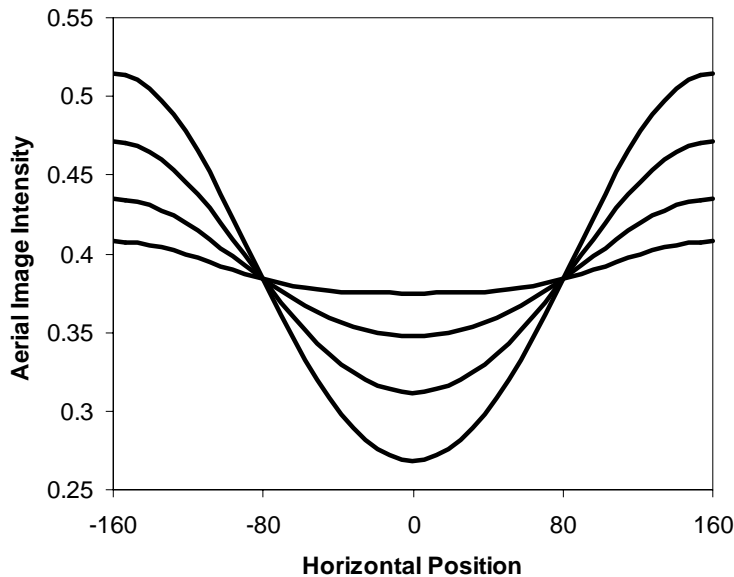


Figure 6.1 Aerial image isofocal point for 160nm nested lines at 320nm pitch. Shown is aerial image intensity versus horizontal position for four arbitrary focus values. The point where all four lines cross is the isofocal point. Notice the isofocal point is at half the pitch.

6.2 EXPERIMENTAL

6.2.1 Materials

An electronics grade, ESCAP-type terpolymer consisting of 60% hydroxystyrene, 23% t-butyl methacrylate, and 17% styrene, donated by DuPont Electronic Polymers, was dissolved in propylene glycol methyl ether acetate (PGMEA) to create a stock polymer solution. The weight-averaged molecular weight of the polymer was 12,300. Three photoacid generators (PAGs) were used to formulate stock solutions. These PAGs were triphenylsulfonium perfluoro-1-butanesulfonate (TPS-nonaflate), donated by AZ Clariant Corporation, bis(4-*tert*-butylphenyl)iodonium perfluoro-1-octanesulfonate (DTBPIPFOS), purchased from Daychem Corporation, and triphenylsulfonium trifluoromethanesulfonate (TPS-triflate), synthesized in our lab via standard techniques. Eight bases were purchased from Aldrich Company and were likewise diluted in PGMEA. These included trihexylamine (THA), trioctylamine (TOA), tridecylamine (TDA), tridodecylamine (TDDA), 1-piperidineethanol (1PE), 3-piperidino-1,2-propanediol (3PPD), triethanolamine (TEA), and a 1.0N solution of tetrabutylammoniumhydroxide in methanol (TBAH). All chemicals were used as delivered without further purification.

6.2.2 Formulation Strategy

Stock solutions of the polymer and PAG were diluted to 10% by weight. Stock solutions of bases were diluted to 2% by weight. PAG solution was added to portions of the polymer stock solution. When different PAG types were used, the ratio of moles PAG to grams polymer was kept constant. Base percentages were measured relative to molar amounts of PAG. After all solutions were formulated, additional quantities of

solvent were added to each formulation to give them a constant polymer to solvent ratio. This procedure ensured that all solutions would spin coat to the same thickness at a constant spin speed.

6.2.3 Contrast Studies

Ten resist formulations were created for contrast experiments. TPS-nonaflate at a loading of 2.8% by weight was used as the PAG in all ten solutions. The first solution contained no base, while the other nine solutions contained TOA, TBAH, and TEA at concentrations of 5%, 10%, and 20% relative to the PAG. All experiments were performed at International SEMATECH. Wafers were coated, post apply baked (PAB), and developed on a FSI Polaris 2000. Wafers were exposed on a 248nm SVG Microscan III, using conventional illumination ($NA = 0.6$, $\sigma = 0.6$), and the post exposure bake (PEB) was performed on an in-line track. Both the PAB and PEB were 60s at 130°C. A 60 second develop step was performed using SHIPLEY CD26, a 0.26N, surfactant-free, aqueous TMAH developer. All resists were coated over 59.5nm of Brewer Science DUV 30J, an antireflective coating. Resist formulations gave a coated thickness of 330nm. Open frame exposures were performed in a serpentine pattern across 62 locations on the wafer. Doses started at 2 mJ/cm² and increased to 52mJ/cm². Dose increments were 1/2 mJ/cm² for the first 20 steps, and 1 mJ/cm² for the remainder. Both the as-coated and after-PEB resist thickness were measured at all 62 sites with a Rudolph S300 ellipsometer. The change in thickness was normalized to go from 1 to 0 by dividing thickness change by the maximum thickness change of the resist after the deprotection reaction has reached its maximum extent. Thickness loss was assumed to vary linearly with the extent of deprotection of the resist, and hence, was used as a measure of the extent of deprotection of the resist.⁷³

6.2.4 Imaging Experiments

The majority of focus exposure matrices (FEMs) for this study were shot at AMD using a Cannon ES4 stepper. Conventional illumination with a numerical aperture of 0.8 and a partial coherence of 0.8 was used. A binary mask was employed for all of the studies, and the features of interest were 160nm nested lines at 320nm pitch. Twenty-one dose steps and fifteen focus steps were used. FEMs were centered on the dose-to-size and best focus, and appropriately sized dose and focus steps were employed to generate Bossung plots. The previously mentioned ten solutions plus several additional solutions were tested in this manner. Four new solutions were formulated with the same 2.8% by weight of TPS-nonaflate as used previously. Each solution contained 10% base relative to PAG. The four base types used, one in each of the four solutions were 1PE, 3PPD, THA, and TDDA. In addition, two solutions were made with a 10% loading of TOA, but varying PAG types. One solution contained TPS-triflate, while the other had DTBPIPFOS. These solutions were formulated to contain the same number of moles of acid as in the TPS-nonaflate solutions previously described. These resists were coated on 62nm of Shipley AR40 BARC. Resists were coated to a thickness of 338nm. The PAB conditions were 130°C for 60s, and unless otherwise noted, the PEB conditions were the same. Develop time was 60s in Shipley CD26.

A final set of FEMs was shot at International SEMATECH on the SVG Microscan III. The processing conditions for the SEMATECH wafers were as described above in the contrast subsection. Formulations in this case contained a higher absolute loading of acid and base. These formulations contained a loading of 6% by weight TPS-nonaflate, or an equivalent molar loading of one of the other PAGs. With the TPS-nonaflate PAG, base loadings of 5%, 10%, 25%, and 40% of TOA were used. Additionally, formulations with 40% loadings of THA, TDA, and TDDA were prepared.

Finally, for all three PAG types, 40% loadings of the largest and smallest alkyl amines available, TDDA and THA respectively, were shot. The feature size of interest in this case was 180nm nested lines at 360nm pitch. At SEMATECH, nine focus and nine dose steps were used for the FEMs, centered at best focus and dose to size.

All of the wafers printed in this study were analyzed by CD SEM. An Applied Materials NanoSEM 3D was used at both AMD and at SEMATECH to take SEM images of the features of interest on the wafers. At AMD, Scanning Electron Microscope images (SEMs) were acquired at three different positions along the bank of nested lines. Each SEM image contained three lines. Hence, a total of nine measurements were acquired for each field on each wafer. At SEMATECH, because of time constraints, only one image was taken of the bank of three lines at each processing condition.

6.2.5 Data Analysis

Data analysis was performed on the SEMs using a software package called SuMMIT written by Patrick Naulleau at the Center for X-ray Optics, Lawrence Berkeley National Lab. This software allowed the automation of the analysis of over 25,000 SEMs collected in this study. SuMMIT measures CD and LER for each line. The edge detection algorithm was held constant for every SEM analyzed. No filtering algorithm was applied to the data. The CD data was fed into ProDATA, provided to us by KLA-Tencor Corporation. ProDATA was used to generate Bossung plots from the data and to determine isofocal doses and isofocal CDs for each resist formulation.

6.2.6 Error Analysis

Throughout this chapter and the next, numerous experimental results for isofocal CD, LER, and contrast are presented, and it is important to consider the error associated with each of these measurements. Conducting a full error analysis for all the experiments performed is a difficult undertaking, and in order to properly quantify experimental error, multiple wafers would have to be imaged and analyzed to determine a standard deviation for each measurement. The equipment needed to print wafers; however, is expensive, production quality equipment located at AMD and at International SEMATECH. Both of these companies were extremely kind to allow university experiments to be performed on their tools, but because of high demand for the tools, access was limited. As a result, a full set of repeats could not be performed, and consequently, a full error analysis could not be conducted. Best estimates of experimental error based on experimental protocol and the limited number of repeats that could be performed are listed as follows: LER could be measured to within one nanometer, isofocal CD could be measured to within eight nanometers, and contrast could be measured to within ten percent. These values should be kept in mind for all results presented throughout the remainder of this chapter and the next.

6.3 RESULTS

Simulations were run with PROLITH, and experimental data was collected to understand shifts in the isofocal CD from the aerial image isofocal point, located at half the pitch.

6.3.1 Simulation Results

The goal of this set of simulations was to understand shifts in the isofocal CD caused by the addition of base quenchers. Preliminary results from PROLITH indicated that large shifts in the isofocal CD could be achieved by varying acid and base diffusion coefficients. To further investigate this phenomenon, a series of PROLITH simulations were conducted in which the acid and base diffusion coefficients were varied. Base loadings were also varied, although PAG loadings and all other simulation parameters were fixed. It was seen in these simulations that the difference between the diffusion lengths of the photoacid and the base quencher was the dominant parameter controlling shifts in the isofocal position. Simulation indicates that photoresist formulations with low levels of base quencher have only minor shifting of the isofocal position when acid and base diffusion lengths are varied. As the relative base loading is increased, however, the shift in the isofocal position becomes more pronounced. For long acid diffusion lengths (relative to base diffusion lengths), the isofocal CD was observed to shift to smaller values. The opposite was true when base diffusion lengths were greater than acid diffusion lengths. Figure 6.2 below summarizes these trends. Linear fits were applied to the simulation data to demonstrate the trends.

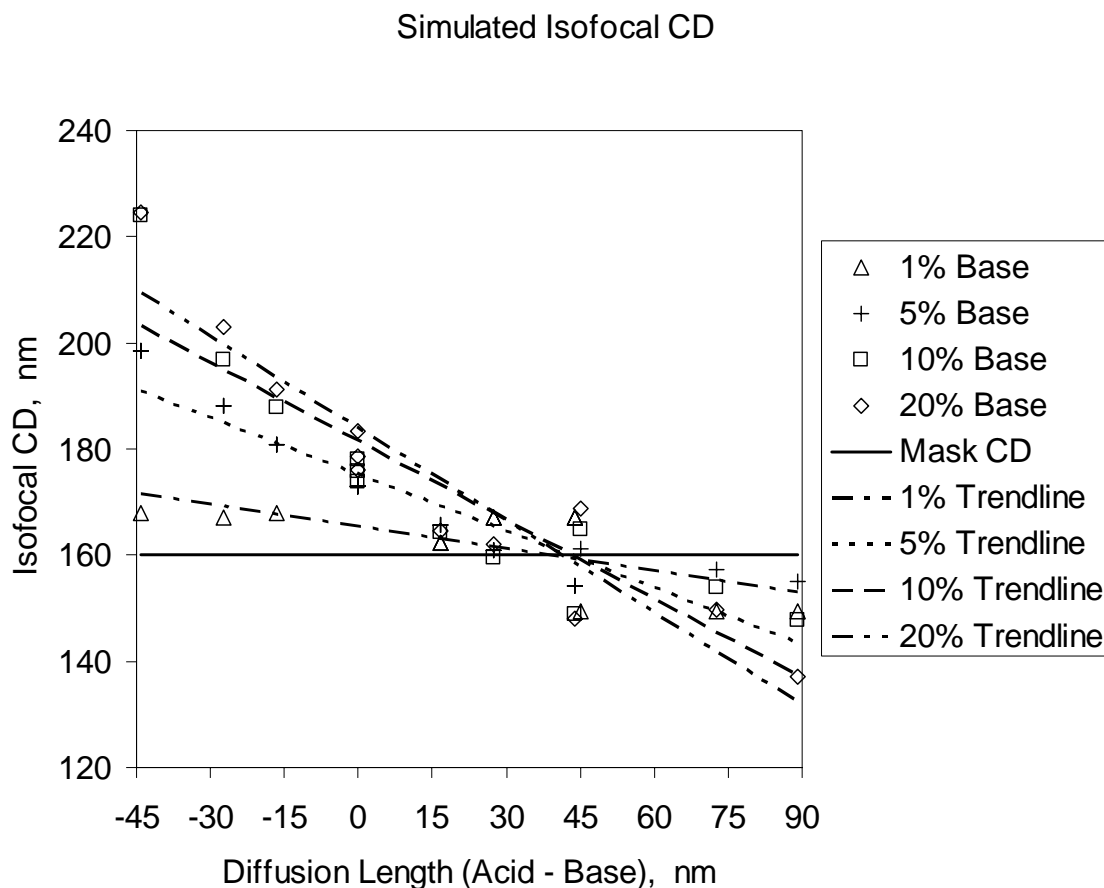


Figure 6.2 Summary of the results of PROLITH simulations. In general, acid diffusion lengths greater than base diffusion lengths result in a downward shift in the isofocal CD. The opposite is true for acid diffusion lengths smaller than base diffusion lengths. Also, shifts in the isofocal CD tend to become more pronounced at higher base loadings.

6.3.2 Experimental Results

It is known from simple diffusion theory that the diffusion coefficient of a small molecule penetrant through a medium is related to the size of the penetrant unless other interactions are present. Because simulation predicts that varying acid and base diffusion

coefficients within a photoresist film will influence the isofocal position, acids and bases of varying molecular volume were chosen to investigate the phenomenon. Data were collected and analyzed to generate Bossung plots, from which the isofocal condition was determined by ProDATA. The data from all of the formulations are summarized below in Table 6.1. Note that each data point is the average of measurements at three different positions.

Table 6.1 Experimental Results for isofocal CD studies (nominal mask CD = 160 nm)

PAG	Base	Base Loading, rel. to PAG	Isofocal CD, (nm)	Dose to Size, (mJ/cm²)
TPS-nonaflate	None	N/A	144	27
TPS-nonaflate	TOA	5%	153	63
TPS-nonaflate	TOA	10%	157	102
TPS-nonaflate	TOA	20%	152	180
TPS-nonaflate	TEA	5%	159	61
TPS-nonaflate	TEA	10%	163	99
TPS-nonaflate	TEA	20%	167	180
TPS-nonaflate	TBAH	5%	157	69
TPS-nonaflate	TBAH	10%	151	111
TPS-nonaflate	TBAH	20%	149	200
TPS-nonaflate	TDDA	10%	158	102
TPS-nonaflate	THA	10%	156	206
TPS-nonaflate	1PE	10%	161	99
TPS-nonaflate	3PPD	10%	155	102
TPS-triflate	TOA	10%	73	95
DTBPIPFOS	TOA	10%	182	66

These results show a large shift in isofocal CD with varying acid type (73nm - 182nm), but they do not show a large shift in isofocal CD with varying base type or concentration (152nm – 167nm), although the wafer with TPS-nonaflate and no base shows an isofocal CD of about 10nm smaller than any other wafer containing TPS-

nonaflate and base. In an effort to increase the magnitude of the shift, additional data was taken on a different set of formulations. In this set, absolute acid and base loadings were increased based on simulation results that suggest that doing so would potentially amplify any shifts that were occurring. Furthermore, only trialkyl amines were considered as bases in this study to ensure that other variables such as hydrogen bonding between the base and the polymer did not confound the results. Finally, bases with the most extreme difference in size were shot with all three PAG types. This experiment was designed to capture the maximum possible shift in isofocal CD obtainable with the materials available. The data from these experiments are shown in Table 6.2 below. Results were similar to those reported in the first trial.

Table 6.2 Experimental results for the second round of isofocal CD studies (nominal mask CD = 180nm)

PAG	Base	Base Loading, rel. to PAG	Isofocal CD, (nm)	Dose to Size, (mJ/cm²)
TPS-triflate	TDDA	40%	111	53
TPS-triflate	THA	40%	122	49
TPS-nonaflate	TDDA	40%	158	55
TPS-nonaflate	THA	40%	167	53
DTBPIPFOS	TDDA	40%	214	30
DTBPIPFOS	THA	40%	224	27
TPS-nonaflate	TOA	5%	178	9
TPS-nonaflate	TOA	10%	179	15
TPS-nonaflate	TOA	25%	166	33
TPS-nonaflate	TOA	40%	176	54
TPS-nonaflate	TDA	40%	179	50

6.3.3 193nm Photoresist Results

Photoresist bias was examined in a 193nm photoresist as well, and an interesting trend was observed. The iso-fading CD, analogous to the iso-focal CD, was observed to shift as a function of base loading. Figure 6.3 shows this result. For specifics on the materials and apparatus used to conduct this experiment, please refer to the experimental section of Chapter Seven. This result is significant because for the first time the addition of base was observed to cause a significant shift in the iso-fading CD.

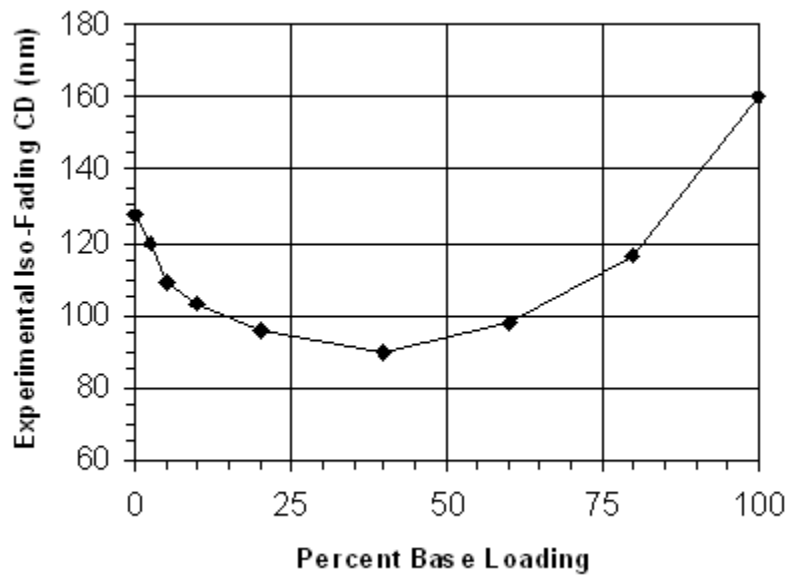


Figure 6.3 Observed iso-fading CD through base loading

6.4 DISCUSSION

6.4.1 Simulation Results

As described previously, simulation suggests that the difference between the acid and base diffusion coefficients is a good predictor of isofocal shift direction. Also, simulation predicts that at low base concentrations this shift will not be large, but at higher base concentrations, the shift magnitude will increase. At some level, these trends can be explained by fairly simple arguments. When no base is present in a photoresist film, the acid profile generated for nested lines looks very similar to the deposited aerial image. As base levels are increased slightly, some of the acid and all the base are consumed, which shifts the acid profile to lower concentration values but does not affect the shape of the acid profile. Eventually, with the addition of sufficient base, all of the acid will be consumed in the nominally unexposed regions. This process will create a region containing acid adjacent to a region containing base. A schematic of both of these cases is shown below in Figure 6.4. In the latter case, if the acid and the base are then allowed to diffuse, the faster diffusing species will spread into the regions occupied by the slower diffusing species. If base were to diffuse into the nominally exposed regions and quench the acid there, the lines in resist would print larger; however, if the acid diffused outwards from the exposed regions, line widths would be decreased. This simple idea explains the results of the PROLITH simulations presented earlier.

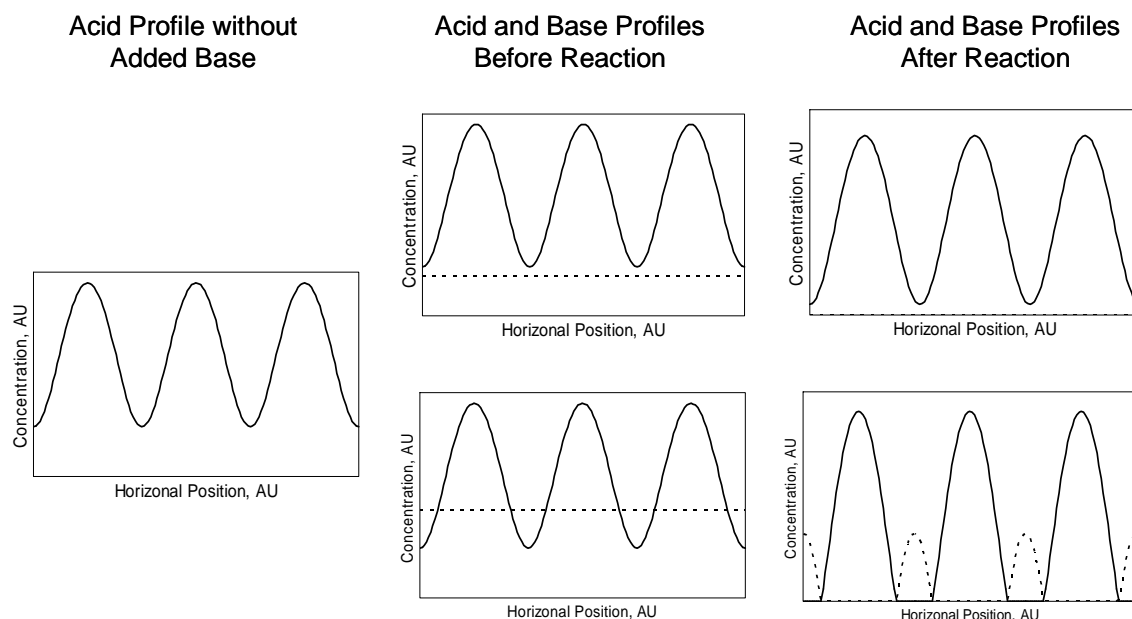


Figure 6.4 Illustration showing how the addition of various levels of base quencher can lead to different types of acid and base profiles in a photoresist film. The solid lines represent acid, and the dotted lines represent base

6.4.2 Experimental Results

Three general types of experiments were conducted: varying the acid type at a constant base type and loading, varying the base type at constant acid type and loading, and varying the base loading for constant acid and base type. Experiments were conducted both at AMD and International SEMATECH using different imaging conditions. Of these studies, the one that showed the largest effect on isofocal position was varying the acid type. Simulation predicts that all things being equal, faster diffusing acids lead to smaller isofocal CD and faster diffusing base leads to larger isofocal CD. The diffusion coefficients for these acids in this particular polymer are unknown, so in order to qualitatively determine if the experimental data followed predicted trends, some relation between acid diffusion coefficient and a known parameter is required. The

simplest possible predictor of diffusion coefficient is the Stokes-Einstein equation for diffusion of a small molecule through a liquid.⁷⁴ Although not strictly valid for polymer systems, it does provide some framework from which statements about the relative difference in diffusion coefficient of like molecules can be made. Equation 6.1 shows this relationship:

$$\frac{D_{AB}\mu_B}{kT} = \frac{1}{6\pi R_A}, \quad (6.1)$$

where D_{AB} is the diffusion coefficient, μ_B is the viscosity of the medium, k is Boltzmann's constant, T is temperature, and R_A is the radius of the diffusing molecule. This equation states that in the simplest possible case, diffusion coefficient is proportional to molecular radius, a quantity that can be easily simulated. Such simulations were carried out using a program called Spartan '02. Molecular radii were calculated from molecular volumes by assuming a spherical molecule. Diffusion length was related to diffusion coefficient by the standard one dimensional expression $D=L^2/2t$, where D is diffusion coefficient, L is diffusion length, and t is PEB time. Using these quantities, Figure 6.5 below was created to examine the correlation of isofocal CD with the estimated acid diffusion length.

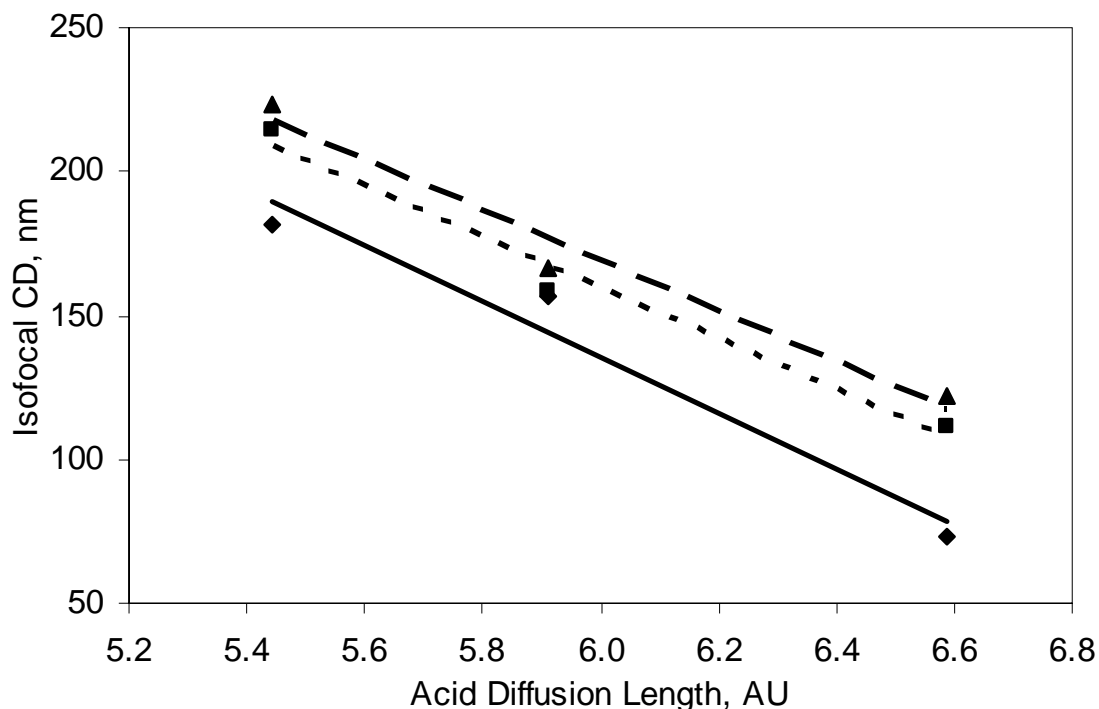


Figure 6.5 Correlation between estimated acid diffusion lengths in arbitrary units with isofocal CD measured by experiment. Diamonds with a solid line are 160nm nominal mask features in a resist containing 10% TOA. Squares with a dotted line are 180nm nominal mask features in a resist containing 40% TDDA, and triangles with a dashed line are 180nm nominal mask features in a resist containing 40% THA. The trend shown matches the trend seen in simulation.

Isofocal CD was observed to vary as predicted by simulation at a fixed base loading. Contrary to simulation, however, results of the studies in which base type and loading were varied show far less shift in isofocal CD than was observed in the acid studies. In fact, all observed shifts in the isofocal CD for these cases were well within the margin of error for determining isofocal CD, and no trends could be ascertained. This result was contrary to expectation because simulation predicts that the difference between acid and base diffusion coefficients is the critical parameter that influences isofocal

shifts. Based on simulation, one would predict that isofocal CD should shift as much based on changes in base diffusion coefficient as it would based on changes in acid diffusion, assuming the diffusion coefficients of both species are of the same order of magnitude. It is possible that little shift in the isofocal CD was observed because the magnitudes of the base diffusion coefficients are much smaller than those of the acids.

Although the 193nm resist was not part of this study originally, results from this case were included because they were markedly different than those obtained with the 248nm resist. These results were also different than those predicted by simulation, although this is somewhat to be expected because PROLITH simulation parameters were determined by matching PROLITH output to experimental data from the 248nm resist. Results from the 193nm resist indicate that iso-fading CD in this system can in fact be tuned by the addition of base. Although multiple base types were not considered in this study, by adjusting the base loading in this resist, iso-fading CD was observed to first decrease and then increase as base was added to the resist. In the case of 248nm resists, neither changing base type nor changing base loading was observed to cause a shift in isofocal CD.

PROLITH simulations did indicate that adjusting base loading should cause a shift in iso-fading CD, but no change in the direction of the shift was predicted. This disagreement was probably caused because concentrations of base higher than 20% were not simulated due to the fact that 20% was the highest base loading in the original study. Furthermore, the simulation was specifically tuned to the 248nm resist and hence some disagreement between the 193nm and 248nm cases should be expected.

Although the specific reason for the initial decrease followed by an increase in measured CD is not fully understood at this time, one possible explanation for this trend may be enhanced transport facilitated by the addition of base. Another possible

explanation can be found in the theory that shifts in photoresist bias may be tied to acid and base diffusion in the resist.⁷⁵⁻⁷⁸ According to these theories, as acid diffusion occurs, it can “push” the iso-fading CD towards smaller values of CD. Conversely, base diffusion is thought to push the iso-fading CD in the opposite direction. Furthermore, no shift in the iso-fading position is predicted at low levels of base. One possible explanation for this trend may be that by adding base initially, the iso-fading position is able to shift to lower CD because of acid diffusion. Then, as base loading is further increased, the amount of acid in the nominally exposed regions remains roughly the same (imagine a threshold acid concentration required to deprotect the photoresist polymer), but the amount of base in the nominally unexposed regions is increased. Eventually the amount of base in the dark region might become large enough to limit acid diffusion or perhaps even push the iso-fading CD towards higher values through base diffusion.

6.5 CONCLUSIONS AND RECOMMENDATIONS

Base type was not observed to have a strong influence on imaging performance of 248nm resists in these studies although PROLITH simulations predict differently. Three general types of bases were used in these studies, trialkyl amines, hydroxyl containing (hydrogen bonding) amines, and TBAH (ionic rather than amine). Varying the size of the base was expected to cause variations in the diffusion coefficient of the base, which would in turn lead to shifts in the isofocal CD. Such shifts were not observed, although it is possible that such shifts were occurring but their magnitude was below the experimental error associated with this study. One reason for the discrepancy between experiment and simulation could be that base diffuses much more slowly in the photoresist film than acid. Another reason could be the influence of other parameters not accounted for in the simulation. Similar experiments in which acid type rather than base

type was varied were performed as well. In this case, a large shift in isofocal CD was observed with changing acid size. These shifts correlated well to shifts predicted by simulation.

A 193nm resist was also investigated. Contrary to the results observed with the 248nm resist, base loading was observed to influence bias. In this case, however, bias was observed to initially decrease and then increase again as base loading was increased. It is thought that this result might be caused because a fast diffusing base could be overwhelmed by a much larger amount of slower diffusing acid, but as base loading is increased, base diffusion would become more dominant. The fact that bias shifts at all tends to indicate that base diffusion in the 193nm system may be much greater than in the 248nm system.

Clearly additional studies are needed to fully understand bias in these systems. Future work should begin by independently measuring the diffusion coefficient of bases through photoresist films. One proposal by which this goal might be accomplished is to use a trilayer film stack similar to those used by researchers at UT to measure acid diffusion coefficients.⁷⁹ In this experiment, one would coat a polymer loaded with a high concentration of the diffusing species. Either the base itself could be used or for more control over the time at which diffusion begins, a photo-base generator could be used.^{80,81} The second layer of the film stack would be the photoresist polymer that diffusion is to be measured in. The final layer of the film stack should be a base sensitive detector layer that gives a measurable signal when heated in the presence of base. Such a polymer has recently been developed by researchers at UT. Imaging studies should also be continued. One study in particular that would be interesting is to see how the differing bases such as THA, TOA, and TDDA affect bias in the 193nm system. Also, variables such as

developer threshold, polymer type, and acid loading, which have not been previously considered, should be investigated as well.

Chapter 7: The Influence of Base on Line-Edge Roughness

This section describes experiments designed to determine how base influences photoresist contrast as well as line-edge roughness. The first portion of this chapter describes additional data collected from the experiments described in Chapter Six. The reader should refer to that chapter's experimental section for details on the experimental protocols. The second half of this chapter describes additional experiments that were conducted with a 193nm photoresist polymer to explore the link between photoresist contrast and line-edge roughness.

7.1 INTRODUCTION

7.1.1 Contrast

Photoresist contrast can be generally described as the ability of a photoresist to take an aerial image and to convert that image into a well-defined photoresist profile. Contrast can be thought of as having two distinct contributors: the chemical processes within a photoresist that create a gradient in photoresist deprotection based on the deposited aerial images and the developer/polymer interactions that act on that gradient to selectively remove areas of the photoresist that have been sufficiently deprotected. The developer interactions with the photoresist are not likely influenced significantly by small amounts of base within the film, but the base does affect the deprotection reaction in the photoresist film by reacting with the photogenerated acid. Mathematically, photoresist contrast can be defined as the log-slope of the development rate versus dose curve⁶ as shown in Equation 7.1 as follows:

$$\gamma = -\frac{\partial \ln R}{\partial \ln E} \quad (7.1)$$

where γ is photoresist contrast, R is development rate, and E is dose. This expression can be further broken down into a “developer” contrast and a “chemical” contrast. Equation 7.2 below shows this step as follows:

$$\gamma = -\frac{\partial \ln R}{\partial \ln E} = -\frac{\partial \ln R}{\partial F} \frac{\partial F}{\partial \ln E} \quad (7.2)$$

where F represents the relative blocking fraction of the photoresist. In this case, the derivative of development rate with blocking fraction, the developer contrast ($d \ln R / dF$), can be thought of as being independent of base concentration, while the gradient of blocking fraction with respect to aerial image intensity, the chemical contrast ($-dF / d \ln E$), is strongly dependent on base concentration.

7.1.2 Line-edge roughness

Line-edge roughness is another parameter important to lithographers that is strongly influenced by the addition of base. It is usually defined as the 3σ deviation of the position of the edge of a line in resist from the mean position of that edge. A number of people have looked at LER in recent years, and have found it to be a function of numerous variables such as substrate type, post apply bake, mask LER, aerial image quality, exposure dose, and PEB temperature.⁸² Excessive LER can lead to yield loss and poor transistor performance.⁸²⁻⁸⁶ Additionally, the relative impact of LER increases as feature sizes get smaller; hence, the magnitude of allowable LER in a photoresist is continually decreasing.⁸⁷ In recent years, researchers have examined LER as a function

of several process parameters,^{82,88-91} and work in this area is ongoing. Clearly it is important to understand the origins of LER and to develop methods to control it. Figure 7.1 below shows two SEM micrographs of lines in resist. Figure 7.1(a) shows lines in resist without base, and (b) shows lines of the same size printed in a resist formulation with base. It is easily seen that the addition of base to photoresist qualitatively improves LER. Subsequent sections describe how variables like base loading and base type influence this value.

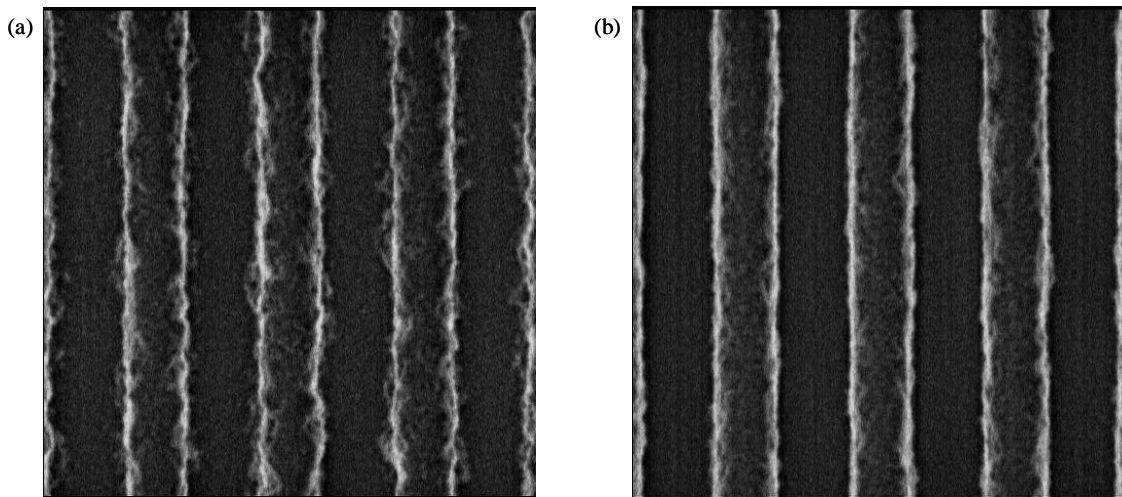


Figure 7.1 (a) Lines printed in a photoresist that does not contain base, (b) Lines printed in a photoresist that does contain base. The edges of the lines in (b) show less roughness than the edges in (a).

7.2 RESULTS

This section describes additional results obtained from the imaging studies described in Chapter 6. The goal of these experiments was to obtain a basic idea of how the addition of base influences imaging performance. Photoresist contrast and LER were investigated.

7.2.1 Contrast Studies

Open field exposures at different doses were performed on wafers coated with the ten different resist formulations described previously in Chapter 6. For each resist formulation, the difference between the thickness of the resist film after the post apply bake (PAB) and the thickness of the exposed resist film after the post exposure bake (PEB) was measured as a function of dose. These data have been normalized such that 1.0 represents a film that has not undergone any shrinkage whereas 0.0 represents a film that has undergone the maximum shrinkage. Maximum shrinkage was determined by the point at which increasing the dose did not cause additional film shrinkage. It was assumed that film shrinkage is proportional to the conversion of blocked polymer to unblocked polymer; hence, Figure 7.2 shows the data plotted as blocking fraction rather than thickness loss.⁷³

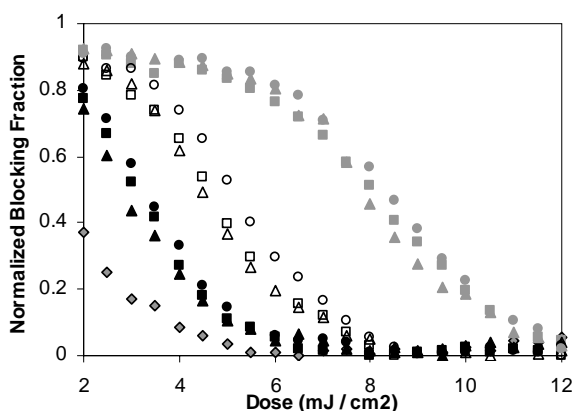


Figure 7.2 Percentage of blocked polymer sites that remain blocked after exposure and PEB for ten different photoresist formulations. The shape of the dots represents the type of base used. Diamonds represent the no base resist, triangles represent TEA, squares represent TOA and circles represent TBAH. The color of the points represents the base loading. Solid black points represent a molar loading of 5% relative to PAG, while hollow points represent a loading of 10%, and solid grey points represent a loading of 20%.

7.2.2 Line-Edge Roughness Studies

Line-edge roughness was also measured for all of the wafers shot in the first round of imaging experiments described above. Values quoted are LER at best focus and dose to size. LER values were measured on 18 line edges and averaged to give the value quoted. In addition to the studies described previously, the effect of PEB temperature on LER was investigated as well. In these studies, the temperature of the PEB was varied for two resists. One was the resist containing no base, and the other was the resist containing 10% TOA. Data from these studies are presented below in Table 7.1 and Table 7.2.

Table 7.1 LER as a function of base type and loading

PAG	Base	Base Loading	3σ LER, nm
TPS-nonaflate	None	N/A	16.3
TPS-nonaflate	TOA	5%	10.8
TPS-nonaflate	TOA	10%	8.2
TPS-nonaflate	TOA	20%	7.1
TPS-nonaflate	TEA	5%	10.6
TPS-nonaflate	TEA	10%	9.5
TPS-nonaflate	TEA	20%	7.2
TPS-nonaflate	TBAH	5%	10.1
TPS-nonaflate	TBAH	10%	8.6
TPS-nonaflate	TBAH	20%	7.3
TPS-nonaflate	TDDA	10%	8.8
TPS-nonaflate	THA	10%	7.6
TPS-nonaflate	1PE	10%	9.6
TPS-nonaflate	3PPD	10%	8.8
TPS-triflate	TOA	10%	10.6
DTBPIPFOS	TOA	10%	12.4

Table 7.2 LER as a function of PEB temperature for a resist without base and for a resist containing 10% TOA

Base	PEB Temperature, °C	3 σ LER, nm
10% TOA	130	8.2
10% TOA	120	9.6
10% TOA	110	9.9
10% TOA	105	8.5
10% TOA	100	9.1
None	135	14.5
None	130	15.6
None	120	13.7
None	110	11.0
None	105	9.1
None	100	10.7

7.3 DISCUSSION

7.3.1 Contrast Studies

A mathematical model for contrast was developed and fit to the thickness loss data presented previously. This model is based on the application of elementary kinetics to the expression for the chemical contrast described in Equation 7.1. Three reaction expressions, shown as Equations 7.2-7.5 below, were used for this model: the conversion of PAG into acid by exposure to light, the reaction of the acid with the polymer, and the neutralization of acid with base quencher. Rate expressions can be developed for each of these equations, and those expressions can then be solved to give blocking fraction as a function of exposure dose, which can then be further manipulated to give contrast as a function of exposure dose. The complete derivation of this solution is presented elsewhere.²⁸





These equations can be fit to experimental data using the three reaction rate constants, C , k_{amp} , and k_{quench} as fitting parameters. The results of this fit are shown in Figure 7.3 below, which shows normalized blocking fraction and chemical contrast as a function of dose. It should be noted that the same rate constants were used for every base concentration. The values for the fit parameters used were $C = 0.029 \text{ cm}^2/\text{mJ}\cdot\text{s}$, $k_{amp} = 0.36 \text{ s}^{-1}$ and $k_{quench} = 2.89 \text{ s}^{-1}$.

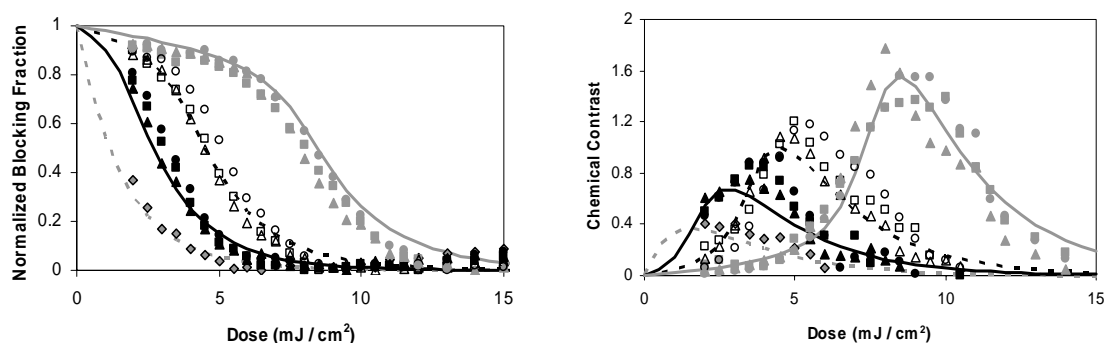


Figure 7.3 This figure shows a comparison of the model fit to experimental data for the contrast model presented. The shape of the dots represents the type of base used. Diamonds represent the no base resist, triangles represent TEA, squares represent TOA and circles represent TBAH. The color of the points represents the base loading. Solid black points represent a molar loading of 5% relative to PAG, while hollow points represent a loading of 10%, and solid grey points represent a loading of 20%. The model fits for the 0%, 5%, 10%, and 20% base loadings are shown by the dotted grey line, the solid black line, the dotted black line, and the solid grey line respectively.

The above figure shows good agreement between the experimental data and the model, so additional simulations were performed to understand not only the benefits of

adding base, but also shows some of the associated drawbacks, particularly decreased photospeed. Contrast enhancements and the photospeed of a resist were simulated for base loadings between 0 and 80%. Figure 7.4 shows the results of this simulation.

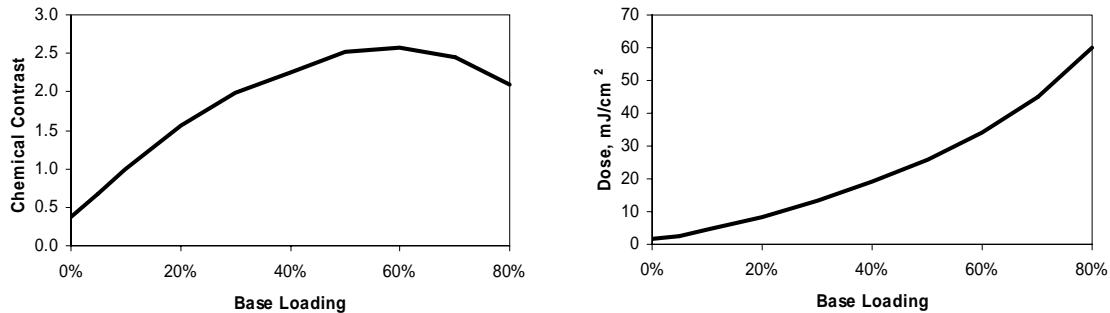


Figure 7.4 Simulation results showing the tradeoff between contrast enhancements and photospeed achieved by adding base

As can be seen, adding base to a photoresist formulation improves contrast, but marginal improvements in contrast diminish as the amount of base is increased. Eventually contrast reaches a maximum at high base loadings because the majority of the available photoacid has already been consumed. Photospeed, on the other hand, decreases with increasing base loading. This situation presents a tradeoff for semiconductor manufacturers. Obviously, contrast needs to be as high as possible, but low photospeeds can reduce exposure tool throughput. Because of this tradeoff, it is advisable to only add low amounts of base to resist formulations. This result has implications for the designers of the next generation of resists as well. The implication is that the addition of base quenchers to CARs to meet increasingly stringent LER and CD tolerances may not be a complete solution because of economic constraints on throughput.

7.3.2 Line-Edge Roughness

Line-edge roughness was measured as a function of acid type, base type, base loading, and PEB temperature. Of these variables, trends in LER could be seen with base loading and PEB temperature. Figure 7.5 below shows these results. Each point on the figure represents an average of measurements over 18 line edges.

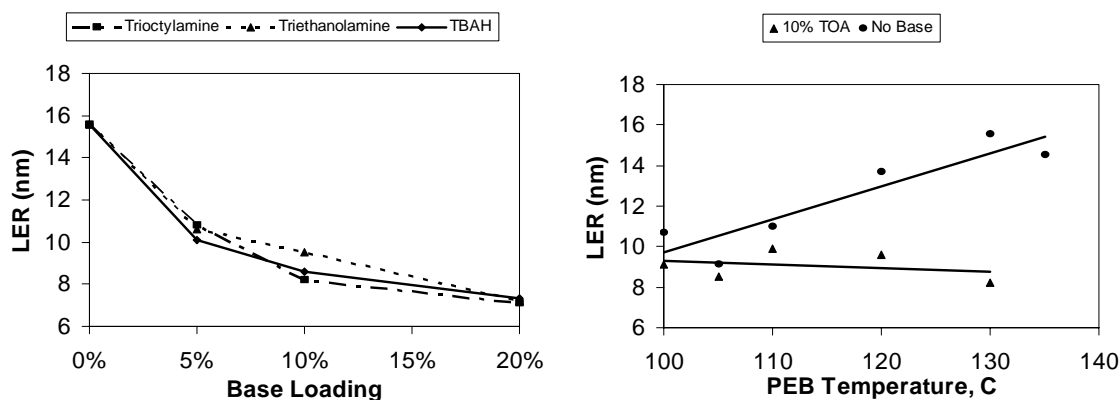


Figure 7.5 Observed trends of LER with base loading and PEB temperature

As can be seen, LER was observed to decrease with base loading for all resists studied. Furthermore, LER was observed to increase with PEB temperature for a resist without base. The addition of base to that resist was observed to eliminate that increase. Improvements in LER with the addition of base can be thought of as coming from two sources. The first source of improvement is the resist contrast enhancement as described earlier. This contrast enhancement improves LER by enhancing the chemical kinetics to create sharper acid latent images in resist. The second possible source of improvement in LER is from diffusion effects. If some component of LER can be attributed to stray acid molecules diffusing randomly into nominally unexposed regions, then the addition of base to the formulation should improve LER by capturing or “scavenging” stray molecules. The right side of Figure 7.5 lends support to this argument. It is possible that

LER is increasing with PEB temperature because of increasing acid diffusion at elevated temperatures for the resist without base. In the second resist that does contain base, the presence of base could be preventing the diffusion of acid molecules into nominally unexposed regions thus limiting the increase of LER.

7.4 A SECOND ROUND OF EXPERIMENTS

Now that an experimental protocol for measuring LER had been established, a model for photoresist contrast had been developed and tested, and a basic understanding of how base quenchers impact LER and photoresist contrast had been obtained, it was decided to conduct a second round of imaging studies to further investigate the role of base in photoresists. Results from the first round of experiments showed that both contrast and LER are improved by the addition of base to photoresists. It was not clear at this point, however, if these two improvements were related and if so, in what way. For example, simulation predicted a maximum in contrast at high base loading, but formulations used in those studies did not use high enough base loadings. As a result, it was unclear if LER would follow a similar trend.

A number of researchers have correlated measured LER with the quality of the aerial image used to generate the feature,^{75,77,92-98} and image-log slope (ILS) has been shown to be a good predictor of LER over a wide range of illumination conditions, feature sizes, pitches, and exposure doses.^{75,91} ILS is defined as the slope of the log of the aerial image intensity versus position curve. The question remains, however, as to how the initial distribution of photons from the aerial image comes to manifest itself as LER. There are many chemical processes in the resist that contribute to this LER, and learning to understand them is the key to understanding and controlling LER. This paper uses

these chemical processes to investigate the link between acid and base concentration, photoresist contrast, and LER in photoresists.

7.5 EXPERIMENTAL

7.5.1 Materials

A copolymer of 59% 2-methyl-acrylic acid 5-oxo-4-oxa-tricyclo[4.2.1.0^{3,7}]non-2-yl ester and 41% 2-methyl-acrylic acid 2-methyl adamantan-2-yl ester with a weight average molecular weight of 8,590 was synthesized via standard free radical polymerization techniques. This polymer was dissolved to 10% by weight in propylene glycol methyl ether acetate (PGMEA) to create a stock polymer solution. For simplicity, one photoacid generator (PAG) type and one base type were used throughout the study. The chosen PAG was triphenylsulfonium perfluoro-1-butanesulfonate (TPS-nonaflate), donated by AZ Clariant Corporation. The base used was trioctylamine (TOA), purchased from Aldrich Company. These compounds were likewise diluted in PGMEA to make stock solutions. Formulations were created by volumetrically dispensing predetermined amounts of each resist component's stock solution to create a formulation of the desired composition. Care was taken when making these resists to maintain the same ratio of solids to solvent for each formulation to ensure the different formulations would spin coat to the same thickness. A total of 9 formulations were made. Each photoresist contained 4% by weight of TPS-nonaflate. TOA was added at molar loadings of 0%, 2.5%, 5%, 10%, 20%, 40%, 60%, 80%, and 100% relative to PAG.

7.5.2 Measuring Deprotection Kinetics

Resist formulations were cast at a thickness of 220nm on top of films of AR40 organic antireflection coating that were 77nm thick using a TEL Act12 wafer track. The

PAB was at 130°C for 90s. Exposures were performed on an ASML XT:1250 ArF scanner with quasar illumination at a 30° blade angle, a numerical aperture of 0.68, and outer and inner sigma values of 0.75 and 0.45, respectively. For deprotection kinetics measurements, no reticle was used. Formulations with base loadings of 2.5%, 5%, 20%, 60%, and 80% were measured, but the 5% loading was not used because of an error with that wafer (possibly a thickness non-uniformity) that caused the data to come out incorrectly. Wafers were patterned using a dose meander of 45 sites, starting at a dose of 1.0mJ/cm², and adjusting the increment based on the level of quencher in each resist formulation. Wafers were processed through PEB at 130°C for 90s, but not developed. The film thickness in each of the exposed areas and at 4 unexposed locations on the wafer was measured using a Thermawave Optiprobe spectroscopic ellipsometer. The change in thickness was normalized from 1 to 0 by dividing thickness change by the maximum thickness change of the resist after the deprotection reaction has reached its maximum extent. Thickness loss was assumed to vary linearly with the extent of deprotection of the resist, and hence, was used as a measure of the extent of deprotection of the resist.⁷³

7.5.3 Imaging Experiments

Dose-asymmetric magnification matrices (DAMMs) were used to image the 193nm photoresists. DAMMs are similar to focus-exposure matrices, or FEMs, except that instead of changing focus, asymmetric magnification (AMag) error is adjusted to induce image blur. A description of the image fading technique used to characterize resist LER by asymmetric magnification error can be found in prior publications.^{75,77,99}

Printing experiments were performed on the same scanner and track following the same process conditions as described in the previous section for measuring deprotection kinetics. Fifteen steps in dose and thirteen steps in asymmetric magnification error were

performed. The exposure dose and the dose increment were adjusted for each resist formulation to capture a wide range of resist CDs on the wafer, typically placing the dose to size in the middle of the matrix. AMag error was applied in increments of 1ppm in a range from 0 to 12ppm on the scanner. Wafers were processed through development using CD26 developer for 60s, and removed from the track without a hard bake process.

7.5.4 Data Collection and Analysis

All of the wafers printed in this study were analyzed by an Applied Materials VeritySEM CD SEM. The field of view was set to 2.0 x 2.0 μm , collecting 7 lines in each image. Two images were recorded for each exposure condition, allowing 14 lines to be analyzed. Data analysis was performed on the SEM images using the software package called SuMMIT from EUV Technology. This software allowed the automation of the analysis of many thousands of SEMs collected in this study. SuMMIT measures CD and LER for each line. The edge detection algorithm was held constant for every SEM analyzed. No filtering algorithm was applied to the data.

7.6 RESULTS

7.6.1 Deprotection Kinetics

Open frame exposures over a range of dose were performed on each photoresist formulation as described previously, and the difference between the starting thickness of the resist film and the final thickness of the exposed and baked resist film was measured for each field. The data were normalized such that one represents a film that has not undergone any shrinkage whereas zero represents a film that has undergone maximum shrinkage. It was assumed that film shrinkage is proportional to the conversion of

blocked polymer to unblocked polymer, and hence, Figure 7.6 shows the data plotted as blocking fraction rather than shrinkage.⁷³

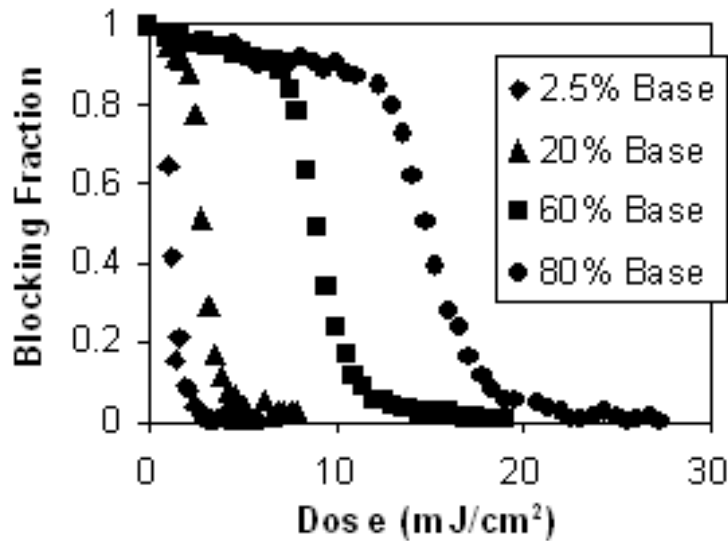


Figure 7.6 Fraction of blocked polymer remaining after PEB

7.6.2 Line-Edge Roughness

Wafers were imaged to generate patterns for LER analysis. SEM images of each field of each wafer were collected and analyzed to measure both CD and LER. Figure 7.7 and Figure 7.8 below show examples of CD and 3σ LER data for the 20% base formulation. CD SEM images showing the dependence of LER on AMag and base loading are shown in Figure 7.9.

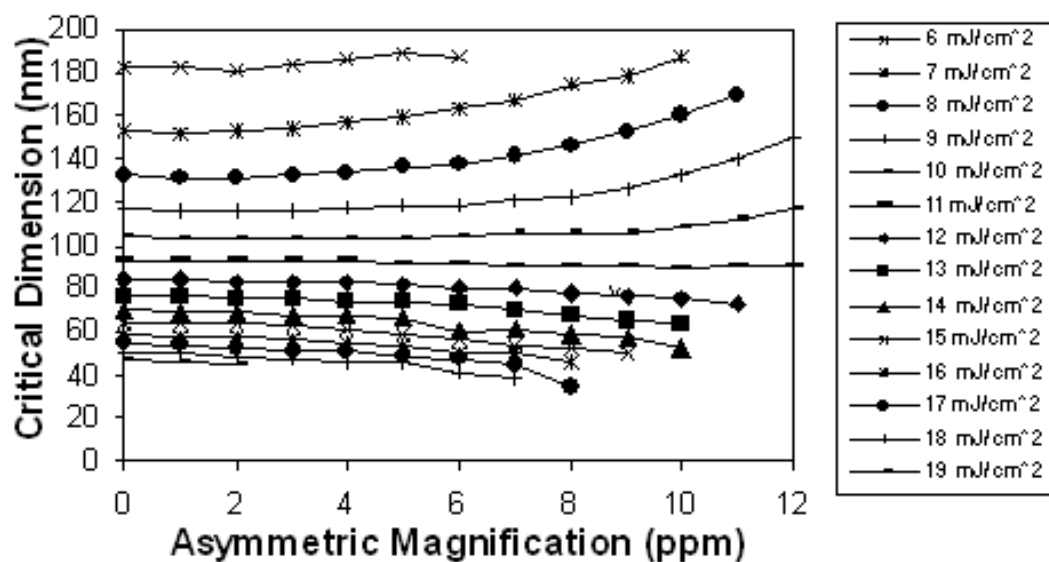


Figure 7.7 CD data through AMag and dose for the 20% base resist

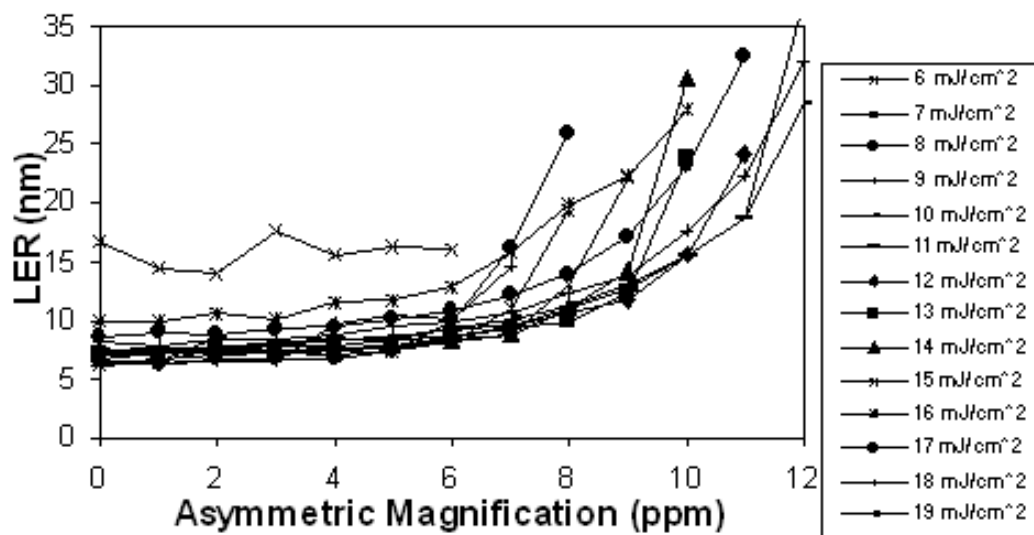


Figure 7.8 3σ LER data through AMag and dose for the 20% base resist

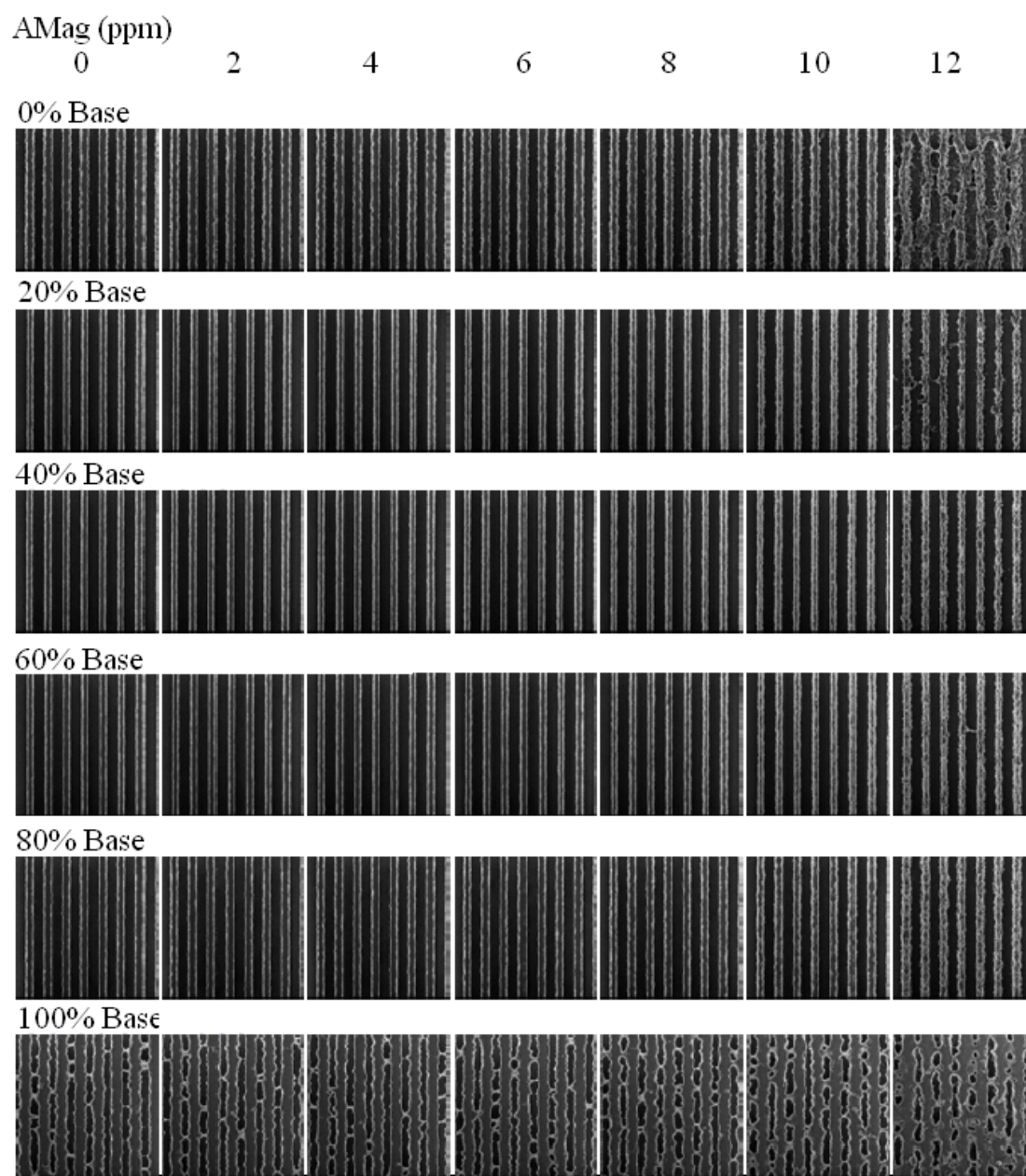


Figure 7.9 CD SEM images of lines in resist showing the effect of asymmetric magnification and base loading on line-edge roughness

7.7 DISCUSSION

7.7.1 Aerial Image Analysis

The aerial image for each imaging condition used in this series of experiments was computed using PROLITH, and AMag error was applied by a convolution of the aerial image with a blur function in the shape of a pulse function. The ILS was calculated directly from the simulated aerial image at the experimentally measured value for the CD. The calculated ILS was plotted against the experimentally determined LER for each imaging condition and formulation used in this study. Figure 7.10 below shows this result. Although the 100% base samples did image, as can be seen in Figure 7.9, no reliable measure of LER could be ascertained due to bridging of the features, and, as a result, that formulation was not included in the following analysis.

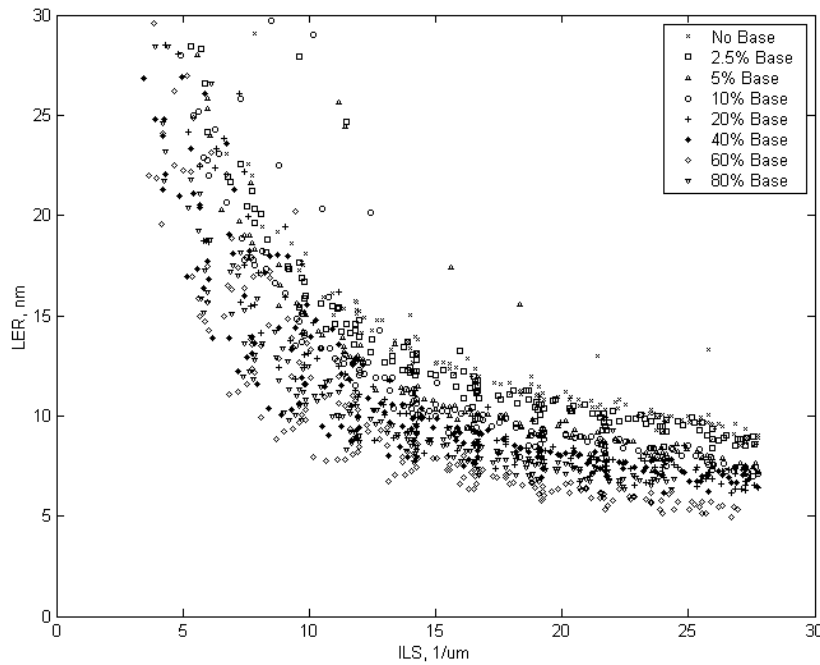


Figure 7.10 The ILS dependence of LER through base loading

Figure 7.10 shows the general trend of decreasing LER as the ILS becomes steeper. Furthermore, it shows a family of curves, one for each base loading, all with the same general shape. Finally it can be seen that the formulation with 60% base exhibited the minimum LER while the low base formulations showed higher LER. Interestingly, the observed LER for the 80% base formulation was higher than for the 60% case. To better visualize this result, LER values at a fixed value of the ILS, $20 \mu\text{m}^{-1}$ were estimated from the data in Figure 7.10. LER for the 100% base loading formulation was estimated as being “high” based on the bridging effect. These data were plotted in Figure 7.11 below.

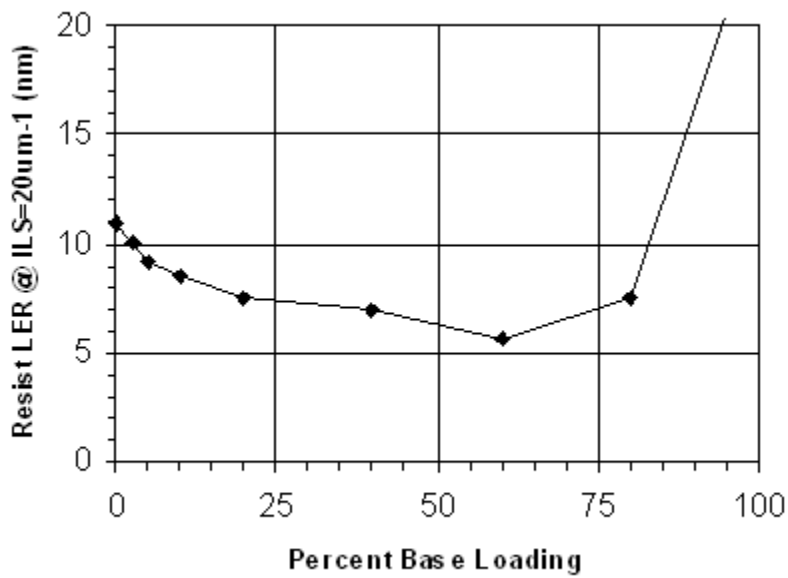


Figure 7.11 Resist 3σ LER through base loading at a fixed ILS of $20 \mu\text{m}^{-1}$

7.7.2 Modeling

The kinetic model described previously was used to fit the contrast data from this round of experiments. Other models exist⁶⁴⁻⁶⁷, as do commercial photoresist simulators such as PROLITH and SOLID-C; however, for the purposes of this analysis, this model was chosen because it contains only three adjustable parameters, it has an analytical solution, and it fits the experimental kinetic data well.⁷⁸ The main drawback to the choice of this model is the fact that diffusion is not taken into account. This model would predict a zero diffusion, or “best case” latent image in the photoresist. This model also assumes no neutralization has occurred at the beginning of the PEB. Adding diffusion would serve to blur and degrade the latent image in the photoresist beyond what is predicted in this model. The purpose of this analysis, however, is not to compute the exact value of the acid concentration throughout the resist, but instead to understand the general behavior and trends in the system, and although diffusion is not included in this model, it should correctly predict the trends. The results of this fit are shown in Figure 7.12 below, which shows normalized blocking fraction as a function of dose. It should be noted that the same rate constants were used for each base concentration. The values for the fit used were $C = 0.11 \text{ cm}^2/\text{mJ}$, $k_{amp} = 0.27 \text{ s}^{-1}$ and $k_{quench} = 4.06 \text{ s}^{-1}$.

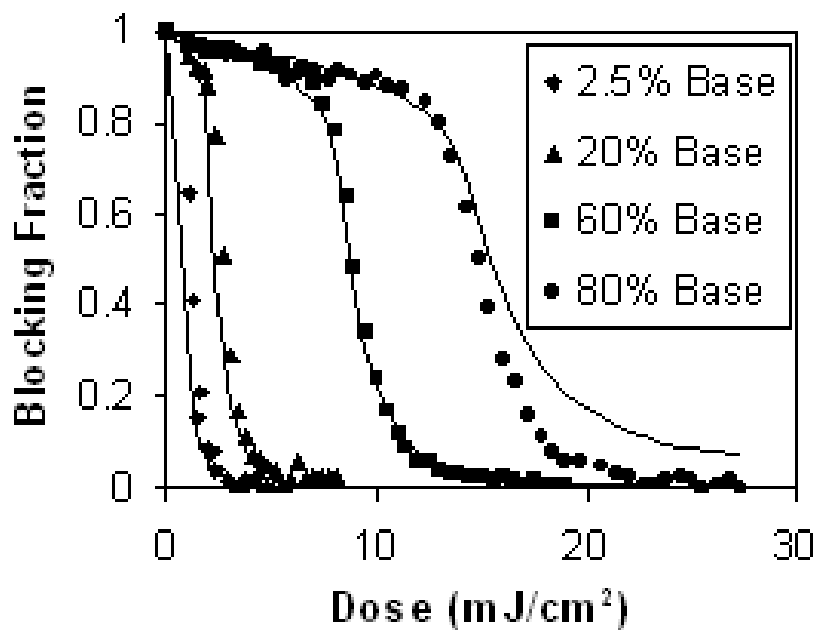


Figure 7.12 Model fit for reaction kinetics. The points represent data while the solid lines represent the model fit.

Using this model fit, the chemical contrast for the system can be computed as described in prior work.^{28,78} Plotting chemical contrast versus base loading as simulated by the model yields Figure 7.13 below.

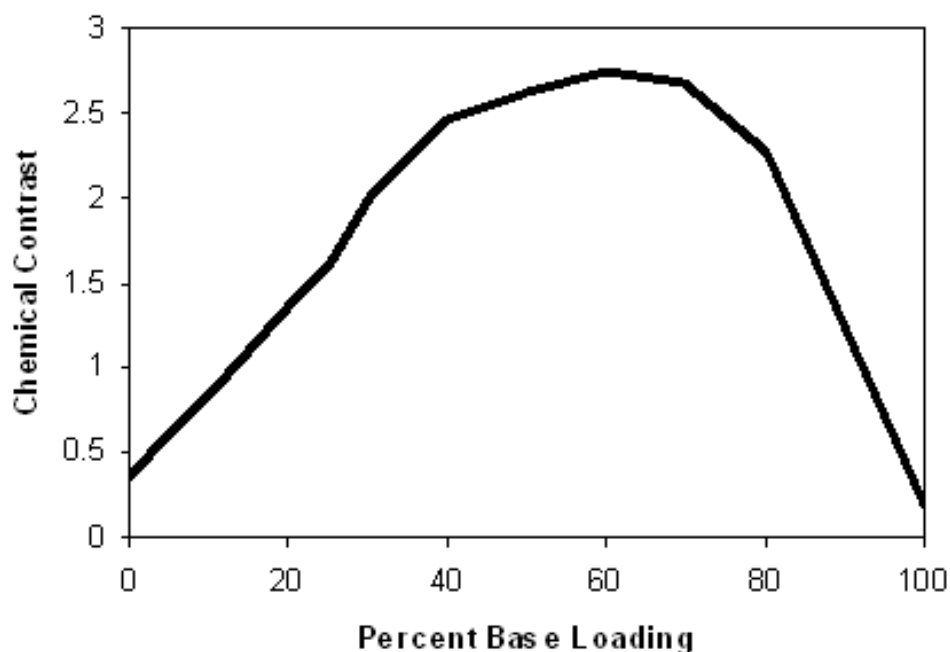


Figure 7.13 Simulated chemical contrast as a function of base loading

The maximum chemical contrast predicted by this analysis occurs at a base loading of 60%, the same base loading at which the minimum value of LER was observed in the experiment. This result is significant because it suggests that the base loading corresponding to the minimum level of LER in a photoresist can be predicted without ever doing an imaging experiment. It also reinforces the tie between chemical gradients in the photoresist film and LER.

The previously calculated aerial images were used as inputs to the kinetic model described above. This procedure yielded normalized blocking fraction of polymer as a function of position for every imaging condition. An example of data generated by this technique is shown in Figure 7.14 below. Once polymer composition as a function of position is known, the polymer composition equivalent of ILS can be calculated. This

value is simply the gradient of protected polymer at the feature edge. This protected polymer gradient will be referred to as the PPG for the remainder of this paper. The PPG should be a superior predictor of LER in photoresist systems because it takes into account the actual chemical gradients in the photoresist prior to develop as opposed to only gradients in the aerial image. As a result, this metric should be applicable to an entire range of possible acid and base loadings in a given photoresist polymer, provided the changes in acid and base loading do not substantially influence the reaction or diffusion kinetics of the system. Figure 7.15 shows LER plotted against PPG for all of the formulations used in this study.

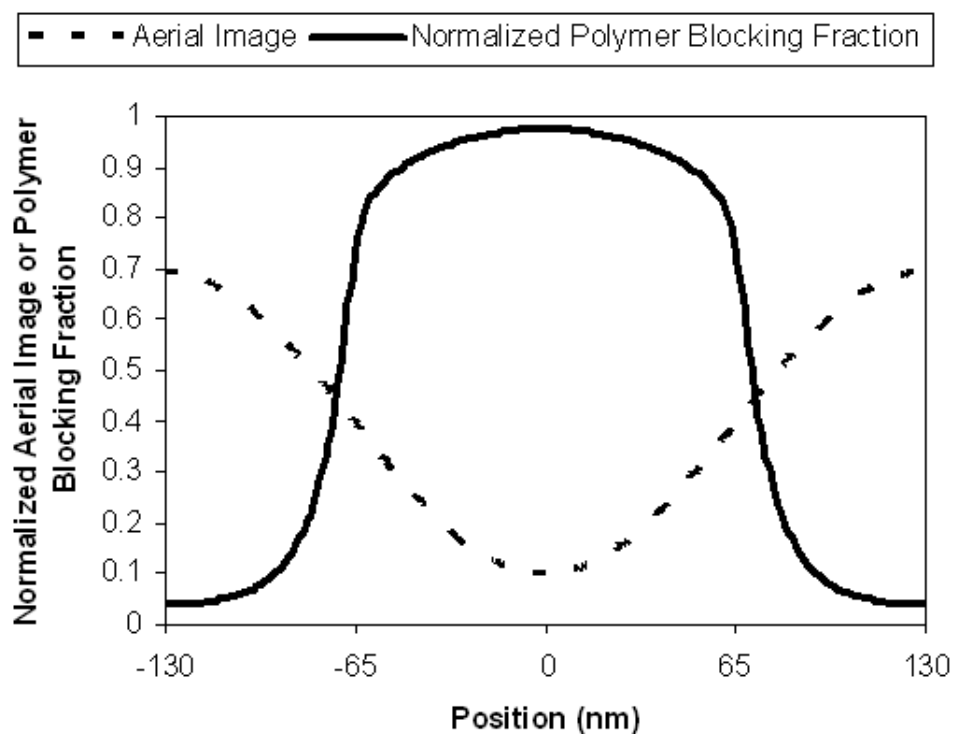


Figure 7.14 Example data for the conversion of an aerial image into a polymer latent image through the use of the kinetic model

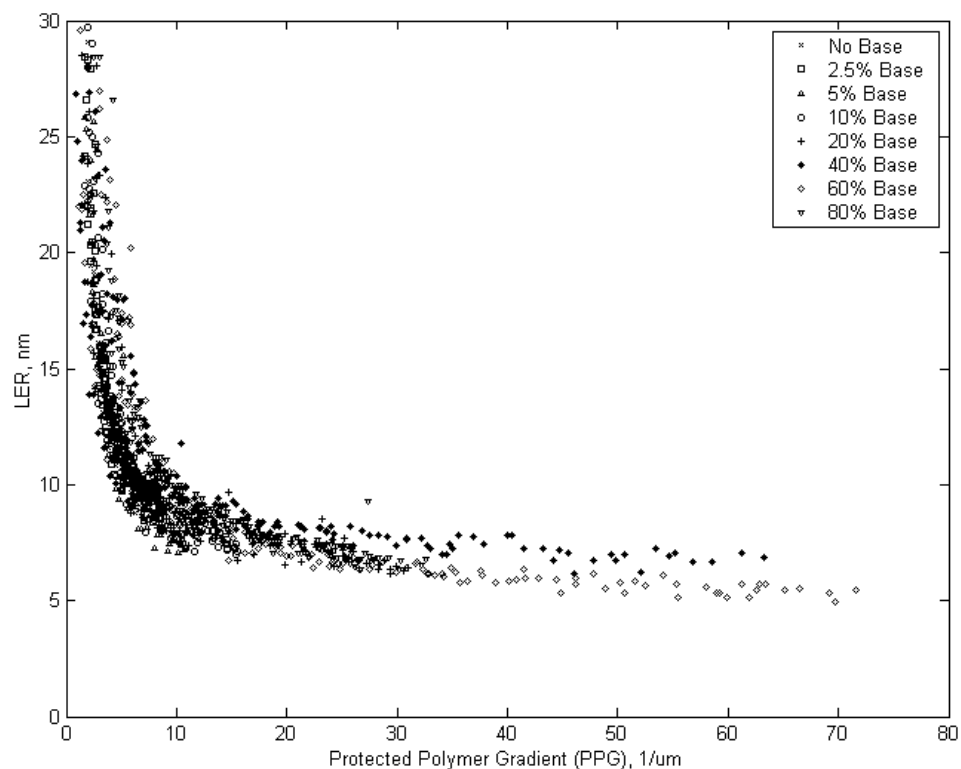


Figure 7.15 LER plotted as a function of PPG

The data shown in Figure 7.15, in contrast those from Figure 7.10, do not segregate into distinctly different curves for each base loading. In effect, the data from each of the eight base loadings from Figure 7.10 have collapsed, within anticipated uncertainty, onto a single master curve governing LER in this photoresist system.

7.8 CONCLUSIONS AND RECOMMENDATIONS

Base concentration was observed to have a huge impact on photoresist performance. The LER of a photoresist without base was observed to increase with post exposure bake temperature, but the addition of base was observed to limit this increase,

possibly by limiting the diffusion of acid molecules into nominally unexposed regions. Large improvements in both LER and photoresist contrast were observed when base concentration was increased in a photoresist. The magnitude of this improvement, however, was observed to diminish as base concentration increased. In other words, going from 0 to 5% base in a resist yields a larger improvement in both LER and contrast than going from 5% to 10% base, even though the same increment in base concentration was used. Photospeed, on the other hand, was observed to steadily increase as base was added to the resist. As a result, it may be advisable to formulate photoresists with smaller base loadings to avoid excessive photospeed penalties. This tradeoff between imaging improvements and photospeed has important implications to resist manufacturers. Photospeed dictates throughput, and although improvements in imaging are desirable, they must be balanced with economic concerns. Resist designers looking to reduce LER to meet targets for the next generation of photoresists may be unable to rely on base alone as a solution the problem. Other techniques or even a change in resist chemistry may be required.

Although ILS has been shown to correlate well with LER for a specific photoresist formulation, it does not explain changes in LER as acid and base loadings are adjusted. In a photoresist, an applied aerial image generates an acid profile, which then reacts with base and the surrounding blocked polymer to generate areas of protected and deprotected polymer. It was theorized that because the protected polymer profile directly determines what the developed photoresist looks like, gradients in protected polymer should be more closely tied to LER than gradients in aerial image intensity or in acid concentration. Hence, the concept of the protected polymer gradient, or PPG, was introduced. LER for this photoresist system was observed to correlate well with PPG as relative base loadings were adjusted from 0% to 80%. Contrary to what many might

expect, when the base loading was equal to the PAG loading, the photoresist did image; however, bridging of the lines prevented accurate LER measurements. The good correlation between LER and PPG indicates that the chemical gradient of blocked polymer within a photoresist is a strong source of LER.

This analysis suggests that if photoresist formulations can be improved to yield higher values for PPG, LER could be significantly reduced. One way to increase the PPG for a specific feature is to adjust the initial blocking fraction of the photoresist polymer such that the edge of the developed feature lies on the steepest part of the polymer latent image. Of course, changing the starting polymer composition may alter the reaction and diffusion kinetics of the system, so performing this task is not necessarily a simple one dimensional optimization problem. Furthermore, the use of photo-decomposable base quenchers in place of some or all of the traditional base quencher could serve to increase the PPG of the system as well.

Chapter 8: Conclusions and Recommendations

This chapter summarizes the conclusions and recommendations for each project presented in previous chapters.

8.1 GRAFT POLYMERIZATION LITHOGRAPHY

A scheme for free radical graft polymerization lithography was developed from the ground up. Syntheses of both the base layer material and the silicon containing monomer were carried out, and a process by which these materials could be used to generate an imaged wafer was described. A grafting chamber was constructed and automated as well. Grafting was demonstrated for both blanket films and patterned features. Unfortunately, although the concept was sound, in its current implementation there are numerous drawbacks to using this technique as opposed to cationic grafting or even conventional lithography.

As the process currently stands, it was observed that high doses are required to fully quench the base layer materials used in this study. Furthermore, the quenching process was observed to be very low contrast. These two factors tend to indicate that high resolution patterning with this technique would be difficult if not impossible. As a result, this technique seems to be more suitable for patterning larger features that have high contrast aerial images such as those much larger than the resolution limit of a stepper or those printed with techniques such as contact printing. Furthermore, even the large features were observed to grow grafts with rounded profiles possibly because of isotropic growth of the grafted polymer. The “rolling hills” shaped grafts are much more difficult to etch than are square shaped profiles generated in conventional lithography. This fact adds further complexity to the process. Also, the monomers used in these

grafting studies were observed to undergo autopolymerization on the surfaces of the windows of the chamber on exposure to UV light. This unintended effect causes a cloudy film to build up on the inside of expensive and hard to clean surfaces in the grafting chamber.

These difficulties all indicate that this process will most likely not become a useful patterning technique. Conventional lithography or even cationic graft polymerization lithography can generate higher resolution images with much greater ease. Because of these many drawbacks, it was decided not to devote further efforts to the study of this process. If future researchers were interested in pursuing this project, the current imaging scheme should most likely be abandoned. Based on the results of these experiments, any process requiring the quenching of an active species to allow grafting in the unexposed areas is not recommended. The reason behind this recommendation is high doses are required to achieve high levels of quenching, and even then incomplete quenching will likely be achieved. Instead, researchers should develop a light-activated species. Furthermore, the photo radical generator used in these studies should probably be replaced with a thermal radical generator. Even though the grafting process may be significantly slower in a thermal process, the use of a thermal radical generator would eliminate the need for exposure during the grafting process as well as the possibility of fouling the chamber windows with undesired polymer. The development of a thermally stable species that on exposure to UV radiation becomes a thermal radical generator is a challenging chemistry project that is beyond the scope of this work. Finally, perhaps the idea of using a living free radical initiator should be revisited to eliminate entirely the oxygen sensitivity issue.

8.2 MODELING BASE QUENCHERS

In order to study the role of acid/base neutralization byproducts in photoresist films, several salts were synthesized and tested for activity. Films of TBOC loaded with different salts were coated onto silicon wafers and then subjected to typical post exposure bake temperatures. These films were monitored with IR spectroscopy for any change. Salts formed from the reaction of strong acids with amine bases were observed to deprotect the resist films without the presence of free acid. The time required for this deprotection in TBOC films, however, is much longer than the time required for free acid to deprotect the film. Salts of weak acids were not observed to cause any change in the film. This result is probably because the weak acids are not strong enough to initiate the photoresist deprotection reaction.

Salts of ionic bases were also not observed to initiate the deprotection of photoresist films. It was concluded that this result was likely caused by the fact that these salts cannot undergo the reverse reaction to regenerate acid without the presence of water. Also, it was observed that salts that had been synthesized or stored in the presence of water produced varying results. These results tend to indicate that water plays an important role in photoresist deprotection kinetics. At this point, no equipment suitable for studying photoresist deprotection kinetics under varying levels of humidity is available in the Willson group labs, but it is recommended that such equipment be acquired or constructed if further studies of photoresist deprotection kinetics are to be undertaken.

Photoresist films containing active salts were observed to initiate the deprotection of TBOC films, but this deprotection was extremely slow compared to deprotection initiated by free acid. Furthermore, the presence of salt did not seem to greatly influence the rate at which TBOC is deprotected by free acid. Because of these factors, it was

concluded that although salts can be active in photoresist films, the time scale at which salts react with the photoresist is much slower than the time scale at which free acid is active. Because of this salts do not likely contribute significantly to the lithographic process.

Base type was not observed to have a strong influence on imaging performance of 248nm resists in these studies although PROLITH simulations predict differently. Three general types of bases were used in these studies, trialkyl amines, hydroxyl containing (hydrogen bonding) amines, and TBAH (ionic rather than amine). Varying the size of the base was expected to cause variations in the diffusion coefficient of the base, which would in turn lead to shifts in the isofocal CD. Such shifts were not observed, although it is possible that such shifts were occurring but their magnitude was below the experimental error associated with this study. One reason for the discrepancy between experiment and simulation could be that base diffuses much more slowly in the photoresist film than acid. Another reason could be the influence of other parameters not accounted for in the simulation. Similar experiments in which acid type rather than base type was varied were performed as well. In this case, a large shift in isofocal CD was observed with changing acid size. These shifts correlated well to shifts predicted by simulation.

A 193nm resist was also investigated. Contrary to the results observed with the 248nm resist, base loading was observed to influence bias. In this case, however, bias was observed to initially decrease and then increase again as base loading was increased. It is thought that this result might be caused because a fast diffusing base could be overwhelmed by a much larger amount of slower diffusing acid, but as base loading is increased, base diffusion would become more dominant. The fact that bias shifts at all

tends to indicate that base diffusion in the 193nm system may be much greater than in the 248nm system.

Clearly additional studies are needed to fully understand bias in these systems. Future work should begin by independently measuring the diffusion coefficient of bases through photoresist films. One proposal by which this goal might be accomplished is to use a trilayer film stack similar to those used by researchers at UT to measure acid diffusion coefficients.⁷⁹ In this experiment, one would coat a polymer loaded with a high concentration of the diffusing species. Either the base itself could be used or for more control over the time at which diffusion begins, a photo-base generator could be used.^{80,81} The second layer of the film stack would be the photoresist polymer that diffusion is to be measured in. The final layer of the film stack should be a base sensitive detector layer that gives a measurable signal when heated in the presence of base. Such a polymer has recently been developed by researchers at UT. Imaging studies should also be continued. One study in particular that would be interesting is to see how the differing bases such as THA, TOA, and TDDA affect bias in the 193nm system. Also, variables such as developer threshold, polymer type, and acid loading, which have not been previously considered, should be investigated as well.

Base concentration was observed to have a huge impact on photoresist performance. The LER of a photoresist without base was observed to increase with post exposure bake temperature, but the addition of base was observed to limit this increase, possibly by limiting the diffusion of acid molecules into nominally unexposed regions. Large improvements in both LER and photoresist contrast were observed when base concentration was increased in a photoresist. The magnitude of this improvement, however, was observed to diminish as base concentration increased. In other words, going from 0 to 5% base in a resist yields a larger improvement in both LER and contrast

than going from 5% to 10% base, even though the same increment in base concentration was used. Photospeed, on the other hand, was observed to steadily increase as base was added to the resist. As a result, it may be advisable to formulate photoresists with smaller base loadings to avoid excessive photospeed penalties. This tradeoff between imaging improvements and photospeed has important implications to resist manufacturers. Photospeed dictates throughput, and although improvements in imaging are desirable, they must be balanced with economic concerns. Resist designers looking to reduce LER to meet targets for the next generation of photoresists may be unable to rely on base alone as a solution the problem. Other techniques or even a change in resist chemistry may be required.

Although ILS has been shown to correlate well with LER for a specific photoresist formulation, it does not explain changes in LER as acid and base loadings are adjusted. In a photoresist, an applied aerial image generates an acid profile, which then reacts with base and the surrounding blocked polymer to generate areas of protected and deprotected polymer. It was theorized that because the protected polymer profile directly determines what the developed photoresist looks like, gradients in protected polymer should be more closely tied to LER than gradients in aerial image intensity or in acid concentration. Hence, the concept of the protected polymer gradient, or PPG, was introduced. LER for this photoresist system was observed to correlate well with PPG as relative base loadings were adjusted from 0% to 80%. Contrary to what many might expect, when the base loading was equal to the PAG loading, the photoresist did image; however, bridging of the lines prevented accurate LER measurements. The good correlation between LER and PPG indicates that the chemical gradient of blocked polymer within a photoresist is a strong source of LER.

This analysis suggests that if photoresist formulations can be improved to yield higher values for PPG, LER could be significantly reduced. One way to increase the PPG for a specific feature is to adjust the initial blocking fraction of the photoresist polymer such that the edge of the developed feature lies on the steepest part of the polymer latent image. Of course, changing the starting polymer composition may alter the reaction and diffusion kinetics of the system, so performing this task is not necessarily a simple one dimensional optimization problem. Furthermore, the use of photo-decomposable base quenchers in place of some or all of the traditional base quencher could serve to increase the PPG of the system as well.

References

- (1) Thompson, L. F.; Willson, C. G.; Bowden, M. J., Eds. *Introduction to Microlithography*, 2nd ed.; American Chemical Society: Washington D.C., 1994.
- (2) Campbell, S. A. *The Science and Engineering of Microelectronic Fabrication*, 2nd ed.; Oxford University Press: New York, 2001.
- (3) Moore, G. E. *Proceedings of the IEEE* **1976**, 64, 837.
- (4) Intel Corporation Website. <http://www.intel.com/technology/silicon/mooreslaw/>. July 17, 2005.
- (5) IBM Website. <http://www.ibm.com/chips/technology/makechip/breakthroughs/copper.html>. July 17, 2005.
- (6) Mack, C. A. *Inside PROLITH*; FINLE Technologies, Inc.: Austin, TX, 1997.
- (7) Willson, C. G.; Dammel, R. A.; Reiser, A. *Proceedings of SPIE-The International Society for Optical Engineering* **1997**, 3049, 28-41.
- (8) Rathsack, B. M.; Tabery, C. E.; Stachowiak, T. B.; Dallas, T.; Xu, C. B.; Willson, C. G. *Proceedings of SPIE-The International Society for Optical Engineering* **1999**, 3873, 80-91.
- (9) Dammel, R. A. *Diazonaphthoquinone-based Resists*; SPIE Optical Engineering Press: Bellingham, WA, 1993.
- (10) Breyta, G.; Hofer, R.; Ito, H.; Seeger, J.; Petrillo, D.; Moritz, T.; Fischer, J. *Photopolymer Science and Technology* **1994**, 7, 449.
- (11) Ito, H.; Breyta, G.; Hofer, R.; Sooriyakunaran, K.; Petrillo, D.; Seeger, J. *Photopolymer Science and Technology* **1993**, 7, 433.
- (12) Thompson, L. F.; Willson, C. G.; Tagawa, S., Eds. *Polymers for Microelectronics: Resists and Dielectrics*; American Chemical Society: Washington D.C., 1994.
- (13) Michaelson, T. B.; Pawloski, A.; Acheta, A.; Nishimura, Y.; Willson, C. G. *Proceedings of SPIE-The International Society for Optical Engineering* **2005**, 5753, 368-379.

- (14) Intel Corporation Website. <http://www.intel.com/technology/silicon/si11032.htm>. July 17, 2005.
- (15) Taylor, J. C.; Shayib, R.; Goh, S.; Chambers, C. R.; Conley, W.; Lin, S.-H.; Willson, C. G. *Proceedings of SPIE-The International Society for Optical Engineering* **2005**, 5753, 836-846.
- (16) Taylor, J. C.; Chambers, C. R.; Deschner, R.; LeSuer, R. J.; Conley, W. E.; Burns, S. D.; Willson, C. G. *Proceedings of SPIE-The International Society for Optical Engineering* **2004**, 5376, 34-43.
- (17) LeSuer, R. J.; Fan, F. F.; Bard, A. J.; Taylor, C.; Tsiartas, P.; Willson, C. G.; Conley, W.; Feit, G.; Kunz, R. *Proceedings of SPIE-The International Society for Optical Engineering* **2004**, 5376, 115-125.
- (18) Conley, W.; LeSuer, R. J.; Fan, F. F.; Bard, A. J.; Taylor, C.; Tsiartas, P.; Willson, C. G.; Romano, A.; Dammel, R. A. *Proceedings of SPIE-The International Society for Optical Engineering* **2005**, 5753, 64-77.
- (19) Brodsky, C.; Byers, J.; Conley, W.; Hung, R.; Yamada, S.; Patterson, K.; Somervell, M.; Trinquet, B.; Tran, H. V.; Cho, S.; Chiba, T.; Lin, S.-H.; Jamieson, A.; Johnson, H.; Vander Heyden, T.; Willson, C. G. *Journal of Vacuum Science & Technology, B: Microelectronics and Nanometer Structures* **2000**, 18, 3396-3401.
- (20) Hung, R.; Tran, H. V.; Trinquet, B.; Chiba, T.; Yamada, S.; Sanders, D.; Connor, E.; Grubbs, R.; Klopp, J.; Frechet, M. J.; Thomas, B.; Shafer, G.; DesMarteau; Conley, W.; Willson, C. G. *Proceedings of SPIE-The International Society for Optical Engineering* **2001**, 4345, 385-395.
- (21) Colburn, M.; Johnson, S.; Stewart, M.; Damle, S.; Bailey, T. C.; Choi, B.; Wedlake, M.; Michaelson, T.; Sreenivasan, S. V.; Ekerdt, J.; Willson, C. G. *Proceedings of SPIE-The International Society for Optical Engineering* **1999**, 3676, 379-389.
- (22) Lin, B. J. *Introduction to Microlithography*, 1st ed.; Thompson, L. F.; Willson, C. G.; Bowden, M. J., Eds.; American Chemical Society: Washington D. C., 1983; pp 288-348.
- (23) Sezi, R.; Leuschner, R.; Sebald, M.; Ahne, H.; Birkle, S.; Borndorfer, H. *Proceedings of SPIE-The International Society for Optical Engineering* **1990**, 1262, 84.

- (24) Sebald, M.; Berthold, J.; Beyer, M.; Leuschner, R.; Nolscher, C.; Scheler, U.; Sezi, R.; Ahne, H.; Birkle, S. *Proceedings of SPIE-The International Society for Optical Engineering* **1991**, 1466, 227.
- (25) Somervell, M. *Top Surface Imaging Through Vapor Phase Silylation for 193nm Lithography*. Doctoral Thesis for The Department of Chemical Engineering, The University of Texas at Austin. 2000
- (26) MacDonald, S. A.; Schlosser, H.; Ito, H.; Clecak, J.; Willson, C. G. *Chemistry of Materials* **1991**, 3, 435.
- (27) Ito, H.; MacDonald, S. A.; Miller, R. D.; Willson, C. G.: United States Patent Number 4,552,833.
- (28) Jamieson, A. T. *Top Surface Imaging for Sub 100-nm Lithography*. Doctoral Thesis for The Department of Chemical Engineering, The University of Texas at Austin. 2004
- (29) Brodsky, C. *Graft Polymerization Lithography*. Doctoral Thesis for The Department of Chemical Engineering, The University of Texas at Austin. 2001
- (30) Hult, A.; MacDonald, S. A.; Willson, C. G. *Macromolecules* **1985**, 18, 1804.
- (31) Kim, S. Y.; Choi, J.; Pulver, D.; Moore, J. A.; Corelli, J. C.; Steckl, A. J. *Journal of Vacuum Science & Technology, B: Microelectronics and Nanometer Structures* **1986**, 4, 403-408.
- (32) Liu, W. T.; Corelli, J. C.; Steckl, A. J.; Moore, J. A. *Applied Physics Letters*. **1984**, 44, 973.
- (33) de Boer, B.; Simon, H. K.; Werts, M. P. L.; van der Vegte, E. W.; Hadziioannou, G. *Macromolecules* **2000**, 33, 349-356.
- (34) Ejaz, M.; Yamamoto, S.; Ohno, K.; Tsujii, Y.; Fukuda, T. *Macromolecules* **1998**, 31, 5934-5936.
- (35) Ejaz, M.; Yamamoto, S.; Tsujii, Y.; Fukuda, T. *Macromolecules* **2002**, 35, 1412-1418.
- (36) Hyun, J.; Chilkoti, A. *Macromolecules* **2001**, 34, 5644-5652.
- (37) Kaholek, M.; Lee, W.-K.; Ahn, S.-J.; Ma, H.; Caster, K. C.; LaMattina, B.; Zauscher, S. *Chemistry of Materials* **2004**, 16, 3688-3696.
- (38) Pieracci, J.; Crivello, J. V.; Belfort, G. *Chemistry of Materials* **2002**, 14, 256-265.

- (39) Ziani-Cherif, H.; Kou, I.; Matsuda, T. *Macromolecules* **1999**, *32*, 3438-3447.
- (40) Allmer, K.; Hult, A.; Ranby, B. *Journal of Polymer Science: Part A: Polymer Chemistry* **1988**, *26*.
- (41) Allmer, K.; Hult, A.; Ranby, B. *Journal of Polymer Science: Part A: Polymer Chemistry* **1989**, *27*, 1641-1652.
- (42) Willson, C. G.; McAdams, C. L.; Yueh, W.; Osborn, B. P. *Polymer Preprints* **2000**, *41*, 946.
- (43) Benoit, D.; Chaplinski, V.; Braslau, R.; Hawker, C. J. *Journal of the American Chemical Society* **1999**, *121*, 3904-3920.
- (44) Dao, J.; Benoit, D.; Hawker, C. J. *Journal of Polymer Science: Part A: Polymer Chemistry* **1998**, *36*, 2161-2167.
- (45) Grubbs, R. B.; Hawker, C. J.; Dao, J.; Frechet, J. *Angewandte Chemie International* **1997**, *36*, 270-272.
- (46) Hawker, C. J. *Journal of the American Chemical Society* **1994**, *116*, 11185-11186.
- (47) Hawker, C. J.; Barclay, G. G.; Orellana, A.; Dao, J.; Devonport, W. *Macromolecules* **1996**, *29*, 5245-5254.
- (48) Husseman, M.; Malmstrom, E. E.; McNamara, M.; Mate, M.; Mecerreyes, D.; Benoit, D. G.; Hedrick, J. L.; Mansky, P.; Huang, E.; Russell, T. P.; Hawker, C. J. *Macromolecules* **1999**, *32*, 1424-1431.
- (49) Wang, J.-S.; Matyjaszewski, K. *Journal of the American Chemical Society* **1995**, *117*, 5614-5615.
- (50) Gaynor, S. G.; Matyjaszewski, K. *ACS Polymer Preprints* **1997**, *38*, 758-759.
- (51) Matyjaszewski, K. *Macromolecules* **1998**, *31*, 4710-4717.
- (52) Kato, M.; Kamigaito, M.; Sawamoto, M.; Higashimura, T. *Macromolecules* **1995**, *28*, 1721.
- (53) Webster, O.; Hertler, W. R.; Sogah, D. Y.; Farnham, W. B.; RajanBabu, T. V. *Journal of the American Chemical Society* **1983**, *105*, 5706-5707.
- (54) Webster, O. *Journal of Polymer Science: Part A: Polymer Chemistry* **2000**, *38*, 2855-2860.

- (55) de Brouwer, H.; Schellekens, M. A. J.; Klumperman, B.; Monteiro, M. J.; German, A. L. *Journal of Polymer Science: Part A: Polymer Chemistry* **2000**, *38*, 3596-3603.
- (56) Percec, V.; Barboiu, B. *Macromolecules* **1995**, *28*, 7970-7972.
- (57) McAdams, C. L. *Polymers and Photoactive Compounds for Non-Chemically Amplified Deep-UV Photoresists*. Doctoral Thesis for The Department of Chemistry, The University of Texas at Austin. 2000
- (58) Ono, N.; Yamada, T.; Saito, T.; Tanaka, K.; Kaji, A. *Bulletin of the Chemical Society of Japan* **1978**, *51*, 2401-2404.
- (59) Ohta, S.; Yamashita, M.; Arita, K.; Kajiura, T.; Kawasaki, I.; Noda, K.; Izumi, M. *Chemical Pharmaceutical Bulletin* **1995**, *43*, 1294-1301.
- (60) Colburn, M.; Grot, A.; Amistoso, M.; Choi, B. J.; Bailey, T.; Ekerdt, J.; Sreenivasan, S. V.; Hollenhorst, J.; Willson, C. G. *Proceedings of SPIE-The International Society for Optical Engineering* **2000**, *3999*, 453-457.
- (61) Yano, E.; Kuramitsu, Y.; Watanabe, K.; Namiki, T.; Nozaki, K.; Igarashi, M. *Proceedings of SPIE-The International Society for Optical Engineering* **1995**, *2438*, 551-562.
- (62) Ferreira, L.; Malik, S.; Sarubbi, T. R.; Blakeney, A. J.; Maxwell, B. *Proceedings of SPIE-The International Society for Optical Engineering* **1998**, *3333*, 236-244.
- (63) *International Technology Roadmap for Semiconductors (ITRS)*; Semiconductor Industry Association, 2003.
- (64) Hinsberg, W. D.; Houle, F. A.; Sanchez, M. I.; Morrison, M. E.; Wallraff, G. M.; Larson, C. E.; Hoffnagle, J. A.; Brock, P. J.; Breyta, G. *Proceedings of SPIE-The International Society for Optical Engineering* **2000**, *3999*, 148-160.
- (65) Houle, F. A.; Hinsberg, W. D.; Sanchez, M. I.; Hoffnagle, J. A. *Journal of Vacuum Science & Technology, B: Microelectronics and Nanometer Structures* **2002**, *20*, 924-931.
- (66) Fukuda, H.; Hattori, K. T.; Hagiwara, T. *Proceedings of SPIE-The International Society for Optical Engineering* **2001**, *4346*, 319-330.
- (67) Hattori, K. T.; Abe, J.; Fukuda, H. *Proceedings of SPIE-The International Society for Optical Engineering* **2002**, *4691*, 1243-1253.

- (68) Pawloski, A. R.; Christian; Nealey, P. F. *Chemistry of Materials* **2002**, *14*, 4192-4201.
- (69) Van Steenwinckel, D.; Lammers, J. *Proceedings of SPIE-The International Society for Optical Engineering* **2003**, 5039, 225-239.
- (70) Sauer, C. A.; Mack, C. A. *Proceedings of SPIE-The International Society for Optical Engineering* **1999**, 3748, 27-40.
- (71) Petersen, J. S.; Byers, J. D.; Carpio, R. A. *Microelectronic Engineering* **1997**, *35*, 169-174.
- (72) Arthur, G.; Martin, B. *Proceedings of SPIE-The International Society for Optical Engineering* **1996**, 2725, 85-93.
- (73) Burns, S. D.; Medeiros, D. R.; Johnson, H. F.; Wallraff, G. M.; Hinsberg, W. D.; Willson, C. G. *Proceedings of SPIE-The International Society for Optical Engineering* **2002**, 4690, 321-331.
- (74) Atkins, P. *Physical Chemistry*, 5th ed.; W. H. Freeman and Company: New York, 1994.
- (75) Pawloski, A. R.; Acheta, A.; Lalovic, I.; La Fontaine, B.; Levinson, H. *Proceedings of SPIE-The International Society for Optical Engineering* **2004**, 5376, 414-425.
- (76) Smith, M. D.; Byers, J. D.; Mack, C. A. *Proceedings of SPIE-The International Society for Optical Engineering*, 5376, 322-332.
- (77) Pawloski, A. R.; Acheta, A.; Levinson, H. J.; Michaelson, T.; Willson, C. G. *Proceedings ARCH Interface* **2004**.
- (78) Michaelson, T. B.; Jamieson, A. T.; Pawloski, A. R.; Byers, J.; Acheta, A.; Willson, C. G. *Proceedings of SPIE-The International Society for Optical Engineering* **2004**.
- (79) Stewart, M. D. *Catalyst Diffusion in Positive-Tone Chemically Amplified Photoresists*. Doctoral Thesis for The Department of Chemical Engineering, The University of Texas at Austin. 2003
- (80) Cameron, J. F.; Willson, C. G.; Frechet, J. M. J. *Polymeric Materials Science and Engineering, Proceedings of the ACS* **1996**, *74*, 284-285.

- (81) Tatersall, P. I.; Breslin, D.; Grayson, S. M.; Heath, W. H.; Lou, K.; McAdams, C. L.; McKean, D.; Rathsack, B. M.; Willson, C. G. *Chemistry of Materials* **2004**, *16*, 1770-1774.
- (82) Rice, B. J.; Cao, H. B.; Chandhok, M.; Meagley, R. P. *Proceedings of SPIE-The International Society for Optical Engineering* **2003**, *5039*, 384-392.
- (83) Shibata, K.; Izumi, N.; Tsujita, K. *Proceedings of SPIE-The International Society for Optical Engineering* **2004**, *5375*, 865-873.
- (84) Asenov, A.; Brown, A. R.; Davies, J. H.; Kaya, S.; Slavcheva, G. *IEEE Transactions on Electron Devices* **2003**, *50*, 1837-1852.
- (85) Asenov, A.; Kaya, S.; Brown, A. R. *IEEE Transactions on Electron Devices* **2003**, *50*, 1245-1260.
- (86) Diaz, C. H.; Tao, H. J.; Ku, Y. C.; Yen, A.; Young, K. *IEEE Electron Device Letters* **2001**, *22*, 287-289.
- (87) International Technology Roadmap for Semiconductors (ITRS), Semiconductor Industry Association, 2003.
- (88) Stewart, M. D.; Schmid, G. M.; Goldfarb, D. L.; Angelopoulos, M.; Willson, C. G. *Proceedings of SPIE-The International Society for Optical Engineering* **2003**, *5039*, 415-422.
- (89) Watanabe, M.; Yabe, S.; Machida, S.; Taguchi, T. *Journal of Photopolymer Science and Technology* **1999**, *12*, 643-648.
- (90) Peters, R. D.; Lucas, K.; Cobb, J. L.; Parker, C.; Patterson, K.; McCauley, R.; Ercken, M.; Van Roey, F.; Vandenbroeck, N.; Pollentier, I. K. *Proceedings of SPIE-The International Society for Optical Engineering* **2003**, *5038*, 1131-1142.
- (91) Koh, H. P.; Lin, Q.; Hu, X.; Chan, L. H. *Proceedings of SPIE-The International Society for Optical Engineering* **2000**, *3999*, 240-251.
- (92) Williamson, M.; Neureuther, A. *Proceedings of SPIE-The International Society for Optical Engineering* **2003**, *4690*, 357-365.
- (93) Williamson, M.; Meng, X.; Neureuther, A. *Proceedings of SPIE-The International Society for Optical Engineering* **2002**, *4690*, 357-365.
- (94) Yoshizawa, M.; Moriya, S. *Journal of Vacuum Science & Technology B* **2000**, *18*, 3105-3110.

- (95) Hinsberg, W. D.; Houle, F. A.; Hoffnagle, J. A.; Sanchez, M. I.; Wallraff, G. M.; Frank, S. *Journal of Vacuum Science & Technology B* **1998**, *16*, 3689-3694.
- (96) Sanchez, M. I.; Hinsberg, W. D.; Houle, F. A.; Hoffnagle, J. A.; Ito, H.; Nguyen, C. *Proceedings of SPIE-The International Society for Optical Engineering* **1999**, 3678, 160-171.
- (97) Ma, Y.; Tsvd, G.; Cerrina, F. *Journal of Vacuum Science & Technology B* **2003**, *21*, 3124-3130.
- (98) Shin, J.; Han, G.; Ma, Y.; Moloni, K.; Cerrina, F. *Journal of Vacuum Science & Technology B* **2001**, *19*, 2890-2895.
- (99) Lalovic, I.; Kroyan, A.; Kye, J.; Liu, H. Y.; Levinson, H. J. *Proceedings of SPIE-The International Society for Optical Engineering* **2003**, 5040, 1570-1580.

Vita

Timothy Bryan Michaelson was born on January 17, 1979 in Las Vegas, New Mexico to parents David and Margie Michaelson. He graduated from Clear Lake High School in Houston, Texas in 1996. In 2000, He graduated from The University of Texas at Austin with a B.S. degree in chemical engineering with highest honors. He received an M.S. degree in chemical engineering from the University of Texas at Austin in 2003 and will receive his Ph.D. in 2005. He has had an internship at Micron Technology in Boise, Idaho and will begin employment at Applied Materials in Santa Clara, California upon graduation.

Permanent address: 4640 Westview Terrace, Santa Fe, New Mexico 87507

This dissertation was typed by the author.